UNIVERSITY OF OKLAHOMA

GRADUATE COLLEGE

ANALYTICAL AND COMPUTATIONAL MODELING OF MULTIPHASE FLOW IN FERROFLUID CHARGED OSCILLATING HEAT PIPES

A DISSERTATION

SUBMITTED TO THE GRADUATE FACULTY

In partial fulfillment of the requirements for the

Degree of

Doctor of Philosophy

Mechanical Engineering

By

Huiyu Wang
Norman, OK
2020

ANALYTICAL AND COMPUTATIONAL MODELING OF MULTIPHASE FLOW IN FERROFLUID CHARGED OSCILLATING HEAT PIPES

A DISSERTATION APPROVED FOR THE SCHOOL OF AEROSPACE AND MECHANICAL ENGINEERING

BY THE COMMITTEE CONSISTING OF

Dr. D. Keith Walters, Chair

Dr. Keisha B. Walters, Chair

Dr. Hamidreza Shabgard

Dr. Prakash Vedula

Dr. Jivtesh Garg

Dr. Jessica E. Ruyle

ABSTRACT

Electromagnetic-based energy harvesting materials and devices have emerged as a prominent research area in the last ten years, especially systems using ferrofluidic induction—a process that generates voltage via the pulsation of a ferrofluid (iron-based nanofluid) through a solenoid. This work includes the development of an analytical model and computational modeling methods to investigate ferrofluid pulsating flow within an energy harvesting device and the mass and heat transfer performance of a two-phase closed thermosyphon (TPCT) and oscillating heat pipe (OHP). First, an analytical model is proposed to predict the induced electromotive force (EMF) based on the flow behavior and magnetic properties of a pulsating ferrofluid energy harvesting device. The model identifies key parameters for describing and optimizing induction for ferrofluid pulsing through a solenoid. Data from a previously documented experimental study was used to validate the analytical model, and both the experimental data and analytical model show the same trends with the induced EMF increasing as a function of pulsating frequency and magnetic field strength as a higher percentage of the ferrofluid nanoparticle moments are aligned. Second, computational fluid dynamics (CFD) simulations were performed to predict the heat transfer performance of a TPCT. Simulations were performed using a three-dimensional finite-volume flow solver (ANSYS Fluent) with a pressure-based scheme for the solution of the continuity and momentum equations, volume-of-fluid method for resolution of the liquid-vapor phase interface, and a temperature-dependent model for interphase mass transfer by evaporation and condensation. Different model and numerical scheme combinations were investigated to identify an efficient and consistently accurate method using currently available software tools. To address issues with previously published simulation methods violating the conservation of mass, a new variable saturation temperature model was tested along with mass transfer coefficients based

on the vapor-liquid density ratio and more physically realistic boundary conditions. The variable saturation temperature model significantly mitigated mass and energy imbalance in the simulations, for both constant heat flux and convection condenser boundary conditions. In addition, for the VOF discretization the Geo-Reconstruct scheme was found to be more accurate than the Compressive scheme available in Fluent without additional computational cost. Third, simulations of a vertical OHP were performed using the CFD methodology developed for the TPCT system. Results show simulations using appropriate values for the evaporation and condensation mass transfer time relaxation parameters and the new variable saturation temperature model are in good agreement with the available experimental data. For the OHP system, using the Compressive discretization scheme for the VOF model allowed for computationally efficient simulation. It is believed that the advances in analytical and computational modeling developed in this research project will contribute important steps toward development of an accurate, efficient, and comprehensive simulation methodology to predict multiphase flow, heat transfer, and energy harvesting in ferrofluid charged oscillating heat pipes.

ACKNOWLEDGEMENTS

I would like to thank my advisors Dr. D. Keith Walters and Dr. Keisha B. Walters for all their tremendous support, advice, and patience and for bringing me with them to University of Oklahoma. They are always willing to talk through any question or concern and remained positive and encouraging no matter how many times my simulations failed. All the research ideas, simulation results, and resulting publications and presentations were spurred on by their guidance. Thank you both for helping me to become a better researcher, writer, and leader.

My most sincere gratitude is expressed to my dissertation committee members for their input and counseling throughout my Ph.D. program. I am grateful to Dr. Hamidreza Shabgard for his insight and understanding of the heat pipe work. To my other committee members, this work would not have come together without their instruction, help, patience, and kindness throughout my graduate study. I am also grateful to Dr. Matt Berg who I met at Mississippi State University for his expertise and advice on the electromagnetic induction analytical model.

I want to thank my parents for raising me and instilling in me a strong work ethic and all the love, support, and understanding while I was studying abroad. I would not be the person I am without their love and sacrifices.

Graduate school would have been a monotonous affair had it not been for the friendship and camaraderie of my teammates. We provided each other counsel, humor, and assistance; many tasks were lightened by many hands. I would like to thank my teammates, Tausif Jamal and Olalekan O. Shobayo, for their help and assistances. I am also thankful to all my friends, Qi Qiao, Wen Yang, Jing Wen, Monica Chidurala, Brandon Abbott, Mackenzie Carney, and Songyuan Yao for all the joyful moments we had together in Norman or Starkville.

TABLE OF CONTENTS

LIST OF FIGURES

LIST OF TABLES

NOMENCLATURE

Greek symbols

α	Volume fraction
α_L	Langevin parameter
ω	Angular frequency (Hz)
μ	Dynamic viscosity (kg/m·s)
μ_F	Permeability of the ferrofluid (N/A^2)
μ_0	Permeability of the free space (N/A^2)
ρ	Density (kg/m^3)
σ	Surface tension coefficient (N/m)
σ_s	Saturation mass magnetization (emu/g, Am^2/kg)
χ	Susceptibility
χ_i	Initial susceptibility
λ	Dipolar coupling coefficient
ϕ	Volume fraction of the nanoparticles
Φ	Magnetic flux (Wb)
κ	Surface curvature

θ	Contact angle

Symbols

A	Surface area (m^2)
B	Magnetic flux density (mT)
c_p	Specific heat (J/kgK)
d	Diameter (m)
D	Displacement (m)
E	Energy (J)
E_I	Induced electromotive force (EMF) (μV)
f	Frequency (Hz)
F	Force
G	Gravity
k	Thermal conductivity (W/mK)
k_B	Boltzmann constant
L	Latent heat (J/kg)
$\dot{m}$	Mass transfer (kg/m^3s)

M_L	Langevin function magnetization (A/m)
Ms	Saturation volume magnetization (A/m)
m	Magnetic moment of a single nanoparticle (Am^2)
m_{slug}	Magnetic moment of the slug (Am^2)
n	Particle concentration (number of iron particles per unit volume) ($1/m^3$)
n_∞	Mean number of particles in the chain
N	Number of solenoid turns
p	Pressure (Pa)
q	Heat transfer rate (W)
q”	Heat flux (W/m^2)
r	Mass transfer time relaxation parameter (1/s)
R	Radius (m)
s	Length of the solenoid (m)
S	Source term
T	Temperature (K)
t	Time (s)
Δt	Time step (s)

V	Volume (m^3)
v	Velocity (m/s)
v_0	Average velocity (m/s)
z	Displacement (m)

Subscripts

a	Average
c	Condenser
e	Evaporator
l	Liquid
v	Vapor

CHAPTER I: INTRODUCTION

1.1 Electromagnetic Energy Harvesting

1.1.1 Background

Electromagnetic-based energy harvesting materials and devices have emerged as a prominent research area in the last ten years, which continues to grow at a rapid pace. These energy harvesters have a wide range of applications including structural health monitoring using distributed wireless sensor nodes, embedded sensing for medical technologies, non-contact battery charging of large systems, monitoring tire pressure in automobiles, powering unmanned vehicles, and powering and controlling security systems in businesses and households.

The fundamentals of electrodynamic energy harvesting were discovered nearly two centuries ago. In 1821 Michael Faraday invented the electric motor by setting up his experiment with a permanent gyration of a current carrying wire in a magnetic field. It is possible to explain the conversion from mechanical to electrical energy by the law of induction found by Faraday which can be expressed as

$$E_I = -N\frac{d\Phi}{dt}. \tag{1-1}$$

where E is the induced EMF, N is the number of turns of the solenoid, Φ is the magnetic flux, t is the time.

1.1.2 Ferrofluids

Ferrofluids have recently attracted attention for use as electromagnetic induction materials and/or thermal transport media in energy harvesting devices. Ferrofluids are nanoscale colloidal suspensions of magnetic particles in a liquid carrier (organic or aqueous solvent). The surfaces of

these particles can be modified with small molecules, surfactants, or polymers to prevent aggregation thus maintaining the stability of the system. Due to their magnetic properties, they also demonstrate a potential for energy harvesting in thermal management applications. When a ferrofluid moves relative to a solenoid, ferrofluidic induction can occur resulting in electrical voltage generation. Compared to conventional permanent magnets, ferrofluids have the advantage of being suspendable and conforming to any shape channel or vessel. Therefore, ferrofluids can be easily extended to new designs and complex geometries of next-generation electromagnetic energy harvesters.

The principle of the ferrofluid energy harvesters is to use the motion of the ferrofluid within the external magnetic field to generate a time-varying magnetic flux to induce an electromotive force in the solenoid adjacent to the ferrofluid. There are several designs of the ferrofluid energy harvesters. Most of these energy harvesters employ the sloshing motion of the ferrofluid inside the container. For example, Daqaq et al. [1.3] designed vibration energy harvester by putting the ferrofluid in a seismically excited tank within an external magnetic field generated by two coaxially magnetized permanent magnets. Kim et al. [1.11] designed a magnetic circuit consisting of a rectangular container partially filled with ferrofluid, two groups of permanent magnets on the top and bottom of the ferrofluid container, an iron yoke made of ferromagnetic material connected with top and bottom permanent magnets, and two induction coils winding around the yoke as a vibration energy harvester. Some other studies use the pulsating motion of the ferrofluid inside the pipe. For instance, Monroe et al [1.7,1.9] investigated the electromagnetic induction process from a ferrofluid charged oscillating heat pipe (OHP).

1.2 Overview of Thermosyphon

1.2.1 Background

Heat pipes are the two-phase heat transfer devices without any external pumping. Heat pipes have emerged as efficient cooling and cost-effective devices due to their excellent heat transfer capabilities. A two-phase closed thermosyphon (TPCT) is a special heat pipe where the condensed liquid in the condenser falls back to liquid pool inside the evaporator by gravity without any capillary structure. Compared to the conventional heat pipe, the TPCT can operate over wider heat transfer and temperature ranges since it does not have the large flow resistance or low boiling limit inside the wick. Hence the TPCT has broad application in the chemical and petroleum industry, electronics cooling, telecommunication devices, energy storage systems, railway transportation systems, thermoelectric power generators, seasonal cooling load reduction of buildings, and solar energy systems.

1.2.2 Operating Principle

A TPCT consists of three parts: an evaporator, an adiabatic section, and a condenser. In a TPCT, the condenser is located above the evaporator so the condensate liquid in the condenser can be returned to the evaporator. In such a device, the input power is supplied through the outer wall of the evaporator to the liquid pool inside the TPCT. The liquid contained inside the evaporator starts to evaporate, and those vapor flow tends to move upward until it hits the inner wall of the condenser, which is condensing the vapor back to the liquid phase. The condensate liquid film tends to move downward along the inner of the TPCT until it reaches back to the liquid pool in the evaporator. This is how the working fluid circulate inside the TPCTs. Figure 1.1 is schematic overview of the TPCT.

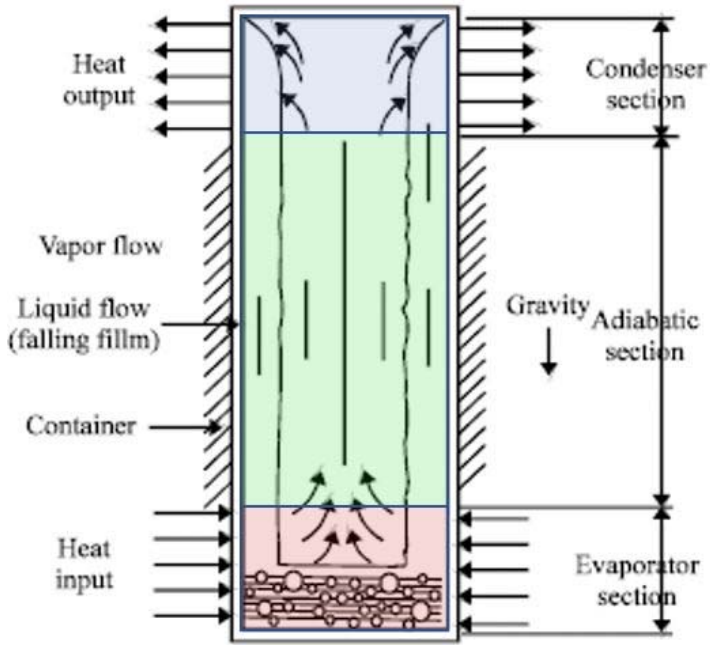

Figure 1.1. Schematic overview of a TPCT.

1.2.3 Current Work

The wide application of TPCTs has led to increasing interests among researchers and various experimental and numerical studies have been performed to investigate their performance. Among the numerical studies, computational fluid dynamics (CFD) models have been developed by several researchers to simulate the complex heat and mass transfer processes inside TPCTs using commercially available software packages such as ANSYS FLUENT. One challenge for CFD research is to determine an accurate and efficient method to simulate the complex flow, heat transfer and phase change processes inside TPCTs in order to predict performance characteristics relevant to engineering design.

When conducting the CFD simulation on the heat transfer and phase process inside TPCTs, an important consideration is to effectively simulate the amount of the mass transfer between the liquid and vapor phases of the working fluid during the evaporation and condensation process. The

most common approach for researchers is to use the mass transfer time relaxation parameters for evaporation and condensation within the Lee model to control the amount of mass transfer between the two phases of the working fluid insider TPCTs. Among the early researchers, the most popular choice for the mass transfer time relaxation parameters for evaporation and condensation are both equal to 0.1. Some following researchers use a transient value for the condensation mass transfer time relaxation parameter while keeping the mass transfer time relaxation parameter constant [1.31]. Some other researchers use transient values for both the mass transfer time relaxation parameters for evaporation and condensation [1.29,1.30]. Kim et al. [1.28] is the only researcher who suggested that the choice of mass transfer time relaxation parameters should consider the mass transfer balance inside the TPCT by adjusting these parameters based on the density ratio of the liquid phase and the vapor phase. In this study, four different sets of mass transfer time relaxation parameters for condensation and evaporation selected based on the method suggested by Kim et al. were incorporated within the Lee phase change model to determine their impact on the accuracy and efficiency of CFD simulation of a TPCT.

Another important consideration is the simulation of the interface of the two-phase flow inside the TPCT. Among these studies, the Geo-Reconstruct method is the most popular discretization scheme for the volume fraction equation since this scheme is able to capture the sharp interface between the liquid and vapor phases of the working fluid. One key limitation of the Geo-Reconstruct scheme is that the time step size must be relatively small compared to other volume fraction discretization schemes to prevent divergence of the simulation. In order to increase the time step size, a dispersed, second-order upwind interface scheme (QUICK) employed within the VOF formulation has been employed by some researchers [1.25,1.31-1.32]. It is also worth pointing out that the saturation temperature of the working fluid inside the TPCTs is set to

a fixed value in all of the CFD simulations except one study proposed a pressure-based phase change model instead of the more popular used Lee model to overcome the problem of thermal balance self-adjustment [1.36]. In this work, a more dispersive VOF discretization scheme is compared with the Geo-Reconstruct scheme in an effort to increase the maximum time step size allowable for stable simulation. In addition, a user-defined function (UDF) within the VOF model is proposed to maintain the appropriate filling ratio during simulation by globally varying the saturation temperature in response to the net interphase mass transfer.

As for the boundary conditions for the evaporator and the condenser of the TPCTs, the most common combination is the constant heat flux for the evaporator and the convective heat transfer boundary condition for the condenser in most CFD studies. However, some researchers use the constant heat flux boundary conditions for both the evaporator and condensers of TPCTs [1.19,1.25]. Some researchers use the convective heat transfer boundary conditions for both the evaporator and condenser of TPCTs [1.26,1.27]. There are also some other CFD simulations on TPCTs not specifying the details of the methods they are using [1.34,1.35]. In this study, there are two types of combinations of boundary conditions. When a fixed saturation temperature of the working fluid is employed, both the boundary conditions for the evaporator and the condenser are constant heat flux. When the UDF is incorporated to vary the saturation temperature of the working fluid, the boundary condition for the evaporator still remains to be constant heat flux while the convective heat transfer boundary condition and constant heat flux boundary condition were both tested in different cases. Table 1.1 and Table 1.2 summarize the methods employed in TPCT CFD simulations using the Geo-Reconstruct and QUICK discretization schemes, respectively.

Table 1.1. Review of TPCT simulation in the literature using the Geo-Reconstruct discretization scheme for the VOF model.

Mass transfer time relaxation parameters		**Boundary condition**		**Reference**
Evaporation	**Condensation**	**Evaporator**	**Condenser**	
0.1	0.1	Constant heat flux	Constant heat flux	[1.19]
0.1	0.1	Constant heat flux	Convective heat transfer	[1.20] [1.21] [1.22] [1.23] [1.24] [1.33]
Equal, values not specified		Convective heat transfer	Convective heat transfer	[1.26]
0.1	1000	Convective heat transfer	Convective heat transfer	[1.27]
0.1	Based on the density ratio of the liquid phase and the vapor phase	Constant heat flux	Convective heat transfer	[1.28]
Transient		Constant heat flux	Convective heat transfer	[1.29] [1.30]

Table 1.2. Review of TPCT simulation in the literature using the QUICK discretization scheme for the VOF model.

Mass transfer time relaxation parameters		**Boundary condition**		**Reference**
Evaporation	**Condensation**	**Evaporator**	**Condenser**	
0.1	0.1	Constant heat flux	Constant heat flux	[1.25]
0.09 0.3 0.5	Transient	Constant heat flux	Convective heat transfer	[1.31]
0.1	Transient	Constant heat flux	Convective heat transfer	[1.32]

1.3 Overview of Oscillating Heat Pipe

1.3.1 Background

An oscillating heat pipe (OHP), or pulsating heat pipe (PHP), is a passive heat transfer device that was developed by Akachi [1.37]. There are three main types of OHPs: closed loop oscillating heat pipes (CLOHP); closed loop oscillating heat pipes with additional check valves; and open loop oscillating heat pipes. Most researchers believe the heat transfer performance of CLOHP is better than the other two types due to the circulation of the working fluid within the pipe. Also, the CLOHP is the most common type of OHP. In this study, the CLOHP is referred as OHP. The OHP has the advantage of a simple structure, since they do not contain any wick structure. OHP also has the advantage of compact size compared to the conventional heat pipes, making them more flexible in different configurations. Hence the OHP has broad application in electronic cooling, solar collectors, fuel cell cooling, micro electronic devices, and many more.

1.3.2 Operating Principle

The OHP is made from a long capillary tube bent into several turns with no wick structure. It consists of three parts: an evaporator, an adiabatic section, and a condenser. Heat received in the evaporator leads to the evaporation of the liquid and generates bubble. The size of bubbles grows and increase in the vapor pressure. This causes the motion of the fluid towards the condenser. Then condensation happens at the condenser by heat dissipation. The growth and collapse of those bubbles result in the oscillating behavior of working fluid inside the OHP. Figure 1.2 is a schematic overview of an OHP.

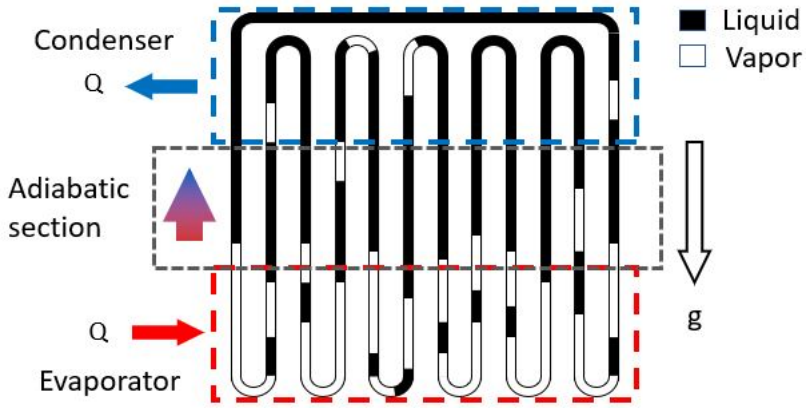

Figure 1.2. Overview schematic of an OHP system and operation.

1.3.3 Current Work

The wide application of OHPs has led to increasing interest among researchers and various experimental and numerical studies have been performed to investigate their performance. The most common approach for early researchers is to use the VOF model to simulate the interface of the two-phase flow inside the OHPs. Among all these studies, the Geo-Reconstruct scheme is the most popular discretization scheme for the volume fraction equation, since this scheme is able to capture the sharp interface between the liquid and vapor phases of the working fluid. Another approach for researchers to simulate the two-phase flow inside OHPs is using the mixture model [1.59]. They even did a comparison of these two methods. Similarly, some researchers use the dispersed interface to increase the time step size of the simulation. In their study, the QUICK scheme was employed to discretize the volume fraction equations. Table 1.3 is a summary of the CFD simulations on the OHP using the VOF model. Transient RANS simulation is also employed to investigate the thermal performance of CLPHP with different filling ratios [1.60]. Some other researchers have performed CFD simulations on the OHP but without specifying the methods used.

Table 1.3. Review of literature using the volume of fluid (VOF) model.

Interface	Volume discretization scheme	Reference
Sharp	Geo-Reconstruct	[1.41-1.43]
Dispersed	Not specified	[1.44, 1.45]
Dispersed	QUICK	[1.59]

CHAPTER II: ANALYTICAL MODEL FOR ELECTROMAGNETIC INDUCTION IN PULSATING FERROFLUID PIPE FLOWS

Energy harvesting processes using ferrofluidic induction—a process that generates voltage via the pulsation of a ferrofluid (iron-based nanofluid) through a solenoid—have received increasing attention over the past decade. In this paper an analytical model is proposed to predict the induced electromotive force (EMF) based on the flow behavior and magnetic properties of a pulsating ferrofluid energy harvesting device. The ferrofluid is treated as an idealized series of discrete magnetic 'slugs' passing through the solenoid, and the model identifies key parameters for describing and optimizing ferrofluidic induction in pulsating pipe flows. The resulting expression for induced EMF as a function of slug position relative to the solenoid is numerically integrated to determine the root mean square (RMS) of EMF during one pulsation cycle. Data from a previously documented study using an experimental induced EMF test rig is analyzed to find corresponding measured values of EMF RMS and used to validate the analytical model. Experimental and analytical results both show an increase in induced EMF with higher pulse frequency, increased number of bias magnets, and reduced spacing between the magnet and solenoid. Furthermore, experimentally measured values of EMF lie within the uncertainty bounds of the model resisted, indicating that induced EMF can potentially be predicted within an order of magnitude for these types of energy harvesting systems.

Keywords: analytical model, ferrofluidic induction, ferrofluid, pulsating flow, energy harvesting, solenoid

2.1 Introduction

2.1.1 Ferrofluids

Ferrofluids have recently attracted attention for use as electromagnetic induction materials and/or thermal transport media in energy harvesting devices [2.1-2.10]. Ferrofluids are nanoscale colloidal suspensions of magnetic particles in an organic or aqueous liquid carrier. The surfaces of these particles can be modified with small molecules, surfactants, or polymers to prevent aggregation thus maintaining the stability of the colloidal system despite thermal cycling and even phase change. In comparison to the base carrier liquid, ferrofluids have higher viscosities and thermal conductivities, and consequently demonstrate improved conductive and convective heat-transfer performance [2.1-2.2]. Due to their magnetic properties, they also show potential for energy harvesting in thermal management applications. When a ferrofluid moves relative to a solenoid, ferrofluidic induction can occur resulting in electrical voltage generation. Compared to conventional permanent magnets, ferrofluids have the advantage of being suspendable and conforming to any shape channel or vessel; therefore, ferrofluids can potentially be extended to new designs and complex geometries for next-generation electromagnetic energy harvesters.

2.1.2 Experiments Examining Ferrofluids for Energy Harvesting

Most energy harvesting systems employ the sloshing motion of the ferrofluid inside the container. For example, Sansom et al. [2.1] experimentally investigated the use of commercially available ferrofluids for waste heat removal, power conversion, and energy harvesting applications. In their study, three aqueous ferrofluids were tested in a tubular structure (10 mm ID) placed adjacent to a copper coil inductor with the intention of producing an EMF across the inductor. It was observed that the ferrofluid system acted as a thermal pump and had a thermomechanical conversion efficiency (mechanical movement realized/input thermal energy) of

0.13%. Chen et al. [2.3] also demonstrated the feasibility of ferrofluid energy harvesting both experimentally and theoretically. In their experiments, a series of cylindrical plastic containers filled with various amounts of ferrofluids were driven through pairs of induction coils. The induced EMF magnitudes increased with the relative fractional ferrofluid-volume inside the container (filling ratio) and the velocity of the ferrofluid moving through the coils. To further investigate the use of ferrofluids for energy harvesting, Bibo et al. [2.4-2.5] conducted a series of experiments using an external magnetic field formed by two axially arranged permanent magnets. A time-dependent voltage was generated across a solenoid by the vibratory motion of a container containing magnetized ferrofluid. These results not only demonstrated the potential for ferrofluid-based energy harvesting but also showed the impact of fluid column height, external magnetic field strength, and container acceleration on the measured voltage response; it was concluded that there exists a maximum output voltage for a given column height. Similarly, Kim et al. [2.6-2.7] also designed a setup for harvesting energy from the 'sloshing' motion of a ferrofluid. The setup consisted of a rectangular container partially filled with ferrofluid, two groups of permanent magnets on the top and bottom of the ferrofluid container, an iron yoke made of ferromagnetic material connected with top and bottom permanent magnets, and two induction coils winding around the yoke. Experiments with this setup showed that the volume of the ferrofluid inside the container and the permanent magnetic field strength affect the output voltage in the coils.

Our group has previously conducted experiments to investigate electromagnetic induction in a ferrofluid-charged oscillating heat pipe (FF-OHP) [2.8,2.9]. This system resulted in a harvested, peak-to-peak solenoid voltage around 1 mV from passive (temperature difference) oscillation in the FF-OHP with the nanoparticle magnetic poles aligned by a bias electromagnetic field. Recently, Choi et al. [2.10] presented a ferrofluid-based vibration energy harvester with a

hybrid triboelectric-electromagnetic operating mechanism. The apparatus included a cylindrical tube half-filled with ferrofluid, two separate aluminum electrodes on the top and bottom of the tube, a 200-turn of wire coil around the outside of the tube, and a permanent magnet at the bottom of the cylinder to provide a bias magnetic field. Compared to conventional solid-solid contact-based generators, the device demonstrated the advantage of operating under very weak vibrations while still generating measurable voltage amplitudes.

2.1.3 Modeling Ferrofluids in Magnetic Fields

While several different ferrofluid-based electromagnetic energy harvesting apparatuses have been examined experimentally, the ability to compare and optimize designs is limited without predictive analytical and computational modeling methods. To this end there have been only a few prior modeling studies focused on understanding and predicting the behavior of pulsating ferrofluids. In designing an electromagnetic energy harvester for ferrofluid sloshing motion, Kim et al. [2.7] used finite element numerical simulation to determine the magnetization distribution along/within an energy harvester, with the goal of optimizing magnetization by changing the back yoke shape. Ozbey et al. [2.11] used commercially available COMSOL Multiphysics® software to simulate ferrofluid flows driven by varying external magnetic fields in small channels. Their modeling results showed that velocity profiles along the tube were not constant and were affected by the magnetic field gradient. Berthier and Ricoul [2.12] used MATLAB® to develop a numerical model for instabilities in ferrofluid plug flow in a capillary tube near a permanent magnet. It was concluded that sudden velocity changes of the ferrofluid slug near the magnet resulted in the ferrofluid slug breaking up into smaller slugs, and this was confirmed by experimental measurements. Papadopoulos et al. [2.13] performed a numerical analysis of ferrofluid flow in a pipe under the influence of a magnetic field induced by cylindrical coils. In their study, the axial

pressure gradient of the ferrofluid flow near the edges of the coils was found to increase linearly with the volumetric concentration of nanoparticles in the ferrofluid.

Besides serving as the working fluid in electromagnetic energy harvesting devices, ferrofluids also have many applications in the biomedical field, and related modeling studies have been performed to study the transport behavior of magnetic particles within an external magnetic field. For example, Furlani et al. [2.14] presented numerical models to analyze and optimize the magnetofection process, in which magnetic particles are used to deliver gene vectors to target cells for uptake, in multiwell cell culture plate systems. Using these models, several key parameters influencing particle transport and accumulation were identified, such as particle size, magnet-to-wall spacing, position and concentration of particles in a well, and relative orientation of magnetic fields from neighboring magnets. Khashan et al. [2.15] used computational fluid dynamics (CFD) to design a microfluidic system capable of separating magnetic (or 'magnetically-labeled') particles. Integrated flow-invasive soft-magnetic elements were employed for the CFD model. The numerical model helped demonstrate that the magnetofection process has substantial performance advantages over conventional bioseparation systems by increasing the capture efficiency in specific regions of the channel due to the short-range nature of the magnetic force.

Application of an accurate numerical model can potentially help to drive process improvement, such as the bioseparation method described above. To the authors' knowledge a comprehensive analytical or numerical model has not yet been developed to predict output voltage for use in the analysis and design of ferrofluid energy harvesting processes based on the pulsating motion of a ferrofluid flow. Such a model would allow for the prediction of generated induced electromotive force based on ferrofluid properties, geometric details of the solenoid and pipe/tube system, and any imposed or generated magnetic fields. This analytical study investigates key

design parameters that are known to affect ferrofluidic induction, such as the number of bias magnets, magnet spacing, fluid pulse frequency, and ferrofluid particle diameter, to develop a relatively simple analytical model. The resulting model is validated against available experimental data.

2.2 Analytical Model

2.2.1 Model Description

To better understand energy harvesting processes using ferrofluid induction due to pulsating flow, an analytical model is developed and validated using the experimental results of Monroe et al. [2.16]. The basis for this effort is a model developed to describe the electromagnetic induction process from a solid cylindrical magnet with a uniform magnetization M passing through a circular wire ring [2.17], but extended to apply to a slug of magnetic ferrofluid. Induced EMF is generated by the relative motion between the magnetic slug and the solenoid. As the slug first enters the solenoid, a voltage (induced EMF) is generated due to a sudden change of magnetic flux inside the solenoid. While the slug moves through the solenoid the induced EMF is zero since the magnetic flux inside the solenoid remains constant. As the slug leaves the solenoid, an induced EMF (opposite sign) is generated due to a sudden inversion of the magnetic flux inside the solenoid (Figure 2.1).

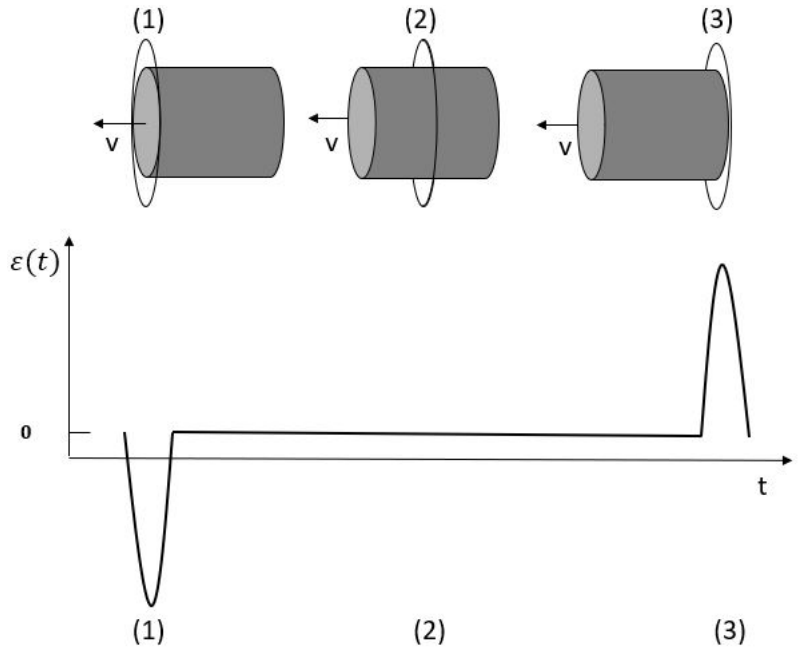

Figure 2.1. Electromagnetic induction of a cylindrical magnetic slug passing through a circular wire.

As mentioned previously, ferrofluids are composed of two components, magnetic nanoparticles, that are treated as magnetic dipoles, and a liquid carrier. In the absence of an external magnetic field, the magnetic moments of the particles are randomly oriented. When an external magnetic field is applied, the magnetic dipoles align to produce a net magnetic moment that is parallel to the external field, as is shown in Figure 2.2. The experimental study [2.16] used to validate the induced EMF analytical model utilized an external magnetic field. Therefore, the analytical model adopts the point of view that the ferrofluid within the tube can be approximated as a cylindrical pseudo-slug consisting of uniformly magnetized material as it flows through the solenoid.

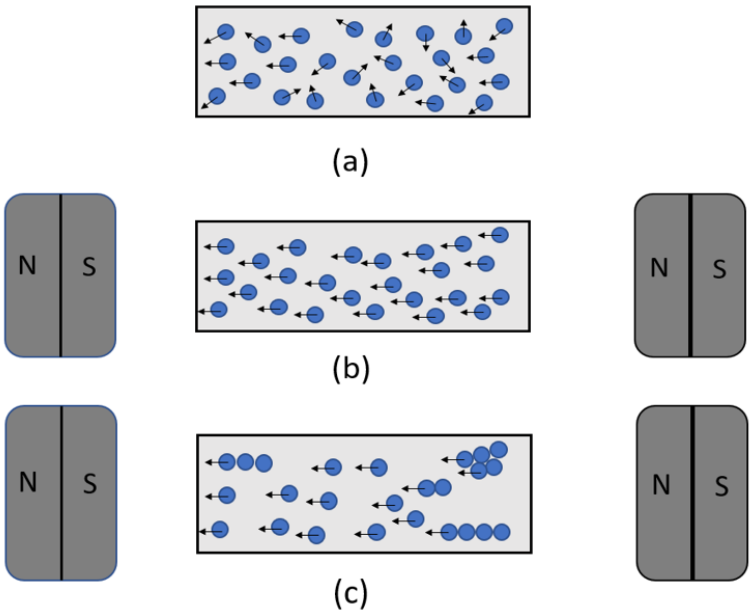

Figure 2.2. Schematic diagram of the ferrofluids with (a) no bias field, (b) applied bias field showing alignment of dipole moments of the suspended magnetic nanoparticles, and (c) potential chain structure formation.

The magnetic moment of a cylindrical slug can be calculated as

$$m_{slug} = M_s \times V. \tag{2-1}$$

where m_{slug} is the magnetic moment of the slug, M_s is the volume saturation magnetization of the slug, and V is the volume of the slug.

The analytical model starts with the motion of a point dipole passing through a single loop [18]:

$$e_1(z) = \frac{3\mu p_m R^2 vz}{2(R^2+z^2)^{5/2}} \tag{2-2}$$

where μ is the magnetic permeability, p_m is the magnetic moment of the dipole, R is the radius of the solenoid loop, v is the axial velocity of the dipole, and z is the relative axial position between

the dipole and the solenoid loop. Assuming each infinitesimal 'slice' of a magnetic slug with length L acts as a dipole, then a differential induced EMF can be defined as

$$de_1(z) = \frac{3\mu m_{slug} R^2 vz}{2L(R^2+z^2)^{5/2}}\, dz. \tag{2-3}$$

where the magnetic moment of each differential dipole is assumed to be

$$p_m = \frac{m_{slug}}{L}\, dz. \tag{2-4}$$

Defining the slug position z to correspond to the centroid of the slug and integrating over the slug length gives the induced EMF as

$$E_1(z) = \int_{-L/2}^{L/2} \frac{3\mu m_{slug} R^2 v[z+\xi]}{2L[R^2+(z+\xi)^2]^{5/2}}\, d\xi. \tag{2-5}$$

Evaluating the integral yields

$$E_1(z) = \frac{\mu m_{slug} R^2 v}{2L}\left\{\frac{1}{[R^2+\left(z-\frac{L}{2}\right)^2]^{\frac{3}{2}}} - \frac{1}{[R^2+\left(z+\frac{L}{2}\right)^2]^{\frac{3}{2}}}\right\}. \tag{2-6}$$

We now consider the induced EMF of a magnetic slug passing through a solenoid of length S with N loops. Defining the loop spacing as $\Delta = S/(N-1)$, the induced EMF from all loops can be summed to yield

$$E_{total}(z) = \sum_{i=0}^{N-1} E_1(z + S/2 - i\Delta). \tag{2-7}$$

Here $z = 0$ corresponds to the center of the solenoid. For cases in which $\Delta \ll R$, the induced EMF through the solenoid can be approximated using an integral over the length of the solenoid

$$E_{total}(z) = \frac{1}{\Delta}\int_{-N\Delta/2}^{N\Delta/2} E_1(\xi)\, d\xi. \tag{2-8}$$

and for $N \gg 1$, the induced EMF can be approximated as

$$E_{total}(z) = \frac{N}{S}\int_{-S/2}^{S/2} E_1(z+\xi)\, d\xi. \tag{2-9}$$

Evaluating the integral yields the total induced EMF from a finite length slug passing through a solenoid with N loops, radius R, and length S

$$E_{total}(z) = \frac{N\mu m_{slug} v}{2LS}\left\{\frac{z-\frac{L}{2}+\frac{S}{2}}{\left[\left(z-\frac{L}{2}+\frac{S}{2}\right)^2+R^2\right]^{\frac{1}{2}}} + \frac{z+\frac{L}{2}-\frac{S}{2}}{\left[\left(z+\frac{L}{2}-\frac{S}{2}\right)^2+R^2\right]^{\frac{1}{2}}} - \frac{z+\frac{L}{2}+\frac{S}{2}}{\left[\left(z+\frac{L}{2}+\frac{S}{2}\right)^2+R^2\right]^{\frac{1}{2}}} - \frac{z-\frac{L}{2}-\frac{S}{2}}{\left[\left(z-\frac{L}{2}-\frac{S}{2}\right)^2+R^2\right]^{\frac{1}{2}}}\right\}. \tag{2-10}$$

2.2.2 Pulsating Motion

In the experimental setup of Monroe et al. [2.16], the pulsating motion of the ferrofluid through the tube was controlled using a peristaltic pump. This same pump setup was also used to perform a separate flow visualization experiment employing pure water as the working fluid in order to characterize the velocity and flow behavior of a liquid slug. Water was chosen for this visualization experiment since the ferrofluid carrier liquid is water and the pulsating fluid motion could be tracked using the interfaces between the liquid slugs and intentionally introduced air bubbles. To capture the fluid motion, a high-speed camera (Phantom Miro 310, Vision Research Inc., 640x480 resolution, 300 frames per second) was used to collect video and measure the velocity of the fluid at different pumping frequencies. Figure 2.3 shows a static image of the liquid slug/bubble flow captured using the high-speed camera.

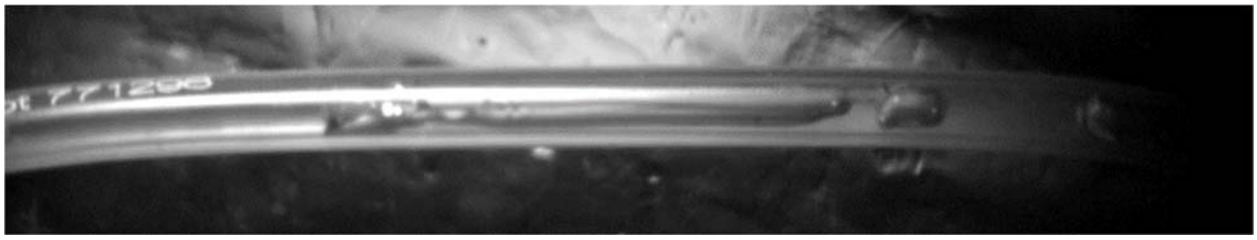

Figure 2.3. Static image from a high-speed video of water/air slugs pumped at approximately 6 Hz through tubing used in experimental setup [2.16].

Analyzing the high speed-camera video of the water/air slug flow, the slug displacement, *D*, for a single pulse averaged 4.11 +/- 0.09 cm over the 6-30 Hz frequency range tested. The average velocity of the slug was estimated as $\mathrm{v}_0 \cong \mathrm{D}/\Delta\mathrm{t}$. Since the peristaltic pump consisted of three rollers in sequence, the time period of each flow displacement within the tube was approximately $\Delta\mathrm{t} \cong 1/(3f)$, where f is the pumping frequency of the peristaltic pump. Pumping frequencies and associated average pulse velocities for the ferrofluid slug are listed in Table 2.1. Since fluid pulsation was observed to be nearly harmonic with the cyclic pump frequency, the velocity profile of the magnetic slug moving through the solenoid is assumed to follow

$$v(t) = v_0[1 - \cos(\omega t)]. \tag{2-11}$$

where v_0 is the average velocity and $\omega = 2\pi f$. The displacement of the of the slug is therefore

$$z(t) = v_0\left[t - \frac{\sin(\omega t)}{\omega}\right] + z_0. \tag{2-12}$$

where z_0 is the initial position of the slug.

Table 2.1. Water/air slug pulse velocities for experimentally tested frequencies.

Pulsating frequency f (Hz)	**Time period Δt (s) (+/- STDEV)**	**Average pulsating velocity v_0 (m/s) (+/- STDEV)**
3	0.11 ± 0.006	0.33 ± 0.02
6	0.05 ± 0.001	0.84 ± 0.02
10	0.03 ± 0.002	1.40 ± 0.07

2.2.3 Ferrofluid Characterization

To provide appropriate inputs to the analytical model, it is critical to understand the ferrofluid microstructure, i.e., the particle distribution inside the liquid carrier. Some studies [2.19] have shown that large-sized, chain-like magnetic structures can form within the ferrofluid due to dipolar interactions between the magnetic nanoparticles. Yoon et al. [2.20] studied the equilibrium structures of ferrofluid aggregates within a magnetic field and showed that dipoles can form chain-like structures which can evolve into larger-scale 2D and 3D multichain assemblies as the system size increases. In this study, transmission electron microscopy (TEM) was employed to characterize the morphological characteristics of the in-house synthesized ferrofluid used in the experiments [2.16].

A representative TEM image of the magnetic nanoparticles from the ferrofluid is shown in Figure 2.4. The nanoparticles are dispersed, and the small amount of aggregation observed is likely due to the drying process necessary for TEM imaging. The distribution of measured particle diameters is shown in Figure 2.5; the average particle diameter was found to be 10.1 nm with a standard deviation of 0.16 nm. With a nanoparticle diameter of 10.1 nm, the volume of each nanoparticle is 5.4×10^{2} nm^3. The mass of a single spherical nanoparticle is calculated to be 4.6×10^{-22} kg, using a Fe_3O_4 nanopowder density of 850 kg/m^3 [2.22]. The experimentally determined physical properties of the in-house synthesized ferrofluid used in this study are summarized in Table 2.2.

No significant chain-like structures were observed in the ferrofluid TEM images (Fig. 2.4). This result is expected since with TEM imaging, the sample is not examined under a magnetic field and further is dried prior to being subjected to vacuum conditions. Therefore, with standard

TEM it is not possible to visualize the formation of chains or other aggregate structures that might occur for magnetic nanoparticles suspended in solution within a magnetic field.

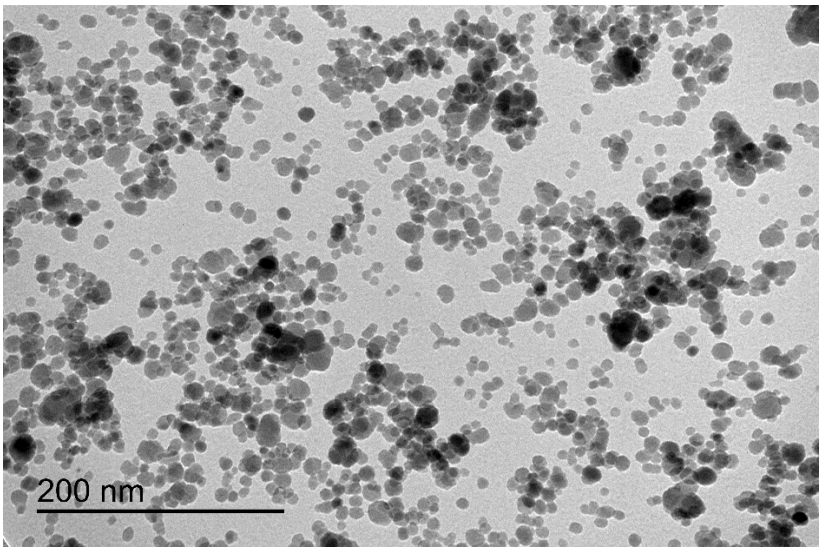

Figure 2.4. TEM image of Fe_3O_4 magnetic nanoparticles from the in-house aqueous ferrofluid.

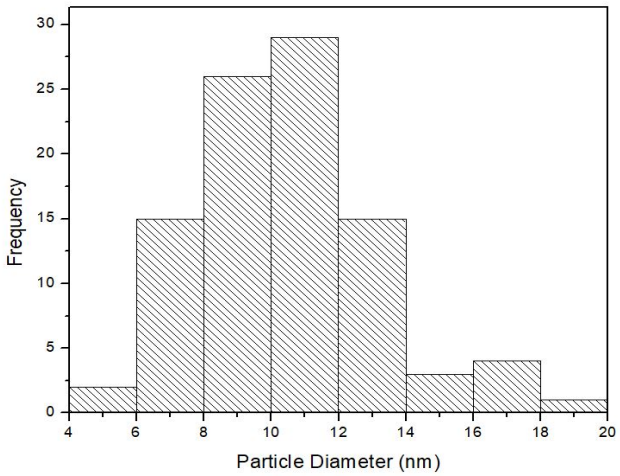

Figure 2.5. Particle size distribution of iron oxide nanoparticles from the ferrofluid used in the EMF flow loop experiments.

Table 2.2. Physical properties of in-house synthesized ferrofluid.

	Average
Fe_3O_4 weight percentage (%)	10.97
Fe weight percentage (%)	7.94
Density of the ferrofluid (g/cm^3)	1.10
Diameter of nanoparticle (nm)	10.1 ± 0.16

2.2.4 Magnetic Properties of the Ferrofluids

As mentioned previously, in the absence of an applied magnetic field, nanoparticle magnetic moments are randomly oriented, and the ferrofluid has no net magnetization. Once an external magnetic field is applied, magnetic moments of the dipoles tend to align with the applied field. The net magnetization of the ferrofluid increases as the field strength increases, and at relatively high field strengths, magnetic moments of the dipoles may become completely aligned. A limit occurs when magnetization reaches its saturation value, a phenomenon known as superparamagnetism. The saturation volume-magnetization of a ferrofluid, M_s, depends on magnetic particle concentration (number of Fe_3O_4 particles per unit volume) and the magnetic moment of individual nanoparticles [2.22]. Considering the magnetic moments of each nanoparticle, the saturation volume-magnetization (M_s) within a volume of ferrofluid can be determined as $M_s = n \times m$ [2.22]. The magnetic moment of nanoscale Fe_3O_4 powder has been found to range from 12.3 emu/g to 85.8 emu/g [2.21], therefore the magnetic moment of each nanoparticle, m, is dependent on its mass. The density of nanoscale Fe_3O_4 powder has been found to be 850 kg/m^3 [2.21]. These Fe_3O_4 nanopowder properties were used for calculating the magnetic properties of the in-house ferrofluids used in this study.

Two additional important parameters to consider regarding the magnetization of the ferrofluid are the magnetic susceptibility, χ, and permeability, μ. The initial susceptibility, χ_i, after

taking into account the interaction between the magnetic moments of the particles is determined by [2.22]:

$$\frac{\chi_i(2\chi_i+3)}{\chi_i+1} = 24\phi\lambda. \quad (2\text{-}13)$$

and the permeability is

$$\mu = \mu_0(1+\chi_i). \quad (2\text{-}14)$$

The magnetic properties calculated for the in-house synthesized ferrofluid from the above governing equations are listed in Table 2.3. As mentioned previously, both experimental and modeling studies have shown that in strong external fields the ferromagnetic nanoparticles tend to form chain-like structures parallel to the field direction [2.19,2.20]. Under these conditions the mean number of nanoparticles in the chain can be calculated as

$$n_\infty = [1 - \frac{2}{3} * \left(\frac{\phi}{\lambda^2}\right) * e^{2*\lambda}]^{-1}. \quad (2\text{-}15)$$

where ϕ is the nanoparticle volume fraction. The dipolar coupling coefficient can be calculated as

$$\lambda = \frac{\mu_0 * m^2}{4*\pi*d^3*k*T}. \quad (2\text{-}16)$$

where m is the magnetic moment of one single iron oxide particle, μ_0 is the permeability of the free space, $\mu_0 = 4\pi \times 10^{-7}\ N/A^2$, k is the Boltzmann constant, $k = 1.38 \times 10^{-23}\ J/K$, T is the absolute temperature ($T = 293$ K), and d is the diameter of magnetic core of the nanoparticle.

Table 2.3. Magnetic properties of the in-house synthesized ferrofluid containing Fe_3O_4 nanoparticles.

Volume fraction, ϕ (%)	14.5
Particle concentration, n (#/m^3)	2.65×10^{23}
Magnetic moment of a single nanoparticle, m (emu)	5.65×10^{-18} - 3.94×10^{-17}
Magnetic moment of a single nanoparticle, m (Am^2)	5.65×10^{-21} - 3.94×10^{-20}
Saturation volume-magnetization, M_s (kA/m)	1.5 - 10.4
Saturation mass-magnetization, σ_s (emu/g)	1.35 - 9.43
Dipolar coupling coefficient, λ	7.66×10^{-4} - 3.73×10^{-2}
Initial susceptibility, χ_i (N/A^2)	8.90×10^{-4} - 4.4×10^{-2}
Permeability, μ_F (N/A^2)	1.26×10^{-6}- 1.31×10^{-6}

The magnetic flux density, B, of the applied bias magnetic field was measured by a DC Gaussmeter (GM-1-ST, AlphaLab, Inc., 0.1 G resolution, 1% accuracy). Since the length of the solenoid was relatively small (about 2 cm), it is assumed that the magnetic flux density inside the solenoid can be approximated as constant. The magnetic flux density in the center of the solenoid is used as the magnetic field strength of the applied bias magnetic field. The locations of the magnets were varied to be either 10.2 cm, 15.2 cm, or 20.3 cm from the center of the solenoid, and the resultant magnetic flux densities measured are listed in Table 2.4. The magnetic flux density of two bias magnets was exactly double that of one bias magnet.

Table 2.4. Bias magnetic field parameters as a function of magnet number and offset.

Number of Magnets	Magnet Offset / Spacing (cm)	Magnetic Flux Density B (mT)
1	20.3 cm	0.3
2	20.3 cm	0.6
1	15.2 cm	0.7
2	15.2 cm	1.4
1	10.2 cm	2.1
2	10.2 cm	4.2

The magnetization of the ferrofluid in the presence of an applied bias magnetic field and saturation magnetization can be characterized using the Langevin function [2.22],

$$M_L(B) = n * m * \left[coth(\alpha) - \frac{1}{\alpha}\right] = n * m * L(\alpha) \quad (2\text{-}17)$$

where n is the particle concentration, m is the magnetic moment of one single iron particle, and $\alpha = (m * B)/(k * T)$ is the Langevin parameter, the ratio of the field interaction to the thermal energy. For each configuration of the magnets shown in Table 2.4, the magnetization for the ferrofluid "slug" in Eq. (10) was calculated using Eq. (2-17).

2.3 Experimental Methods

2.3.1 Ferrofluids Selection

To investigate the concept of ferrofluid induction, Monroe et al. [2.16] previously performed a series of experiments that investigated water and two different aqueous Fe_3O_4 ferrofluids as the working fluids, one of the ferrofluids was a commercially-available (Ocean NanoTech) material with a concentration of 10 mg/mL and the second was an in-house synthesized ferrofluid with a concentration of 100 mg/mL The low-concentration commercial product was found to provide negligible improvement over pure water (negative control) in terms of EMF generation, so only the in-house ferrofluid experimental data is used as a reference for the present

study. The aqueous ferrofluid, containing iron oxide (Fe_3O_4) particles was synthesized as described in [2.16] with perchloric acid as a surface stabilizer [2.8].

2.3.2 Ferrofluids Characterization

The weight percentage of Fe_3O_4 in the synthesized ferrofluid was determined from measuring the ferrofluid mass before and after evaporation of the water and drying of the solids. The iron weight percentage is based on the theoretical stoichiometric value. The density of the ferrofluid was determined by weighing known volumes of the solution. Additional details on the synthesis method and characterization of the aqueous ferrofluid are available in [2.8].

For transmission electron microscopy (TEM) imaging of the ferrofluid samples, the magnetic nanoparticles were suspended in Nanopure™ water with 20 min of sonication. A drop of the ferrofluid samples (5 μL drop volume) was then placed on 300 mesh carbon film coated TEM grids. After allowing the water to evaporate, the TEM grids were treated with glow discharge before imaging with a JEOL JEM-1400 electron microscope. Image J software was used to measure the outer diameter of the nanoparticles (n = 60). The thickness of the surface ligand used to prevent nanoparticle agglomeration was neglected since it was comprised of perchloric acid ($HClO_4$, MW = 100.46 g/mol).

2.3.3 EMF Test Rig Design and Operation

The in-house synthesized ferrofluid, comprised of Fe_3O_4 particles with a particle diameter ~10 nm in water, was circulated through 3.2 mm ID Tygon® tubing using a peristaltic pump (Cole Parmer Model 7553-20). The tubing was oriented horizontally to minimize any gravitational effects. A 1000-turn copper wire solenoid with an outer diameter of 12.7 mm was made from 0.13 mm copper wire wrapped around a tubular core (3.2 mm ID and 127 cm length). To examine the impact of magnet number and position on ferrofluid induction, either one or two neodymium

magnets (each a 16.4 cm^3 cube) were placed at different distances from the midpoint of the solenoid. The experimental setup parameters, including magnet offset, are listed in Table 2.5. Figure 2.6 shows a schematic of the induced electromotive force (EMF) experimental test rig setup.

Table 2.5. Parameters for ferrofluidic induction experiments performed by Monroe et al. [2.16].

Parameter	**Value**
Number of bias magnets	1, 2
Pulse frequency	3 Hz, 6 Hz, 10 Hz
Ferrofluid	Fe_3O_4 + H_2O (100 mg/mL)
Magnet offset	10.2 cm, 15.2 cm, 20.3 cm
Solenoid core	Plastic (Tygon®)
Solenoid number of turns	1000
Solenoid inner diameter	3.2 mm
Solenoid outer diameter	12.7 mm
Solenoid length	20.0 mm

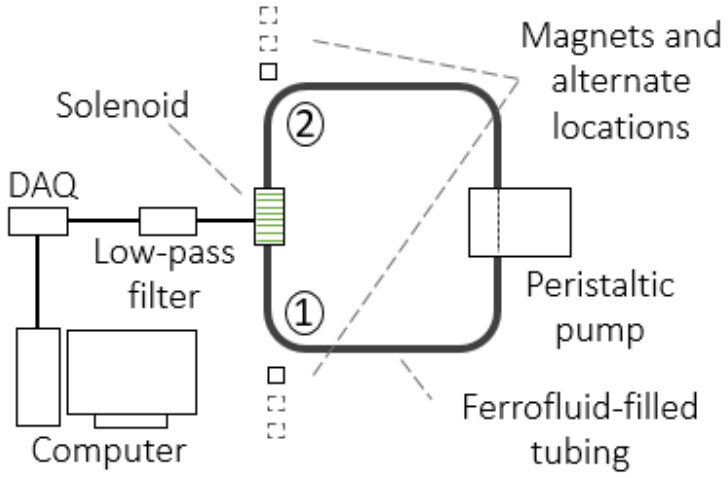

Figure 2.6. Ferrofluidic induction experimental setup [2.16] where labels ① and ② indicate the magnet positioning/offsets in the induced electromotive force (EMF) flow loop.

2.4 Results and Discussions

The analytical model presented in section 2.2 was validated against experimental data of pulsating ferrofluid flow from Monroe et al. [2.16]. For test rig experiments, the measured induced EMF was generated by a continuous pulsating ferrofluid flow being passed through the solenoid. In the analytical model, the continuous pulsating ferrofluid flow was treated as trains of magnetic "slugs" passing through the solenoid.

For each experimental EMF test rig set-up, the root mean square (RMS) value of the induced EMF measured in [2.16] was calculated and used as a single metric to quantify effective voltage and validate the analytical model. Examining the RMS value of the induced EMF calculated from the experimental data shown in Table 2.6, the RMS value of the induced EMF is 13.9 μV when there is no external magnet or when the pumping frequency is zero. Hence, 13.9 μV RMS was treated as the baseline noise value for the overall experimental set-up.

Table 2.6. RMS values of the induced EMF ($\boldsymbol{\mu V}$) from experimental data in [2.16].

Magnetic flux density B (mT)	**0 Hz**	**9 Hz**	**18 Hz**	**30 Hz**
0	13.9	13.9	13.9	13.9
0.3	13.9	13.8	13.9	14.1
0.6	13.9	14.0	14.1	14.6
0.7	14.0	14.0	14.1	14.9
1.4	13.9	14.1	14.4	16.6
2.1	14.0	14.2	15.3	18.6
4.2	13.9	14.5	17.4	23.8

The RMS value of the noise was subtracted from the measured RMS values allowing the effects of pumping frequency and magnetic flux to be more clearly identified (Table 2.7). The RMS values of the induced EMF increased with both pumping frequency and magnetic flux density, as expected. Low magnetic flux density (0.3 mT) at either of the lower pumping

frequencies (9 Hz and 18 Hz) resulted in nominally zero measured RMS, since the induced EMF due to the pulsating flow was small relative to the baseline noise. At the lowest pumping frequency (9 Hz), the RMS value of the induced EMF was relatively small (< 1 μV) at all magnetic flux densities. When the pumping frequency was increased to 18 Hz, the RMS value of the induced EMF calculated from the experimental data was < 1 μV until the magnetic flux density exceeded 2.1 mT. At all frequencies, the RMS value of the induced EMF increased by a factor of two or more when the magnetic flux density was doubled from 2.1 mT to 4.2 mT. At a pumping frequency of 30 Hz, the induced EMF RMS is >1 μV for all magnetic flux densities was greater than 0.7 mT. Similarly, at a low magnetic flux density (≤ 0.7 mT) the RMS value of the induced EMF was small (≤ 1 μV) at all pumping frequencies. As the magnetic flux density was increased above 0.7 mT, the RMS value of the induced EMF increased significantly as a function of increased pumping frequency. The RMS value of the induced EMF experiment increased more than two-fold when the magnetic flux density was doubled.

Table 2.7. Induced EMF RMS values ($\boldsymbol{\mu V}$) adjusted for experimental noise [2.16].

Magnetic flux density B (mT)	**9 Hz**	**18 Hz**	**30 Hz**
0.3	0	0	0.2
0.6	0.1	0.2	0.7
0.7	0.1	0.2	1.0
1.4	0.2	0.5	2.7
2.1	0.3	1.4	4.7
4.2	0.6	3.5	9.9

Since there are multiple unknown parameters related to the experimental conditions and ferrofluid material properties, a sensitivity analysis was performed to examine the response of the model for induced EMF to small differences in the input variables. Some of the model input

variables were well defined in the flow-loop experiment [2.16]: operating temperature; ferrofluid density; magnetic flux density; tube diameter; solenoid radius; solenoid length; and number of turns of the solenoid. The average slug velocity passing through the solenoid was estimated from video captured by high-speed camera. Values for density and magnetic moment of nanoscale Fe_3O_4 powder in the ferrofluid were obtained from literature sources [2.21].

Table 2.8 shows the percentage change in the calculated output voltage for a 1% increase in each of the model input variables. In terms of general trends, the induced EMF increases with larger solenoid radius, length, and turn number, and with lower operating temperature. The induced EMF shows a linear trend with magnetic flux density, length of the slug, length of the solenoid, and average slug velocity passing through the solenoid. Compared to other input variables, the particle diameter has the greatest impact with an increase of 3.69% on the induced EMF in the analytical model. The density of ferrofluid has the least impact on the induced EMF with an increase of 0.22% compared with other input parameters.

Table 2.8. Sensitivity analysis showing the percent change in calculated voltage for a 1% increase in each of the model input parameters.

Input parameter	**Induced EMF Change**
Particle diameter (d)	3.69%
Operating temperature (T)	-1.19%
Density of ferrofluid (ρ_{ferro})	0.22%
Magnetic flux density (B)	1.00%
Density of nanoscale Fe_3O_4 powder (kg/m^3)	1.44%
Magnetic moment of nanoscale Fe_3O_4 powder (emu/g)	1.21%
Diameter of the tube (D)	2.00%
Radius of the solenoid (R)	-0.30%
Length of the slug (L)	1.00%
Length of the solenoid (S)	-1.00%
Number of turns of the solenoid (N)	-0.70%
Average slug velocity passing through solenoid (v_0)	1.00%

In the analytical model, an important consideration is determination of the effective length and volume of the magnetic ferrofluid slug. The diameter of the slug is assumed to be equal the tube internal diameter, $d = 3.2\ mm$. Hence the volume of the ferrofluid slug can be calculated as $V = \frac{\pi d^2 L}{4} = [8.04 \times 10^{-6}\ m^2] \times L$. The choice of slug length is not straightforward. Here we consider two characteristic length scales in the current setup, the length of the solenoid, $L = S = 2\ cm$, and the distance traveled by the fluid during one pulsation cycle, $L = 4.1\ cm$. For both lengths, the RMS of induced EMF was computed by numerically integrating Eq. (2-10) along the entire length of the slug. A minimum and maximum result was found by considering the valid ranges for key ferrofluid material properties, namely the values of magnetic moment for a single nanoparticle, m, and permeability, μ, listed in Table 2.3. Using the low and high parameter values

resulted in the EMF bounding values as determined by the analytical model. The slug velocity was assumed to be equal to the mean fluid velocity, v_0.

Figures 2.7-2.12 show the model prediction of induced EMF for the three pumping frequencies at each of the magnetic flux densities tested. The difference between the minimum and maximum model prediction due to uncertainty in the ferrofluid properties is approximately two orders of magnitude for all cases. Relative to the range of results from considering material property differences, the impact on the model results from the two different slug lengths is small. Notably, the experimental data falls between the model bounds for all cases except for the two lowest frequencies when $B = 3\ mT$. For this case, as discussed above, the induced EMF was too small in the experiments to be differentiated from the background noise (Table 2.7), so these data points are not included in the plots.

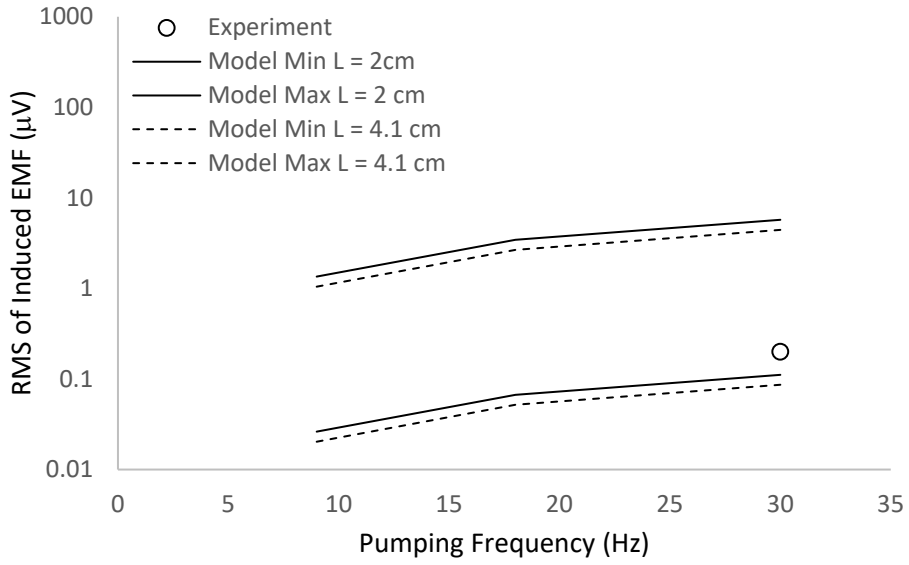

Figure 2.7. Comparison of the experimental and analytical values of induced EMF as a function of pumping frequency for magnetic flux density $\boldsymbol{B = 0.3\ mT}$.

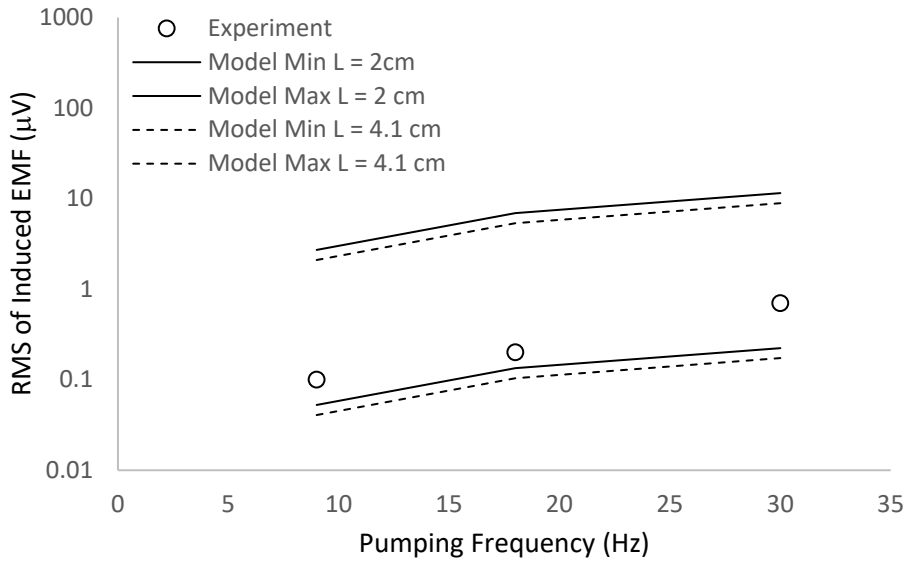

Figure 2.8. Comparison of the experimental and analytical values of induced EMF as a function of pumping frequency for magnetic flux density $\boldsymbol{B = 0.6\,mT}$.

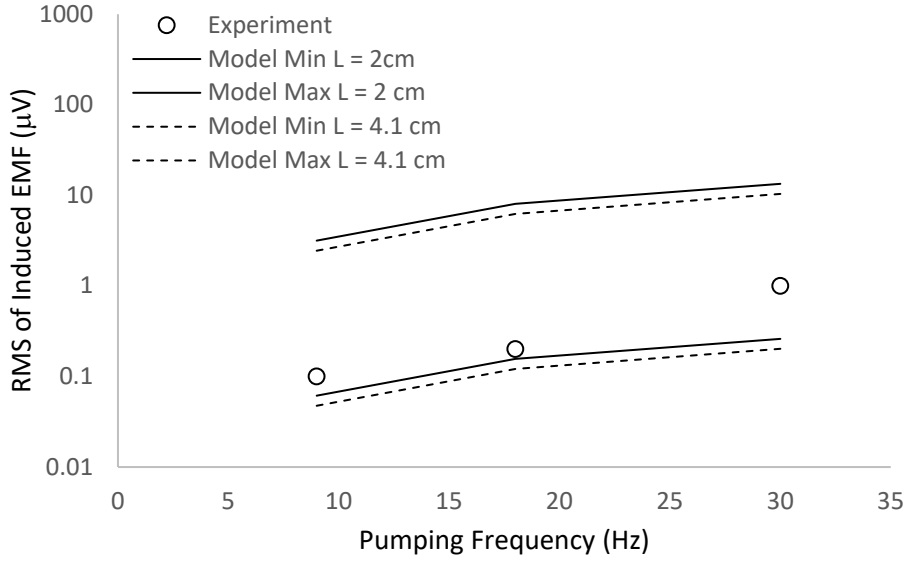

Figure 2.9. Comparison of the experimental and analytical values of induced EMF as a function of pumping frequency for magnetic flux density $\boldsymbol{B = 0.7\,mT}$.

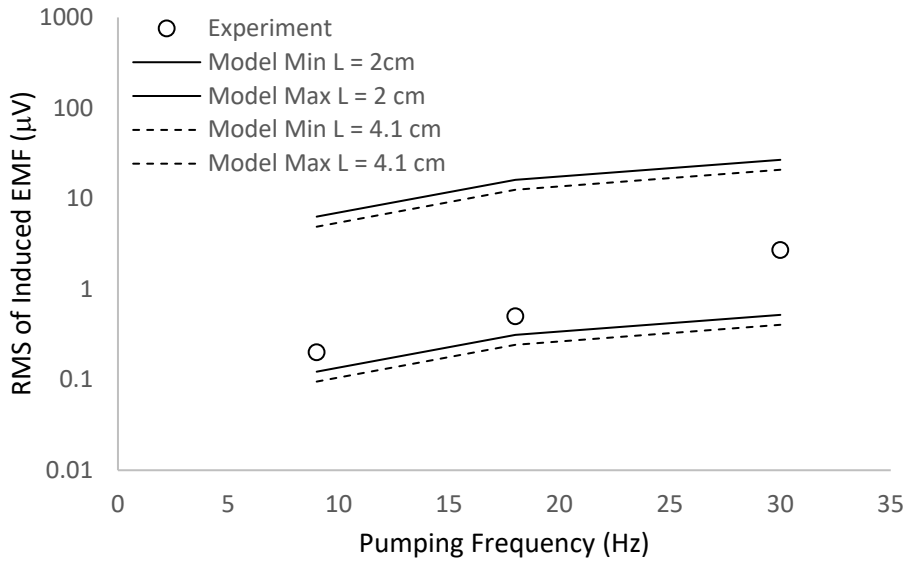

Figure 2.10. Comparison of the experimental and analytical values of induced EMF as a function of pumping frequency for magnetic flux density $\boldsymbol{B = 1.4\,mT}$.

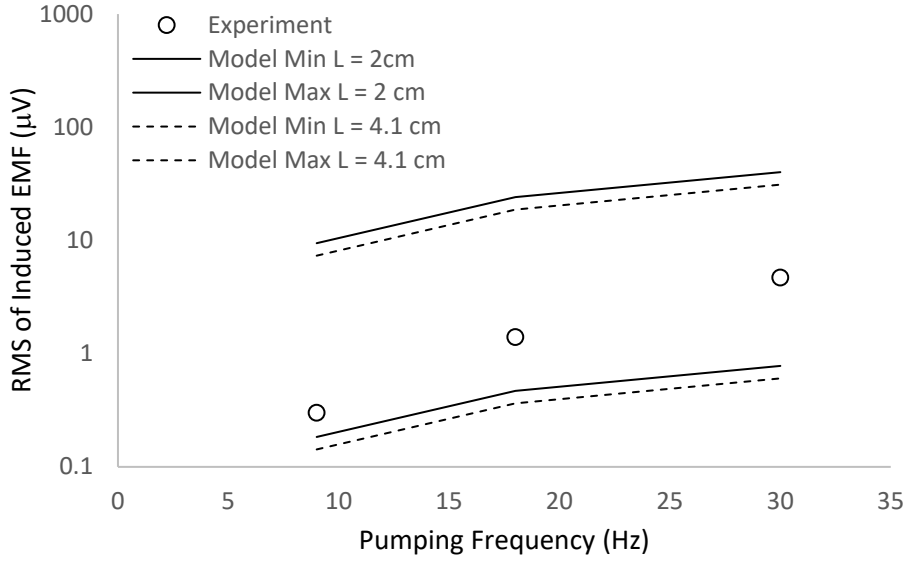

Figure 2.11. Comparison of the experimental and analytical values of induced EMF as a function of pumping frequency for magnetic flux density $\boldsymbol{B = 2.1\,mT}$.

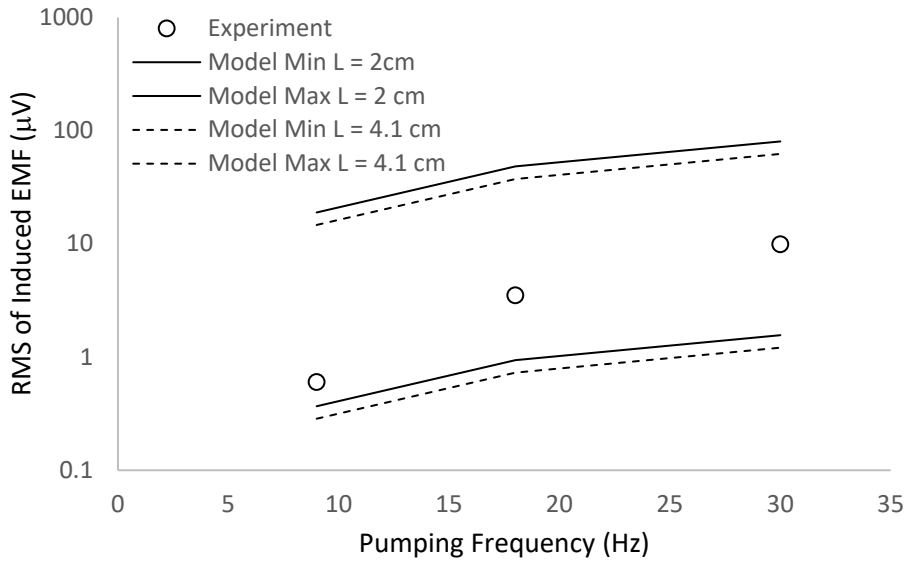

Figure 2.12. Comparison of the experimental and analytical values of induced EMF as a function of pumping frequency for magnetic flux density $\boldsymbol{B = 4.2\,mT}$.

In addition to the uncertainty in the ferrofluid properties discussed above, additional error in the model is likely present due to difficulties in accurately quantifying the slug velocity when the magnetic field is applied. There is likely inaccuracy due to the imaging method used to obtain the water/air slug velocity. In addition, differences in velocity are expected between the ferrofluid flow and water/air mixed flow inside the tube. In the high-speed camera experiment, the water/air flow was driven only by the pump without any external force. In the ferrofluid flow-loop experiment, there is an additional attractive force on the flow due to the bias magnetic field and also more complex multiphase flow. The additional force will tend to accelerate the fluid motion along the direction of the bias magnetic field, especially when the ferrofluid first enters the bias magnetic field (position ① or ② in Figure 2.6). This acceleration is due to a large pressure drop along tube axis which occurs when there is a large magnetic field gradient. This phenomenon was confirmed by Papadopoulos et al. [2.13] in their numerical model of the ferrofluid pipe flow under an external magnetic field generated by a coaxial finite solenoid. In their model, this large pressure drop was present at the entrance and exit of the solenoid coils, where large field-gradients exist. In

the system investigated herein, this pressure drop occurs close to the surface of the bias magnet where there is a large magnetic gradient. As a result, the actual velocity of the ferrofluid 'slug' passing through the solenoid should be greater than that measured for water/air flow in the high-speed video. Examining Eqn. (2-10), an increase in the speed of the 'slug' passing through the solenoid will result in an increase the RMS value of the induced EMF.

Both the experimental data and analytical model show the same trend with the RMS value of the induced EMF increasing as a function of pulsating frequency, since higher pulse frequencies lead to faster relative motion between the solenoid and magnetic slug. Also, the induced EMF is demonstrated both analytically and experimentally to increase with a stronger external magnetic field as a higher percentage of the ferrofluid nanoparticle moments are aligned. Besides, the analytical model shows that the induced EMF would decrease with operating temperature. These outcomes relating higher pulsating frequencies and external magnetic fields to larger induced EMF agree well with the experimental results from other researchers [2.3-2.5]. By adjusting these parameters, the magnetic moment of slug and subsequently the induced EMF across the solenoid can potentially be controlled and/or optimized.

2.5 Conclusions

The analytical model developed in the present work predicts induced EMF due to a pulsating ferrofluid passing through solenoid-equipped tubing. The basis of the model is the assumption that the pulsating fluid is analogous to a series of cylindrical slugs moving through the induction coil. Starting from the expression for induced EMF from a single point dipole, an expression for EMF versus relative position between the slug centroid and solenoid centroid is obtained. The expression can then be integrated to determine the RMS value of EMF for a given set of conditions.

The model inputs include properties of the ferrofluid, magnetic field, solenoid, and fluid flow. As a consequence, it potentially can be tailored to a wide range of EMF generation systems. Experimental data from an energy harvesting process that employed pulsating ferrofluid motion driven by a peristaltic pump was used to validate the model. Uncertainty in the model inputs was included by obtaining minimum and maximum prediction of induced EMF for each test case. The two extrema were found in the present case to differ by approximately two orders of magnitude.

The analytical model generated was able successfully predict induced EMF from a solenoid for pulsating ferrofluids. The trends with respect to both magnetic flux density and pumping frequency were correctly reproduced, and the experimental EMF values were between the minimum and maximum for all cases, with the exception of the two operating conditions for which the experimental values were nominally zero. Overall, the results suggest that the modeling approach adopted here is valid for these magnetic fluid-induced energy harvesting configurations, although further work is needed to fully validate and optimize the modeling methodology for general ferrofluid energy scavenging applications.

CHAPTER III: INVESTIGATION OF NUMERICAL SCHEME AND MODEL COMBINATION FOR CFD SIMULATION OF A TWO-PHASE CLOSED THERMOSYPHON

Computational fluid dynamics simulations were performed to predict the heat transfer performance of a two-phased closed thermosyphon (TPCT). Simulations were performed using a three-dimensional finite-volume flow solver (ANSYS Fluent) with a pressure-based scheme for the solution of the continuity and momentum equations, volume-of-fluid method for resolution of the liquid-vapor phase interface, and temperature-dependent model for interphase mass transfer by evaporation and condensation. Both liquid and vapor phase densities were assumed to be independent of pressure. which is in line with most previous studies. Several different model and numerical scheme combinations were investigated in an effort to identify an appropriate method for efficient and consistently accurate results using currently available software tools. An initial set of simulations was performed using a constant value for the saturation temperature, constant heat flux boundary condition in the evaporator section, and convection boundary condition in the condenser section, similar to several published TPCT simulation studies. Using this method the simulations did not converge to a stationary state for which the net heat transfer rate is equal to zero, and the cause was identified to be an inappropriate combination of boundary conditions and fixed saturation temperature that resulted in overconstrained system temperatures. This problem was successfully mitigated by applying a constant heat flux boundary condition for both evaporator and condenser sections. Simulations using the previously published methods were also found to violate conservation of mass, due to the inability of the simulated system to provide the pressure-based feedback and thermal self-adjustment that occurs in real physical systems, which is a consequence of the fluid density assumptions and the use of a pressure-based numerical scheme. To address this issue, a new model for variable saturation temperature was proposed and a test

suite of simulations was performed using the new model and different combinations of boundary condition and VOF discretization scheme, including the Geo-Reconstruct scheme and the Compressive scheme available in Fluent. Values of the mass transfer model coefficients were also varied to determine their impact on simulation accuracy. Results using both constant heat flux and convection condenser boundary conditions show that the variable saturation temperature model significantly mitigates mass and energy imbalance in the simulations. Results using the Geo-Reconstruct scheme were found to be more accurate than with the Compressive scheme, due to the ability of the former to preserve a sharp interface between the liquid and vapor phases. It was also found that, when used with the variable saturation temperature model and appropriate values of the mass transfer coefficients, the computational cost of the Geo-Reconstruct scheme was comparable to the Compressive scheme. The results of this study highlight critical aspects of the solution methodology that must be addressed for simulation of the TPCT and provide a recommended solution strategy. Most importantly, the results show that simulations should adopt some method to include appropriate system response to changes in vapor/liquid total mass fraction (in this case a variable saturation temperature model), and that the commonly used approach of pressure-independent fluid properties and constant saturation temperature is likely to yield accurate results only with a judicious (if not lucky) choice of boundary conditions, numerical scheme, and model coefficients.

3.1 Introduction

A heat pipe is a passive heat transfer device with no internal or external pumping in which a working fluid is driven by the temperature gradient between the evaporator and condenser. The two-phase closed thermosyphon (TPCT) is a type of heat pipe for which the condensed liquid returns to the evaporator section due to gravity, with no need for a capillary wicking structure. A

TPCT consists of an evaporator, adiabatic section, and condenser, and the condenser must be located above the evaporator so the condensate liquid can be return by gravity to the evaporator. Compared to a conventional heat pipe, a TPCT can operate over a wider temperature range since it does not have the large flow resistance or low boiling limit that occurs within a wick. The absence of active pumping combined with wider operating temperatures has resulted in broad application of TPCTs in the chemical and petroleum industries, electronics cooling, telecommunication devices, energy storage systems, railway transportation systems, thermoelectric power generators, seasonal cooling load reduction in buildings, and solar energy systems [3.1]. In the last decade TPCT research has increased and several experimental and numerical studies have been performed to investigate their design and performance. Among the numerical studies, computational fluid dynamics (CFD) models have been developed to simulate the complex heat and mass transfer processes inside TPCTs. The key challenge for CFD research of a TPCT is to determine an accurate and efficient method to simulate phase change and two-phase flow. Critical aspects include the boundary conditions and the phase transfer model to accurately simulate the condensation and evaporation processes. Other important considerations are the choice of domain, such as whether to use a two-dimensional (axisymmetric) or three-dimensional representation, and whether or not to include heat conduction across the thermosyphon wall in the simulation. There is currently no standard, well-validated methodology for simulating TPCTs, and determination of accurate and efficient simulation strategies remains an active area of research.

The most common approach for CFD simulation of TPCTs found in the open literature uses the volume-of-fluid (VOF) method to simulate the two-phase interface [3.2-3.17]. When applying the VOF model to examine the heat transfer and phase change, an important consideration

is effectively simulating mass transfer between the liquid and vapor phases of the TPCT working fluid during the evaporation and condensation processes. The most common approach for researchers has been to use mass transfer time relaxation parameters for evaporation and condensation to control the mass transfer rate between the two phases of the working fluid inside TPCT. Among early researchers the most popular choice was to use 0.1 for both the evaporation and condensation mass transfer time relaxation parameters. Alizadehdakhel et al. [3.2] performed a 2D analysis using 0.1 for these parameter values to investigate the heat transfer performance and optimum filling ratio of TPCTs. Another 2D CFD study was performed by Fadhl et al. [3.3-3.4] on phase change behavior inside a TPCT with different working fluids including water, R134a, and R404a. Jouhara et al. [3.5] extended Fadhl's CFD model from 2D to 3D specifically focusing on the geyser boiling phenomenon, a flow pattern that arises in a thermosyphon at low heat input rates. Fadhl's 2D CFD model was also used by Alammar et al. [3.6] to investigate the heat transfer performance of TPCTs with different filling ratios and inclination angles. Song et al. [3.7] performed a 2D simulation of vapor-liquid two-phase flow during evaporation and condensation taking into account the relationship of superheating, subcooling, and wall heat flux using the same mass transfer time relaxation parameters for evaporation and condensation as Fadhl [3.3-3.5]. A 2D CFD simulation of a TPCT with a CuO/water as the working fluid was performed by Asmaie et al. [3.8].

Wang et al. [3.9] also used equal values for the evaporation and condensation mass transfer time relaxation parameters in their CFD modeling of geyser boiling. However, they asserted that the value of the condensation mass transfer time relaxation parameter should be 10-1000 times greater than the value of the evaporation mass transfer time relaxation parameter for a semi-steady state simulation of a TPCT. In another study Wang et al. [3.10] performed a 3D CFD simulation

to evaluate a new TPCT design consisting of a horizontal two-phase loop thermosiphon including a U-turn section to prevent bidirectional flow. In their model, the mass transfer time relaxation parameter for evaporation was set to 0.1 while the condensation parameter was set to 1000, with the parameter values selected based on experimental data. Kim et al. [3.11] pointed out the mass transfer being phases should be related to the ratio of the liquid and vapor phase densities. Four condensation mass transfer time relaxation parameter values were examined while holding the evaporation mass transfer time relaxation parameter fixed at 0.1. The authors concluded that the simulation results agreed best with the experimental data when the ratio of the condensation and evaporation mass transfer time relaxation parameters was equal to the ratio of the liquid and vapor phase densities.

Xu et al. [3.12] proposed transient mass transfer time relaxation parameters to simulate phase change processes inside a TPCT. Their simulation results showed that the CFD model with transient parameters had smaller relative errors in the temperature distribution along the TPCT wall than the model without transient parameters. Transient mass transfer time relaxation parameters were then incorporated into other CFD studies. In a later study Xu et al. [3.13] studied the effects of filling ratio and evaporator wettability using surface contact angles on TPCT heat transfer performance using the same CFD model as [3.12]. Similarly, Kafeel et al. [3.14] also utilized a transient mass transfer time relaxation parameter but only for condensation, while the evaporation parameter was held constant. Using this same methodology Kafeel et al. [3.15] also studied the thermal response of a TPCT subjected to pulsed heat input conditions. Wang et al. [3.16] examined the effect on simulation accuracy of different sets of mass transfer time relaxation parameters for evaporation and condensation with a different boundary condition for the condenser and a new selected saturation temperature of the working fluid. Their study confirms the

conclusion that the evaporation and condensation mass transfer time relaxation parameters should be selected such that their ratio is equal to the vapor-liquid density ratio suggested by Kim [3.11]. They also concluded that combining improved selections for the mass transfer time relaxation parameters along with appropriate saturation temperature and condenser boundary conditions resulted in a 3D CFD method that accurately modeled the continuous evaporation and condensation process in a TPCT, based upon comparison with experimental data.

In the studies discussed above, the Geo-Reconstruct method is the most popular discretization scheme for the volume fraction equation, since this scheme can capture the sharp interface between the liquid and vapor phases of the working fluid [3.2-3.7,3.9-3.13]. However, one key limitation of the Geo-Reconstruct scheme is that the time step size must be relatively small, in comparison to other volume fraction discretization schemes, to prevent divergence of the simulation. To increase the time step size, a dispersed, second-order upwind interface scheme (QUICK) within the VOF formulation has been employed by some researchers [3.8,3.14-3.15]. A detailed summary of the solution methods for prior TPCT studies is listed in Table 3.1. Note that the "convective" boundary condition refers to a Robin type with specified heat transfer coefficient and reference fluid temperature. The mesh size shown corresponds to the largest mesh size, in terms of cell count, used in the study.

Table 3.1. Summary of previous CFD simulations of TPCT.

Mass transfer time relaxation parameters		**Boundary condition**		**Mesh size (cells)**	**Reference**
Evaporation	**Condensation**	**Evaporator**	**Condenser**		
Geo-Reconstruct VOF Scheme					
0.1	0.1	Constant heat flux	Constant heat flux	61,485 (2D)	[2]
0.1	0.1	Constant heat flux	Convective	87,800 (2D)	[3]
0.1	0.1	Constant heat flux	Convective	129,944 (2D)	[4]
0.1	0.1	Constant heat flux	Convective	370.702 (3D)	[5]
0.1	0.1	Constant heat flux	Convective	34,142 (2D)	[6]
0.1	0.1	Constant heat flux	Convective	40,000 (2D)	[7]
Equal, values not specified		Convective	Convective	63,029 (2D)	[9]
0.1	1000	Convective	Convective	1,312,084 (3D)	[10]
0.1	Based on the liquid-to-vapor density ratio	Constant heat flux	Convective	80,000 (2D)	[11]
Variable		Constant heat flux	Convective	94,273 (2D)	[12]
Variable		Constant heat flux	Convective	74,780 (2D)	[13]
0.1 1 10	0.1 Based on the liquid-to-vapor density ratio	Constant heat flux	Constant heat flux	846,304 (3D)	[16]
QUICK VOF Scheme					
0.1	0.1	Constant heat flux	Constant heat flux	63,029 (2D)	[8]
0.09 0.3 0.5	Transient	Constant heat flux	Convective	68,000 (2D)	[14]
0.1	Transient	Constant heat flux	Convective	87,280 (2D)	[15]

The majority of CFD simulations of TPCTs are two dimensional. Of the studies discussed previously, only Refs. [3.5,3.10,3.16] are 3D simulations. Also, it is worth pointing out that the

most common boundary conditions for TPCT CFD simulations have combined a constant heat flux condition for the evaporator section and a convective heat transfer boundary condition for the condenser section. Only [3.2] and [3.8] employed a constant heat flux boundary condition for both the evaporator and the condenser, and only [3.9] and [3.10] used a convective heat transfer boundary condition for both the evaporator and the condenser. A critical consideration is that in all the above studies the saturation temperature of the working fluid inside the TPCTs is set to a fixed value. In contrast, Wang et al. [3.17] proposed a pressure-based phase change model instead of the more commonly used Lee model to overcome the problem of the thermal balance and self-adjustment. In their model, the saturation temperature is calculated by a fitting function, and the local mass and heat transfer rates during phase change are related to the difference between local pressure and saturation pressure. While the specific studies cited above have contributed significant improvement to CFD simulation of TPCTs, it is evident that no universally accepted methodology currently exists. Open research questions include whether or not the overall pressure-based CFD methodology using VOF is valid, whether or not it is appropriate to assume pressure-independent fluid properties, how to determine an appropriate value for saturation temperature and whether or not that value should be held constant, how well simulations satisfy global conservation laws, how to determine statistical convergence to a stationary (steady) state, how to determine appropriate values for mass transfer time relaxation parameters, and which numerical discretization schemes represent the best choice in terms of both accuracy and computational efficiency.

The overall objective of this study is to propose a determine a CFD modeling methodology that can accurately and efficiently simulate the realistic operational condition of TPCTs using general-purpose CFD software. The first aim is to evaluate the effects of mass transfer time

relaxation parameters on the accuracy of the simulation results using the most common approach, i.e. Geo-Reconstruct volume discretization scheme with a fixed system saturation temperature. The second aim is to investigate the Compressive scheme as a potentially robust and computationally efficient discretization scheme for the volume fraction equation. The goal of using the Compressive scheme is to allow for an increase in the time step size, relative to the more commonly used Geo-Reconstruct scheme, while preserving the two-phase interface and maintaining the accuracy of the simulations. The third aim is to determine the effects of two different condenser boundary conditions on the accuracy of the simulation results. The fourth aim is to investigate the use of a variable global value for the saturation temperature to enhance the physical realism of the simulations, improve accuracy, and reduce computational expense.

In the present effort, simulations were run using a full 3D computational domain and the simulation results were validated against experimental data available in [3.3]. To provide a baseline, CFD simulations using the same mass transfer time relaxation parameters for evaporation and condensation were conducted and results are compared with previous CFD simulations and experimental data [3.3,3.11]. These simulations show the impact of using a constant heat flux condenser boundary condition and a fixed saturation temperature for the working fluid. In this study a saturation temperature of 327.45 K was selected based on the details of the experimental setup [3.3]. In addition, four different sets of condensation and evaporation mass transfer time relaxation parameters were incorporated within the Lee [3.16] phase change model to determine their impact on the accuracy and efficiency of 3D CFD simulations of a TPCT. Instead of using a convective heat transfer boundary condition for the condenser, such as was used in [3.3] and [3.11], the boundary conditions for both the evaporator and the condenser were set to be constant heat flux in order for the simulation to reach a stationary state and to ensure that energy conservation

was satisfied. To increase the maximum time step size while still allowing for stable simulations, a more dispersive VOF discretization scheme is utilized and the results compared with the Geo-Reconstruct scheme. Additionally, a new model for variable saturation temperature is proposed and implemented within the VOF model to maintain the appropriate filling ratio during simulation by globally varying the saturation temperature in response to the net inter-phase mass transfer. Both the constant heat flux boundary condition and the convective heat transfer boundary condition for the condenser were tested to determine the effect on the accuracy of the simulation results.

3.2 Methods

Simulations were carried out using the commercial software ANSYS Fluent version 16.2. Computational grids were constructed using Pointwise version 17. The volume-of-fluid (VOF) model was used to simulate the two-phase flow and capture the interface between liquid and vapor phases. The Lee [3.18] model was employed to calculate the rate of interphase mass transfer in the vicinity of the phase interface during the evaporation and condensation processes. The continuum surface force (CSF) [3.19] model was employed to simulate the surface tension of the liquid-vapor interface.

3.2.1 VOF Model

In the two-phase VOF method, the volume fraction of each phase is computed as a dependent variable in each computational cell of the domain. One advantage of the VOF model is that it can simulate two immiscible fluids by solving a single momentum equation and tracking the volume fraction of each of the fluids throughout the domain. The phase interface is implicitly resolved as the region for which the volume fraction lies between the bounding values of 0 and 1.

One typical application of the VOF model is the prediction of the steady or transient tracking of any liquid-gas interface in saturated systems.

The tracking of the interface between phases is accomplished by solving the continuity equation for the volume fraction of the liquid and vapor phases. For the liquid phase

$$\frac{\partial(\alpha_l \rho_l)}{\partial t} + \nabla \cdot (\alpha_l \rho_l \vec{v}) = \dot{m}_{vl} - \dot{m}_{lv} \quad (3\text{-}1)$$

and conversely for the vapor phase

$$\frac{\partial(\alpha_v \rho_v)}{\partial t} + \nabla \cdot (\alpha_v \rho_v \vec{v}) = \dot{m}_{lv} - \dot{m}_{vl} \quad (3\text{-}2)$$

Here $\dot{m}_{lv}$ is the mass transfer rate from the liquid phase to the vapor phase due to evaporation, and $\dot{m}_{vl}$ is the mass transfer rate from the vapor phase to the liquid phase due to condensation, per unit volume. The density of the liquid and vapor phases is denoted by ρ_l and ρ_v, and the volume fraction is denoted by α_l and α_v, respectively. The volume fractions for the liquid and vapor phases must satisfy

$$\alpha_l + \alpha_v = 1. \quad (3\text{-}3)$$

In practice, therefore, only one of the phase volume fraction equations is solved along with the sum of Eqs. (3-1) and (3-2) as the continuity equation for the fluid mixture. The variables and properties in any given computational cell (finite control volume) are representative of the pure liquid phase, the pure vapor phase, or a mixture of the two phases. If α_l is the volume fraction of the liquid phase in the cell, the following three conditions are possible:

- $\alpha_l = 1$: The cell is fully occupied by the liquid
- $\alpha_l = 0$: The cell is fully occupied by the vapor
- $0 < \alpha_l < 1$: The cell contains the interface between the liquid and vapor phases

In the two-phase system, the volume-fraction-averaged density, dynamic viscosity, and effective thermal conductivity are computed based on a weighted average between phases:

$$\rho = \alpha_l \rho_l + (1 - \alpha_l)\rho_v \tag{3-4}$$

$$\mu = \alpha_l \mu_l + (1 - \alpha_l)\mu_v \tag{3-5}$$

$$k = \alpha_l k_l + (1 - \alpha_l)k_v \tag{3-6}$$

A single momentum equation for the fluid mixture is solved throughout the domain. The momentum equation is dependent on the volume fractions of the two phases through the mixture properties ρ and μ:

$$\frac{\partial(\rho\vec{v})}{\partial t} + \nabla \cdot (\rho\vec{v}\vec{v}) = -\nabla p + \nabla \cdot [\mu(\nabla\vec{v} + \nabla\vec{v}^T)] + \rho\vec{g} + \vec{F} \tag{3-7}$$

where $\vec{v}$ is the velocity vector, p is the pressure, $\vec{g}$ is the gravitational acceleration vector, and $\vec{F}$ is the surface tension force, which is discussed in detail in the next section.

Similarly, a single energy equation is also solved for the fluid mixture:

$$\frac{\partial(\rho E)}{\partial t} + \nabla \cdot [\vec{v}(\rho E + p)] = \nabla \cdot (k\nabla T) + S \tag{3-8}$$

Here T is the temperature and E is the mixture internal energy which is be defined based on phase volume fractions as:

$$E = \frac{\alpha_l \rho_l E_l + (1-\alpha_l)\rho_v E_V}{\alpha_l \rho_l + (1-\alpha_l)\rho_v} \tag{3-9}$$

S is a source term related to the phase change process, which can be expressed as

$$S = L(\dot{m}_{vl} - \dot{m}_{lv}). \tag{3-10}$$

where L is the latent heat of vaporization for the fluid.

3.2.2 Surface Tension

Surface tension may have a significant influence on the form of the liquid-vapor interface in the TPCT and must be taken into consideration in the CFD model. The continuum surface force (CSF) model [3.19] is applied here, for which the surface tension can be expressed in terms of the

pressure jump across the liquid-vapor interface. The force at the surface is incorporated as a source term in the momentum equation and has the form

$$\vec{F}_{CSF} = \sigma_{lv} \frac{\rho \kappa_l \nabla \alpha_l}{\frac{1}{2}(\rho_l + \rho_v)}. \quad (3\text{-}11)$$

where σ_{lv} is the surface tension between the liquid and vapor phases. In the present study, the surface tension is assumed to be temperature independent and selected based on the initial saturation temperature of the working fluid, and has the value $\sigma_{lv} = 0.067356$ N/m [3.20]. The variable κ is the local surface curvature, which can be approximated in terms of the volume fraction distribution as

$$\kappa = \nabla \cdot \left(\frac{\nabla \alpha_l}{|\nabla \alpha_l|}\right). \quad (3\text{-}12)$$

The wall adhesion angle in conjunction with the surface tension model is assumed to be 12.7°. This value is based on the experimental measurements in Ref. [3.21].

3.2.3 Evaporation - Condensation Model

The Lee model [3.18] is applied to calculate the mass transfer rate for the phase change processes, i.e. evaporation and condensation. The phase change is assumed to occur at a constant pressure and at a quasi-equilibrium thermodynamic state. The governing equations for the mass transfer are given by the following equations. For the evaporation process, if $T_l > T_{sat}$:

$$\dot{m}_{lv} = r_{lv} \alpha_l \rho_l \frac{(T_l - T_{sat})}{T_{sat}} \quad (3\text{-}13)$$

For the condensation process, if $T_v < T_{sat}$:

$$\dot{m}_{vl} = r_{vl} \alpha_v \rho_v \frac{(T_{sat} - T_v)}{T_{sat}} \quad (3\text{-}14)$$

Here T_l is the temperature of the liquid phase, T_v is the temperature of the vapor phase, and T_{sat} is the saturation temperature. The coefficients r_{lv} and r_{vl} are the mass transfer time relaxation

parameters, which are usually set to ad hoc values based on empirical experience. In the present study, four sets of mass transfer time relaxation parameters were used. For one set the evaporation and condensation time relaxation parameters were both equal to 0.1, the value most commonly used in the literature. For the other three sets, the ratio between condensation and evaporation constants is held constant and equal to the density ratio of saturated liquid to saturated vapor, as recommended in [3.11]. The values of these parameters are listed in Table 3.2.

Table 3.2. Mass transfer time relaxation parameters.

r_{lv} (s^{-1})	r_{vl} (s^{-1})
0.1	973.356
1	9733.56
10	97335.6

3.2.4 New Variable Saturation Temperature Model

As noted above, most previous studies assumed a constant value of saturation temperature for simulation of a TPCT [3.2-3.16]. In a real system, however, the saturation temperature varies in response to system pressure. If net mass transfer occurs from the liquid to the vapor phase, the system pressure increases, resulting in higher saturation temperature. The higher saturation temperature increases the rate of condensation relative to evaporation, effectively limiting the overall mass transfer and maintaining the filling ratio at or near its initial value. The opposite effect occurs, of course, if net mass transfer occurs from vapor to liquid phase.

For the pressure-based solution methodology used here and in most previous studies, the density of the liquid and vapor phases are assumed to be independent of pressure, which is treated as a mechanical variable only, not a thermodynamic state variable. As a consequence, the system pressure in the simulation does not respond to interphase mass transfer in a physically appropriate manner. This allows erroneous, non-physical levels of net mass transfer to occur in the simulations including complete dry out the liquid pool. Even for cases in which the results are not non-physical,

it may significantly delay convergence to a statistical steady state since the condenser and/or evaporator temperatures may converge to values far from their initialization values.

To address this issue, a new method is proposed in the present work to calculate the global value of saturation temperature based on the estimated global instantaneous average vapor pressure inside the TPCT. The instantaneous pressure is considered to be equal to the saturation pressure of the working fluid. The variation of this saturation pressure is calculated based on the volume change from liquid phase to vapor phase using the ideal gas law approximation to balance the mass transfer of the working fluid inside the TPCT. The initial saturation temperature of the system is selected as the temperature of the adiabatic section measured in the experiment [3.3]. The model equations for saturation temperature of the working fluid are summarized as below. From application of the ideal gas law approximation for the vapor phase:

$$P = \rho_v RT \tag{3-15}$$

The density of the vapor is here assumed to be a global (mean) quantity equal to the total mass of vapor divided by the volume of vapor in the TPCT:

$$\rho_v = \frac{m_v}{V_v} = \frac{(m - m_l)}{(V - V_l)} \tag{3-16}$$

where the total mass and volume in the TPCT system, m and V, are assumed to remain constant. Differentiating Eq. (3-15) yields

$$dp = \rho_v R\, dT + RT\, d\rho_v = \rho_v R \left(\frac{dT_{sat}}{dp_{sat}}\right) dp + RT\, d\rho_v. \tag{3-17}$$

From saturation tables for water, at an initial assumed saturation temperature of 54 deg C:

$$\frac{dT_{sat}}{dp_{sat}} \approx 0.0013 \frac{K}{Pa} \tag{3-18}$$

Substitution and simplification yields

$$dp = 1.06RT\, d\rho_v \approx RT\, d\rho_v. \tag{3-19}$$

In terms of the mass and volume of liquid in the system, this can be expressed as

$$dp \approx RT\left(\frac{m_v}{V_v^2}dV_l - \frac{1}{V_v}dm_l\right) \approx RT\left(\frac{\rho_v}{V_v} - \frac{\rho_l}{V_v}\right)dV_l \approx -RT\,\frac{\rho_l}{V_v}\,dV_l. \tag{3-20}$$

Assuming small changes in phase volume:

$$dV_l \approx (V_l - V_l^*) \approx (V_v^* - V_v) \tag{3-21}$$

To leading order, the linear relationship between saturation temperature and vapor volume can then be expressed as

$$\Delta T_{sat} \approx \left(\frac{dT_{sat}}{dp_{sat}}\right)\frac{\rho_l}{V_v^*}RT_{sat}^*(V_v - V_v^*). \tag{3-22a}$$

where starred quantities (e.g. V_v^*) represent initial values. More generally, this can simply be expressed as

$$\Delta T_{sat} = C(V_v - V_v^*). \tag{3-22b}$$

In practice, the coefficient C can be selected arbitrarily. It was found that values of C determined using Eq. (3-22a) were too large and resulted in very large swings in saturation temperature from one time step to the next in the simulations, with the result that the simulation was unstable. Too small values of C were not sufficient to prevent significant interphase mass transfer leading to large deviation from the initial filling ratio. Optimum selection of the value of the coefficient C is therefore based on a balance between simulation stability and accuracy, and the coefficient value can be determined for specific test cases using numerical experimentation. In the present study, it was found that a value of $C = 4.2 \times 10^6$ was effective in maintaining stability, while limiting the change in vapor volume to less than 10% of the initial vapor volume with a corresponding variation of saturation temperature of less than +/- 25 K during the course of the simulations. The above model for variable global saturation temperature was implemented as a user-defined function (UDF) in FLUENT. At the end of each time step, the total vapor volume

was determined by numerical integration over the computational domain, and a new saturation temperature was computed from Eq. (3-22b) and applied during the subsequent time step.

3.3 Model Geometry and Computational Mesh

To validate the CFD model, the three-dimensional geometry of the TPCT was built according to the experimental configuration in [3.3], as shown in Fig 3.1. In the experiments the TPCT wall was instrumented with a total of eight thermocouples, whose detailed positions are listed in Table 3.3. The TPCT design dimensions are listed in Table 3.4. Both the TPCT interior (fluid region) and the pipe wall (solid region) were included in the computational domain. The domain external boundary coincided with the outer cylindrical wall surface, and the material in the domain included both the saturated water and the solid copper of the TPCT pipe.

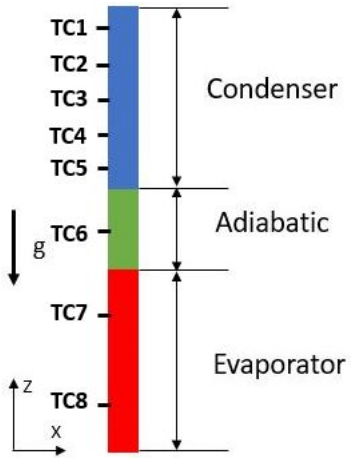

Figure 3.1. Schematic overview of the TPCT.

Table 3.3. Thermocouple positions from [3.3].

TC number	Position along z-axis (mm)
TC1	480
TC2	440
TC3	400
TC4	360
TC5	320
TC6	250
TC7	150
TC8	50

Table 3.4. Design summary of the TPCT from [3.3].

Wall material (mm)	Copper
Outer diameter	22
Wall thickness	0.9
Total length	500
Evaporator length	200
Adiabatic length	100
Condenser length	200

Hexahedral topology grids were generated using Pointwise (v17.0). At the inner wall surface, the first grid cell size was 0.01 mm in the radial direction and the growth ratio was 1.1. An O-type grid was specified from the inner wall up to a point located at one-half of the inner pipe radius, with a total of 32 cells around the circumference of the pipe. From that point an unstructured hexahedral mesh was used to resolve the central portion of the TPCT interior, as shown in Fig. 3.2. A total of 499 uniform cells were distributed in the axial direction. Starting from the inner cylinder surface (water/copper interface) a layer of ten cells of thickness 0.09 mm was extruded outward in the radial direction to resolve the solid pipe region. The total number of cells contained in the TPCT mesh was 846,304, which is comparable to other 3D TPCT simulations listed in Table 3.1. An overall view of the meshed geometry is shown in Fig. 3.2.

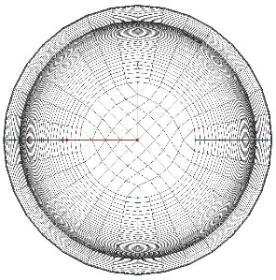

Figure 3.2 (a). Illustration of computational grid, including fluid and solid domains, axial view.

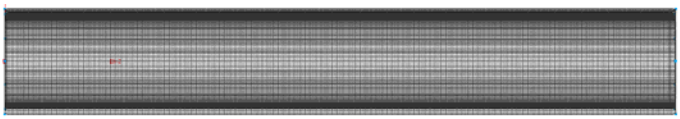

Figure 3.2 (b). Illustration of the outer surface grid, including fluid and solid domains, radial view.

3.4 Simulation Conditions

In the current study, the working fluid was water and the properties are listed in Table 3.5. According to the experiments conducted in Ref. [3.3], the vapor temperature can vary from 327.45 K to 345.75K while the liquid temperature can vary from 301.45 K to 327.45K. Because the temperature range is relatively small, all properties are assumed to be temperature independent except for the vapor density. The vapor density is defined using the incompressible idea gas law [3.22], in which the density of the vapor phase depends on the local temperature and the operating pressure, where the operating pressure is equal to the saturation pressure corresponding to the initial saturation temperature. Vapor density variation due to temperature was included in the simulation since free convection may influence the overall vapor flow field within the TPCT.

Table 3.5. Properties of the working fluid.

Property (unit)	**Value**
ρ_l (kg/m^3)	986.01
μ_l (kg/ms)	5.096×10^{-4}
k_l (W/mK)	0.6485
$c_{p,l}$ (J/kgK)	4181
μ_v (kg/ms)	1.075×10^{-5}
k_v (W/mK)	0.0207
$c_{p,v}$ (J/kgK)	1956
L (J/kg)	2371567

The boundary and initial conditions used in the CFD simulation are listed in Table 3.6. All boundary and initial conditions were set to correspond as closely as possible to the experimental study [3.3]. A no-slip boundary condition was applied on the inner wall of the TPCT. A constant and spatially uniform heat flux boundary condition was applied to the outer radial wall of the evaporator section. When the saturation temperature of the system was set to be a constant value, a constant heat flux boundary condition was also applied to the outer wall of the condenser, which differs from CFD simulations in Refs. [3.3] and [3.11]. The magnitude of the heat flux was selected to match the overall heat transfer rate reported in the experimental study. Use of the convective heat transfer boundary with a fixed saturation temperature for the working fluid effectively imposes both heat transfer rate and surface temperature of the condenser section, thus overconstraining the operation of the system. A detailed discussion of this phenomenon is included in the discussion of results below.

When the saturation temperature of the working fluid was a variable instead of a fixed value as in previous CFD simulations [3.3], [3.11], two types of boundary conditions for the condenser were employed. One type was equal and opposite uniform heat flux as the evaporator applied to the outer wall of the condenser, identical to the simulations with constant saturation temperature. The other was a convective heat transfer boundary condition as described in the CFD

simulation in Refs [3.3], [3.11]. For cases in which the saturation temperature of the working fluid was allowed to vary, the convective heat transfer boundary condition can potentially be used to obtain accurate results, and this is investigated below. Adiabatic conditions were applied to the cylinder top and bottom, and to the adiabatic section of the outer radial wall.

The vapor phase of the working fluid was defined as the primary phase, and the liquid phase was defined as the secondary phase. The volume fraction of the vapor was therefore initialized to 0 in the liquid region and 1 in the vapor region. The initial temperature of the liquid and vapor regions was 326.45 K and 328.45 K, respectively. These temperatures were selected to ensure that the system would reach a stationary state relatively quickly based on the initial saturation temperature of 327.45 K. The initial saturation temperature corresponds to the temperature of the adiabatic section of the TPCT in the reference experimental study [3.3]. The initialization of phases is illustrated in the contours of density shown in Fig. 3.3.

Table 3.6. Operating conditions (heat input of 167.7 [W]).

Condition	Section	Value
Boundary Condition	Evaporator	Constant heat flux: $Q = 167.7$ [W] $A = 0.013823$ [m^2] $q" = 12131.95$ [W/m^2]
	Adiabatic	Zero heat flux: $q" = 0$ [W/m^2]
	Condenser	Constant heat flux: $Q = -167.7$ [W] $A = 0.013823$ [m^2] $q" = -12131.95$ [W/m^2]
		Convective heat transfer: $h = 707.6$ [W/ m^{2}K] $T_\infty = 301.45$ [K]
	Top and bottom	Zero heat flux: $q" = 0$ [W/m^2]
	Wall Adhesion	Contact angle: $\theta = 12.7°$
Initial Condition	Liquid	Volume Fraction: $\alpha_l = 1$ Temperature: $T_l = 326.45$ [K]
	Vapor	Volume Fraction: $\alpha_l = 0$ Temperature: $T_v = 328.45$ [K]
Filling ratio	50%	
Gauge pressure	-86084.7 [Pa]	
Initial saturation temperature	327.45 [K]	

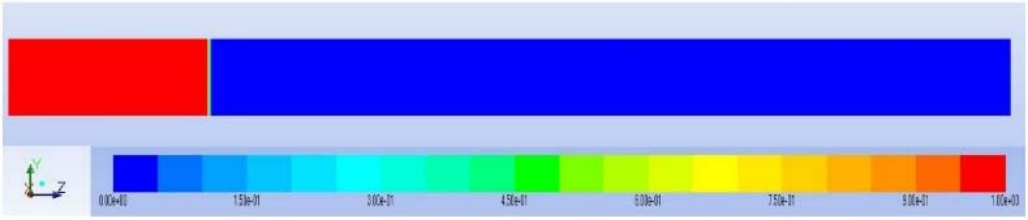

Figure 3.3. Initial density contour viewed from the y-z symmetry plane.

3.5 Solution Procedure

The computations were performed using Ansys FLUENT (v16.2) [3.22]. A transient simulation was carried out to model the dynamic behavior of the two-phase flow inside the TPCT.

A pressure-based scheme was employed with the SIMPLE algorithm for pressure-velocity coupling and momentum interpolation to mitigate pressure-velocity checkerboarding. Either the explicit Geo-reconstruct volume fraction discretization scheme or the implicit Compressive volume fraction discretization scheme was used to discretize the volume fraction equation. A first order upwind scheme was adopted to discretize the momentum and energy equations, as required, when using the Geo-Reconstruct scheme. Both first order and second order upwind schemes were adopted to discretize the momentum and energy equations for use with the Compressive scheme. PRESTO discretization was used for the pressure interpolation.

The initial time step size for all cases using the Geo-Reconstruct scheme was specified to be 0.00005 s. Because there is no imposed characteristic velocity for the system, it is difficult to estimate a priori the appropriate time step size based on the expected Courant-Friedrich-Lewy (CFL) number. However, the time step size of 0.00005 s was found to yield an average CFL of 0.13 during the initial stages of the simulation. Once a quasi-steady state was reached, as evidenced by an approximate balance of heat transfer rates into and out of the fluid portion of the domain, and by approximately equivalent rates of evaporation and condensation within the system, the time step size was reduced to 0.00001 s, in order to more effectively reproduce short time scale flow dynamics within the TPCT. The time step size for the cases using the Compressive scheme was specified to be 0.0001 s at both initial and steady state. During each time step, the simulation was assumed to be converged if the residuals for mass, velocity, energy were reduced by at least two orders of magnitude. The different solution method combinations used in this study are listed in Table 3.7 and Table 3.8. In addition to the cases listed in the two tables, simulations were also attempted using a constant saturation temperature and convective heat transfer boundary condition, following the approach used in [3.3-3.7,3.9-3.15]. It was found for those cases that a stationary

state could only be achieved for certain combinations of the mass transfer time relaxation parameters, and that for all cases the simulations were never able to reach a quasi-steady balance of heat transfer into and out of the system. The reason for this is discussed in more detail in the Results section.

Table 3.7. CFD solution methods for cases with constant saturation temperature.

	Mass transfer time relaxation parameters		**Volume Fraction Discretization Scheme**	**Momentum and Energy Discretization Scheme**
	r_{lv} (s^{-1})	r_{vl} (s^{-1})		
Constant heat flux boundary condition				
Case 1	0.1	0.1	Geo-Reconstruct	First order upwind
Case 2	0.1	973.356	Geo-Reconstruct	First order upwind
Case 3	1	9733.56	Geo-Reconstruct	First order upwind
Case 4	10	97335.6	Geo-Reconstruct	First order upwind
Case 5	1	9733.56	Compressive	Second order upwind

Table 3.8. CFD solution methods for cases with variable saturation temperature.

	Mass transfer time relaxation parameters		**Volume Fraction Discretization Scheme**	**Momentum and Energy Discretization Scheme**
	r_{lv} (s^{-1})	r_{vl} (s^{-1})		
Constant heat flux boundary condition				
Case 6	0.1	973.356	Compressive	Second order upwind
Case 7	1	9733.56	Geo-Reconstruct	First order upwind
Case 8			Compressive	First order upwind
Case 9			Compressive	Second order upwind
Case 10	10	97335.6	Geo-Reconstruct	First order upwind
Case 11			Compressive	First order upwind
Case 12			Compressive	Second order upwind
Convective heat transfer boundary condition				
Case 13	0.1	973.356	Geo-Reconstruct	First order upwind
Case 14			Compressive	First order upwind
Case 15			Compressive	Second order upwind
Case 16	1	9733.56	Geo-Reconstruct	First order upwind
Case 17			Compressive	First order upwind
Case 18			Compressive	Second order upwind
Case 19	10	97335.6	Geo-Reconstruct	First order upwind
Case 20			Compressive	First order upwind
Case 21			Compressive	Second order upwind

3.6 Results and Discussion

3.6.1 Predictions of TPCT Heat Transfer Performance

In the reference experimental study [3.3], temperature measurement positions in the TCPT pipe wall along the z-axis are located at 50 mm and 150 mm in the evaporator, 250 mm in the adiabatic section, and 320 mm, 360 mm, 400 mm, 440 mm, 480 mm in the condenser, as shown in Fig. 3.1. The temperature profiles reached an approximately steady state after 50 s of operation according to [3.3]. The difference between average wall temperature in the evaporator and condenser section is used along with the specified heat transfer rate to determine thermal resistance, which can be compared to experimentally determined values in order to validate the CFD simulation results.

Figure 3.4 shows a comparison between experimental data and the simulation results at steady state for the temperature profiles along the TPCT wall for the cases listed in Table 3.7 (except for Case 5), which use the Geo-Reconstruct volume discretization scheme with a constant saturation temperature. Note that the system was assumed to have reached a steady state when the net heat transfer rate into the fluid portion of the domain was found to oscillate around a value of zero, as shown in Figure 3.5, and the average evaporator and condenser temperatures were no longer changing with increasing simulation time. Examining Figure 3.4, the simulation results of Case 4 slightly overpredict the temperature in the condenser section relative to the experiments, while the other three cases underpredict the condenser temperature. In general, as the values of the mass transfer time relaxation parameters were increased, the temperature difference was reduced. This is due to the fact that, for larger values of the coefficients, a smaller difference between local and saturation temperature is needed to produce the same rate of mass transfer. Interestingly, the effect of changing the time relaxation parameters has much more impact on the condenser

temperature than the evaporator temperature. It is hypothesized that for evaporation the overall rate of mass transfer is controlled by the rate of heat conduction to the phase interface in the relatively low thermal conductivity vapor phase. For condensation, the rate of mass transfer is controlled by the phase change process itself, since heat conduction from the phase interface occurs relatively rapidly in the high thermal conductivity liquid.

In the experimental study, the condenser was cooled by a water jacket and the temperature of the cooling water was 301.45 K. Initially, simulations were attempted using a constant heat flux boundary condition for the evaporator and a convective boundary condition for the condenser, similar to [3.3-3.7,3.11-3.15]. The simulations never reached a stationary state, and the total (net) heat transfer rate for the system never balanced to zero in a time-averaged sense, consistently oscillating around a value that ranged from +60 W (+36% error) to -40 W (-24% error), depending on the values of the mass transfer time relaxation parameters. Also note that the cooling water temperature for the convective boundary condition (301.45 K) is in fact higher than the predicted surface temperature of the condenser for Case 1 (256.7 K) and Case 2 (274.9 K). That is one reason that attempted simulations with the convective heat transfer boundary condition for the condenser never reached steady state. When using a convective boundary condition for the condenser in combination with an imposed heat transfer rate in the evaporator, the average surface temperature of the condenser is effectively imposed by the choice of heat transfer coefficient and reference fluid temperature, T_∞. In that case, the average condenser wall temperature ($T_{c,a}$), the reference fluid temperature for condensation heat transfer (T_{sat}), and the heat transfer rate (Q) are all effectively fixed. As a result, the operation of the TPCT in the simulation is over-constrained when employing a convective heat transfer boundary condition for the condenser with a fixed saturation temperature. Under this situation, the total heat transfer rate of the TPCT never reaches a balanced

state. When a heat transfer rate is imposed, it is therefore more appropriate that the boundary condition for the both the evaporator and condenser be defined as constant heat flux to enforce that the net system heat transfer rate be zero.

For the present simulations, the saturation temperature is defined as 327.45 K, instead of the commonly used value of 373 K in some previous CFD simulations for the same TPCT design and operating conditions [3.3,3.11]. The saturation temperature used herein is the same as the temperature of the adiabatic section measured in the experiments by Fadhl [3.3], since the temperature of the adiabatic section is a good indicator of the working temperature of the TPCT. As can be seen from Figure 3.4, the temperature of the thermocouples located along the wall of TPCT are all less than 373 K, so that value is clearly not appropriate for the test case considered.

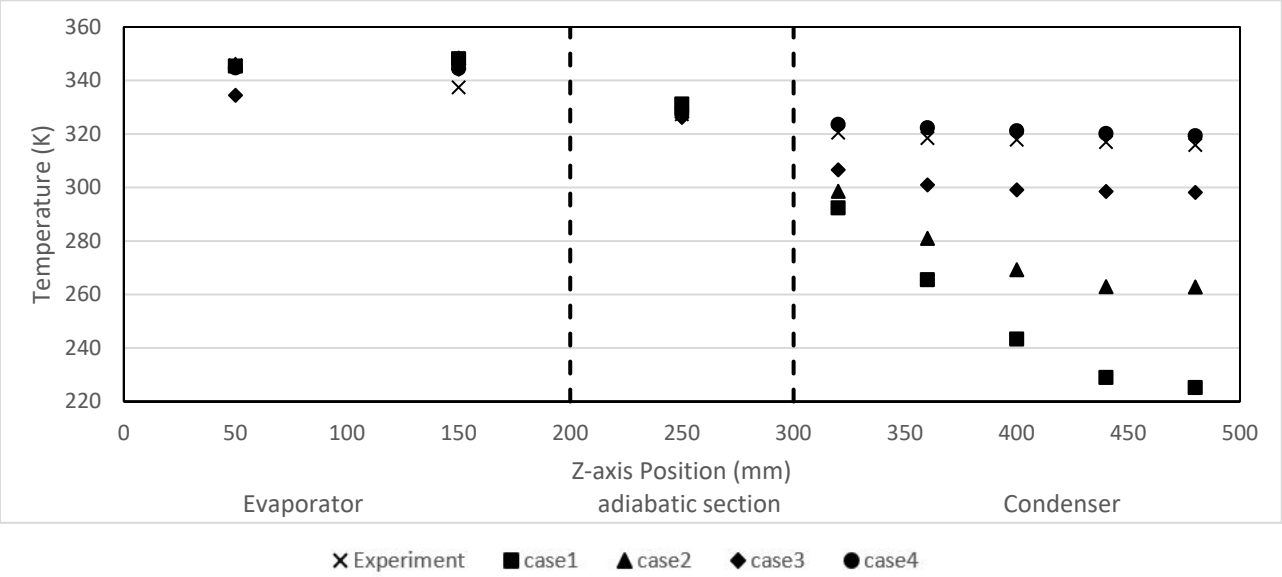

Figure 3.4. Comparison of the temperature profiles between the experimental data and simulation results using the Geo-Reconstruct volume discretization scheme with constant saturation temperature.

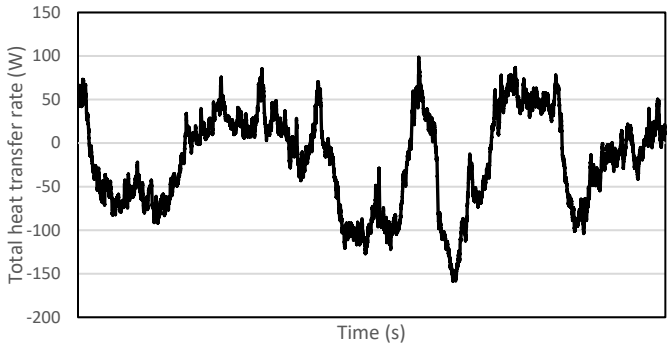

Figure 3.5. Net heat transfer rate through the inner wall of the heat pipe over a time interval of 2.5 seconds at steady state.

A system level figure of merit that can be used to determine simulation accuracy is thermal resistance, which is calculated as

$$R = \frac{T_{e,a} - T_{c,a}}{Q}. \tag{3-20}$$

where $T_{e,a}$ and $T_{c,a}$ are the average wall temperatures in the evaporator and condenser section, respectively, and Q is the heat transfer rate into the evaporator section [3.3]. Fadhl [3.3] also performed a CFD simulation on the heat transfer performance of the TPCT. In their study, a convective heat transfer boundary condition for the condenser was employed with the same mass transfer time relaxation parameters as in Case 1. A comparison of the thermal resistances of previous CFD simulations and the simulations with constant saturation temperature in this study is shown in Table 3.9. The thermal resistance from simulation results in [3.3] has a relative error of 111%. In the current study, Case 1 has the largest deviation from the thermal resistance measured in the experiment, and it should be noted that the simulation of Case 1 was never able to achieve steady state. When the Case 1 simulation was terminated, the relative error between the experimental data and simulation result was already 410% and continuing to increase. If the simulation were continued, the difference between the average surface temperature of the evaporator and condenser would have increased further, resulting in even higher overall thermal

resistance. Therefore, the Case 1 simulation was terminated as the relative error of the final result would have only been higher than the result shown. This result for case 1 underscores the recommendation of previous authors that the mass transfer time relaxation parameters should have relative values determined by the liquid-to-vapor phase density ratio [3.9-3.11,3.16].

Case 2, which has the same value for the evaporation parameter as case 1 (0.1), but uses a condensation parameter based on the density ratio, was able to reach a steady state and shows a smaller relative error of 203%, but predicted thermal resistance remained significantly higher than the experimental data. The best agreement was found for Case 4 which has a relative error of 6%. The thermal resistances in Table 3.9 indicate that predictions are improved when the phase change processes are modeled to occur more rapidly. In other words, as the mass transfer time relaxation parameters for the evaporation and condensation model are increased, the local temperature difference above (evaporation) and below (condensation) the saturation temperature required to drive the phase change process becomes smaller and more effectively models the real process. The results in Table 3.9 suggest that an optimum value for the evaporation time relaxation parameter lies between 1 and 10, since the thermal resistance for those two cases effectively bound the experimentally determined value.

Table 3.9. Thermal resistance for the experimental data set in [3.3] and the relative error of the simulation results when using a constant saturation temperature.

	Thermal Resistance (K/W)	**Relative Error (%)**
Experiment	0.141	
CFD result in [3]	0.297	+111
Case 1	0.720	+410
Case 2	0.428	+203
Case 3	0.231	+64
Case 4	0.133	-6
Case 5	0.260	+84

Overall, it can be seen from Table 3.9 that the accuracy of the simulation results (Case 3 and Case 4) was significantly improved by choosing a more appropriate saturation temperature for the system and using a constant heat flux boundary condition for the condenser, compared to previous CFD studies of the same configuration [3.3-3.11]. However, one key limitation of the Geo-Reconstruct volume fraction discretization is that the time step size must be maintained at a small value compared to other volume fraction discretization schemes to prevent divergence of the simulation. In order to further increase the time step size, the implicit Compressive volume discretization scheme using the same boundary condition for the condenser and saturation temperature as Cases 1-4 was investigated as a possible viable alternative to the Geo-Reconstruct scheme. Case 5, with the same set of mass transfer time relaxation parameters for evaporation and condensation as Case 3, never successfully reached steady state even after 85 s of physical simulation time. In addition, the liquid mass fraction continued steadily downward and the TPCT appeared be approaching dryout. Even for cases that reached a steady state, the final predicted volume fraction of both the vapor phase and the liquid phase still showed a large deviation from the initial volume fraction as can be seen from Table 3.10. From the table it is apparent that cases 3 and 4 were found to under- and over-predict, respectively, the total mass of the system. This once again suggests that the optimum value of the evaporation time relaxation parameter likely lies between 1 and 10, consistent with the thermal resistance results in Table 3.9.

More importantly, in general the total mass of the working fluid inside the TPCTs is not conserved even for cases which have reached a steady state. In short, the simulations violate conservation of mass. One reason for this is believed to be the constant value of saturation temperature used for these cases, which does not allow the system to respond appropriately to changes in total liquid and vapor mass fraction, which in real physical systems would yield a

change in system pressure and therefore a change in saturation, effectively providing a feedback loop to ensure that phase changes are occurring in such a way that mass conservation is satisfied. It is this observation that motivated the development of the variable T_{sat} model described above, and results obtained using that model are discussed in the following section.

Table 3.10. Final predicted volume fraction and total mass for cases with constant saturation temperature.

	Liquid volume fraction	**Vapor volume fraction**	**Total mass (kg)**
Initial values	0.2	0.8	0.02916
Case 2	0.112	0.888	0.01632
Case 3	0.118	0.882	0.01716
Case 4	0.326	0.674	0.04665

The variable saturation temperature formulation proposed above was incorporated into the simulations for all cases using either a constant heat flux or a convective heat transfer boundary condition for the condenser. Simulated cases are summarized in Table 3.8. Resulting predicted values for thermal resistance are listed in Table 3.11. Of particular interest are the results for cases 7 and 10, which correspond to cases 3 and 4, respectively, except for the use of the variable versus constant saturation temperature. Cases 3 and 4 showed the best agreement with experimental data for the constant T_{sat} cases and effectively bound an optimum case in terms of both thermal resistance and mass conservation. Table 3.11 shows that similar behavior is observed for cases 7 and 10. The relative error for both cases was relatively small, with values -9.22% and +13.48%, respectively. The results suggest that the use of a variable saturation temperature does not degrade the simulation results and may in fact yield an improvement in terms of heat transfer performance for a given set of time relaxation parameter values.

Table 3.11. Thermal resistance for the experimental data set in [3.3] and the relative error of the simulation results when using a variable saturation temperature.

	Thermal Resistance (K/W)	**Relative Error (%)**
Experiment	0.141	
CFD result in [3]	0.297	+111.14
Constant heat flux boundary condition		
Case 6	0.213	+51.06
Case 7	0.128	-9.22
Case 8	0.205	+45.39
Case 9	0.233	+65.25
Case 10	0.160	+13.48
Case 11	0.301	+113.48
Case 12	0.250	+77.31
Convective heat transfer boundary condition		
Case 13	0.195	+38.3
Case 14	0.240	+70.2
Case 15	0.157	+11.35
Case 16	0.129	-8.51
Case 17	0.200	+41.80
Case 18*	0.249	+71.63
Case 19	0.177	+25.53
Case 20	0.298	+111.35
Case 21*	0.247	+75.17
* Simulations were numerically unstable and diverged before reaching a stationary state		

As discussed above, for the cases with a constant heat flux boundary condition in the condenser, case 5 with a fixed saturation temperature never successfully reached steady state even after 85 s of physical time. The use of a variable saturation temperature successfully mitigated this problem, as a steady state condition was reached for the corresponding case 8. Furthermore, cases 7 and 10 reached a steady state much earlier than cases 3 and 4, reducing convergence time by approximately 80%. It is hypothesized that the variable T_{sat} model allows the system to more rapidly respond to unbalanced heat and mass transfer rates. For example, if the rate of condensation is greater than the rate of evaporation, the saturation temperature adjusts to force the system

towards equal mass transfer rates for each. In turn, this reduces the overall physical simulation time required to reach statistical convergence.

In the previous section, it was determined that a constant heat flux boundary condition should be applied for both the evaporator and the condenser when using a constant saturation temperature in order to ensure that net heat transfer rates balance and the simulation is able to reach a stationary state. In general, it is proposed here that the following four variables characterize the heat transfer process in the TPCT: Q, $T_{e,a}$, $T_{c,a}$, and T_{sat}, which denote the heat transfer rate through the heat pipe, the average evaporator temperature, the average condenser temperature, and the saturation temperature. For any simulation, only two of these should be constrained. Use of the variable saturation temperature model relaxes the constraint on saturation temperature, which allowed the simulations with a convective condenser boundary condition to converge to steady state. For these cases, the net heat transfer rate for the system was still not balanced, but for all cases the imbalance was less than 10W (±6% error). Comparing all similar cases using convection versus constant heat flux boundary conditions (cases 7-12 versus cases 16-21), it was found that the mean square error was 65.1% versus 65.4%, indicating that the difference in accuracy between the two boundary conditions was negligible. Nevertheless, it is still recommended that simulations with imposed heat transfer rate should use constant heat flux boundary conditions for the evaporator and condenser to ensure that the overall heat transfer to the system is balanced.

Table 3.12 shows the final saturation temperature obtained for each of the simulations. Note that cases 18 and 21, which used second order discretization for the momentum and energy equations, were found to have stability issues, so the saturation temperatures shown for these two cases are the values before the simulations began to diverge. At stationary state, the saturation temperature oscillated about the value shown, which was taken to be the time-averaged final value

(except for cases 18 and 21). For all cases, the final saturation temperature varied less than 19 K from the initial value of 327.45 K. The two cases with the smallest change from the initial saturation temperature were cases 7 (+1.44 K) and 16 (+2.13 K), both of which used the Geo-Reconstruct volume fraction discretization and an evaporation mass transfer time relaxation parameter of 1, and differed only in terms of the condenser boundary condition. These were also the two most accurate cases in terms of thermal resistance, as seen in Table 3.11, with both having an error magnitude of less than 10%.

Table 3.12. Final predicted saturation temperature.

	Saturation Temperature (K)
Initial	327.45
Constant heat flux boundary condition	
Case 6	334.36
Case 7	328.89
Case 8	332.93
Case 9	344.45
Case 10	320.30
Case 11	338.65
Case 12	337.85
Convective heat transfer boundary condition	
Case 13	333.11
Case 14	346.30
Case 15	333.21
Case 16	329.58
Case 17	334.10
Case 18	346.35
Case 19	320.6
Case 20	323.9
Case 21	332

Table 3.13 is a summary of the final predicted volume fraction of the liquid and vapor phases and the total mass of the system for all cases that reached a steady state with the variable saturation temperature model. From Eq. (3-22b), it is apparent that the deviation in total liquid and vapor volume fraction, and hence total mass, from initial values is proportional to the difference

between final and initial saturation temperature. Therefore, it can be seen that case 14 has the largest deviation, while cases 7 and 16 have the smallest. For the latter two cases, the mass imbalance is -1.3% and -0.5%, respectively. The corresponding case with constant saturation temperature is case 3, which had a mass imbalance of -41%. When using the variable model for saturation temperature, the maximum imbalance for all cases is approximately 15%. Compared to the final predicted volume fraction of and total mass of the system using a fixed saturation temperature listed in Table 3.10, the relative errors between the final predicted values and the initial values are significantly reduced. This result indicates that the variable saturation temperature can help to produce more physically realistic results than using a fixed system saturation temperature.

Table 3.13. Final predicted volume fraction and total mass for simulation cases using variable saturation temperature.

	Liquid volume fraction	**Vapor volume fraction**	**Total mass (kg)**
Initial values	0.2	0.8	0.02916
Case 6	0.189	0.811	0.02744
Case 7	0.198	0.802	0.02879
Case 8	0.190	0.810	0.02754
Case 10	0.212	0.788	0.03096
Case 13	0.191	0.809	0.02783
Case 14	0.170	0.830	0.02471
Case 15	0.191	0.809	0.02782
Case 16	0.197	0.803	0.02901
Case 17	0.190	0.810	0.02760
Case 19	0.212	0.788	0.03096
Case 20	0.205	0.795	0.03003

The performance of the three different numerical scheme combinations was compared to highlight differences in accuracy and computational efficiency. The three combinations considered were: Geo-Reconstruct for volume fraction with first order upwind for momentum and energy; Compressive for volume fraction with first order upwind for momentum and energy; and Compressive for volume fraction with second order upwind for momentum and energy. As noted

above, two of the cases with Compressive and second-order upwind were found to be unstable and diverged prior to obtaining a stationary state. It is possible that the simulations could have been made more stable by reducing the time step size, but varying time step sizes to find optimum values was beyond the scope of this work. The mean squared error (MSE) in thermal resistance for all cases using the Geo-Reconstruct/1st-order combination was 22.2%, with a minimum and maximum error magnitude of 8.51% and 38.3%, respectively. For the Compressive/1st-order combination the corresponding error values were 82.5%, 41.8%, and 113.5%, and for the Compressive/2nd-order combination they were 65.0%, 11.35%, and 77.31%. The results are consistent with expectations, since the Geo-Reconstruct scheme most accurately captures a sharp interface between the liquid and vapor phases. It is also consistent with prior CFD studies. Of the 15 references listed in Table 3.1, 3.12 used the Geo-Reconstruct scheme for volume fraction discretization. The results here confirm that, in terms of accuracy, the Geo-Reconstruct is superior to the Compressive scheme.

Comparison of computational efficiency between different scheme combinations was less straightforward. There was negligible difference in memory usage between the different discretization scheme combinations. The total computational cost in terms of CPU time was determined by three separate aspects: CPU time per iteration, time step size, and physical simulation time required to reach a stationary state. As discussed above in the description of the methodology, all simulations used the same number of iterations to converge the simulation at each time step. The time step size for all three scheme combinations was determined via numerical experimentation, in which a representative case was started with a very small time step size that was systematically increased by an order of magnitude after several seconds of physical simulation time until the simulation diverged. The largest time step size for which the simulation was stable was then used for all simulations with the same scheme. Based on this method, it was found that

the Compressive scheme could yield stable results with a time step size double that for the Geo-Reconstruct scheme. (However, as discussed above, the time step size thus determined for the Compressive scheme was later found to be not stable for cases 18 and 21).

The difference in CPU time per iteration (as determined by wall clock time to run the same number of time steps on the same computing hardware) was negligible between the Geo-Reconstruct and the Compressive schemes. The physical simulation time to reach a stationary state varied significantly, however. For cases using the smallest value for the evaporation and condensation mass transfer coefficients (0.1 and 973.356, respectively), simulations using the Geo-Reconstruct scheme required approximately half of the time required by the Compressive scheme to reach convergence. As a consequence, the total computational cost using the Compressive scheme was approximately 25% of that using the Geo-Reconstruct scheme. For larger values of the mass transfer coefficients (1 and 10 for evaporation, 9733.56 and 97335.6 for condensation), the Geo-Reconstruct scheme required less than half the physical simulation time to converge as the Compressive scheme. As a result, the total computational cost between the two schemes was, surprisingly, nearly equal. It is also interesting to note that more accurate results were obtained with the Compressive scheme when using smaller values for the mass transfer coefficients, and more accurate results were obtained with the Geo-Reconstruct scheme using larger values. The reasons for this are not readily apparent. It is hypothesized that for the Compressive scheme, because the phase interface is distributed over several cells, the volume in which interphase mass transfer is occurring is larger than for the Geo-Reconstruct scheme, which restricts the interface within a single cell. As a consequence, higher mass transfer coefficients are needed for the Geo-Reconstruct scheme to achieve a physically appropriate rate of evaporation and condensation.

3.6.2 Comparison of Field Results Using Different Solution Methods

In order to gain insight into the physical processes occurring in the TPCT and to compare the effects of the different solution methods, contours of the vapor phase volume fraction, temperature, and velocity are presented. Figures 3.6 and 3.7 show comparisons of the volume fraction of the vapor phase on the inner wall surface and on the symmetry plane, respectively, for the TPCT at steady state with a constant heat flux boundary condition for the condenser. For case 5, which did not achieve a steady state, results are shown after an operating time of approximately 85 s. Case 3 and case 7, using the Geo-Reconstruct scheme, show both liquid droplets and liquid films formed at the condenser wall. For cases 5 and 8, using the Compressive scheme, the condenser and part of the adiabatic section are mostly covered with liquid film. It is apparent for cases 3 and 7 with the Geo-Reconstruct method that the interface between the liquid phase and the vapor phase is well preserved and is contained within a single computational cell. For case 5 and case 8 using the Compressive method, the interface between the liquid phase and the vapor phase is somewhat dispersed though still clearly identifiable. In Figure 3.7, it is apparent that the volume of the liquid phase in case 5 is much lower than for the other cases. As discussed above, this case evolved steadily toward dryout before being terminated, and in the figure the size of the liquid pool in the evaporator has clearly reduced significantly from its initial state. Case 8, shown in Figure 3.7 (d), is identical to case 5 except for the fact that it used the variable model for saturation temperature. For this case the liquid pool was not substantially reduced, and the total liquid fraction remained close to the initial value as shown in Table 3.13.

Figure 3.8 shows a comparison of temperature profiles at the inner surface of the TPCT at steady state (case 5 is shown after an operating time of approximately 85 s). For cases 3 and 7, the average surface temperature of the evaporator is approximately 330K. In the condenser section,

the average surface temperature for case 3 is approximately 300 K and the average surface temperature for case 7 is approximately 320 K. For cases 5 and case 8, the average surface temperature of the condenser is approximately 315 K, and in the evaporator section the average surface temperature for case 5 is approximately 370 K and for case 8 is approximately 360 K. In general, all four cases show the expected trend of the temperature profile. Qualitative differences are apparent between the cases with the Geo-Reconstruct versus Compressive scheme. For the former, which shows dropwise and filmwise condensation on the condenser wall in Figure 3.6, the distribution of temperature is more uniform on the condenser wall than for the Compressive scheme, which shows only filmwise condensation in Figure 3.6. Likewise, the two schemes show different locations of maximum temperature in the evaporator section. Both differ qualitatively from the experimental data in Figure 3.4, which shows monotonic variation through the length of the TPCT. Quantitative results, however, indicate that the Geo-Reconstruct results predict the overall performance of the system, including the average evaporator and condenser wall temperatures, with a reasonable level of "engineering" accuracy.

Figure 3.9 shows the velocity distribution in the symmetry plane for case 3 and case 8. It can be seen clearly in both cases that the vapor flow in the center of the TPCT tends to move downward and a circulation of the working fluid inside the TPCT has developed. Furthermore, the liquid and vapor velocities are comparable between the two cases, indicating that the solution of the momentum equation is at least qualitatively independent of the VOF solution. Overall, the flow inside the TCPT shows the correct gross motion and velocity magnitudes are reasonable. Unfortunately, more detailed validation of field results is not possible since no data was available from the reference experimental study. Nevertheless, the results in Figures 3.6-3.9 highlight the fundamentally three-dimensional nature of the flow in the thermosyphon, suggesting that a full 3D

simulation methodology, such as that used here, is better suited to resolve the complex flow physics than a 2D axisymmetric approach.

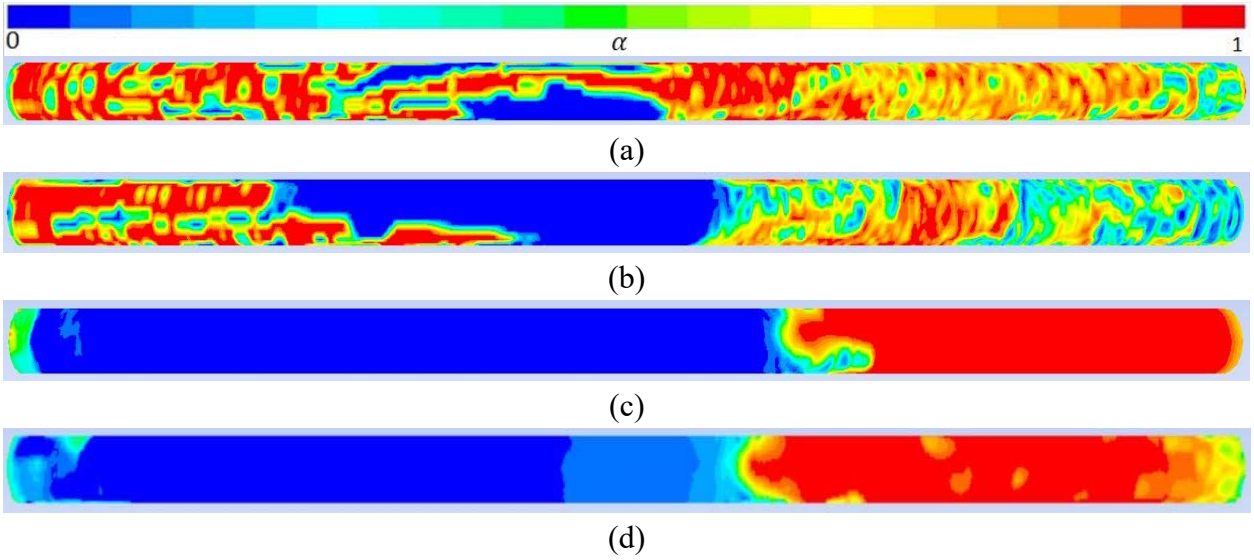

Figure 3.6. Comparison of the vapor phase volume fraction contours on the inner wall surface at steady state: (a) case 3; (b) case 7; (c) case 5; (d) case 8.

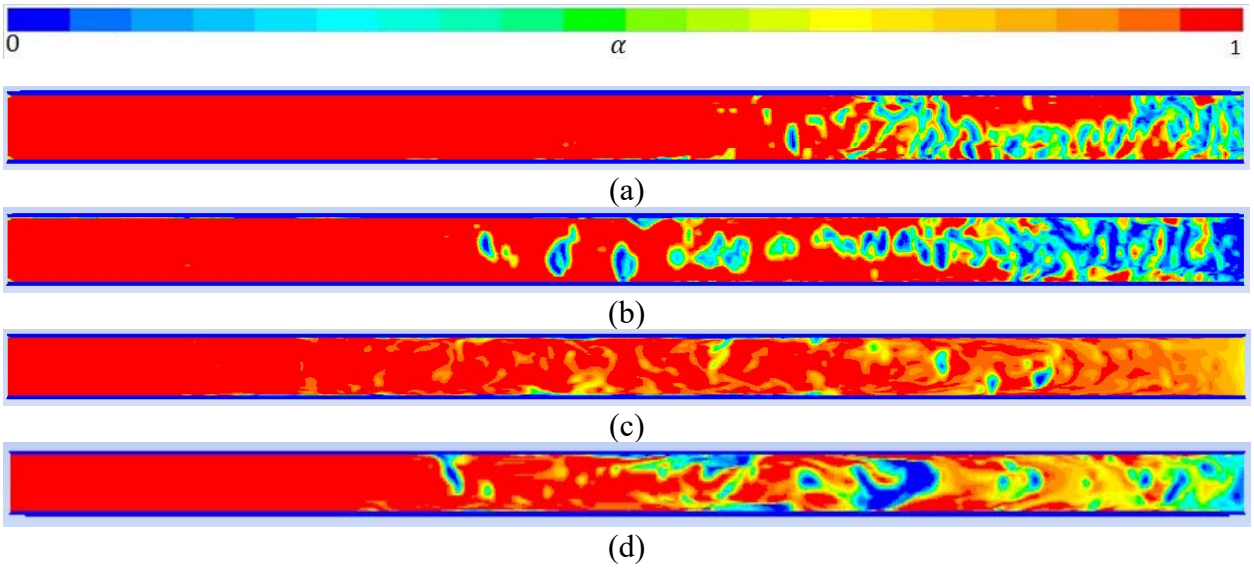

Figure 3.7. Comparison of the vapor phase volume fraction contours in the symmetry plane at steady state: (a) case 3; (b) case 7; (c) case 5; (d) case 8.

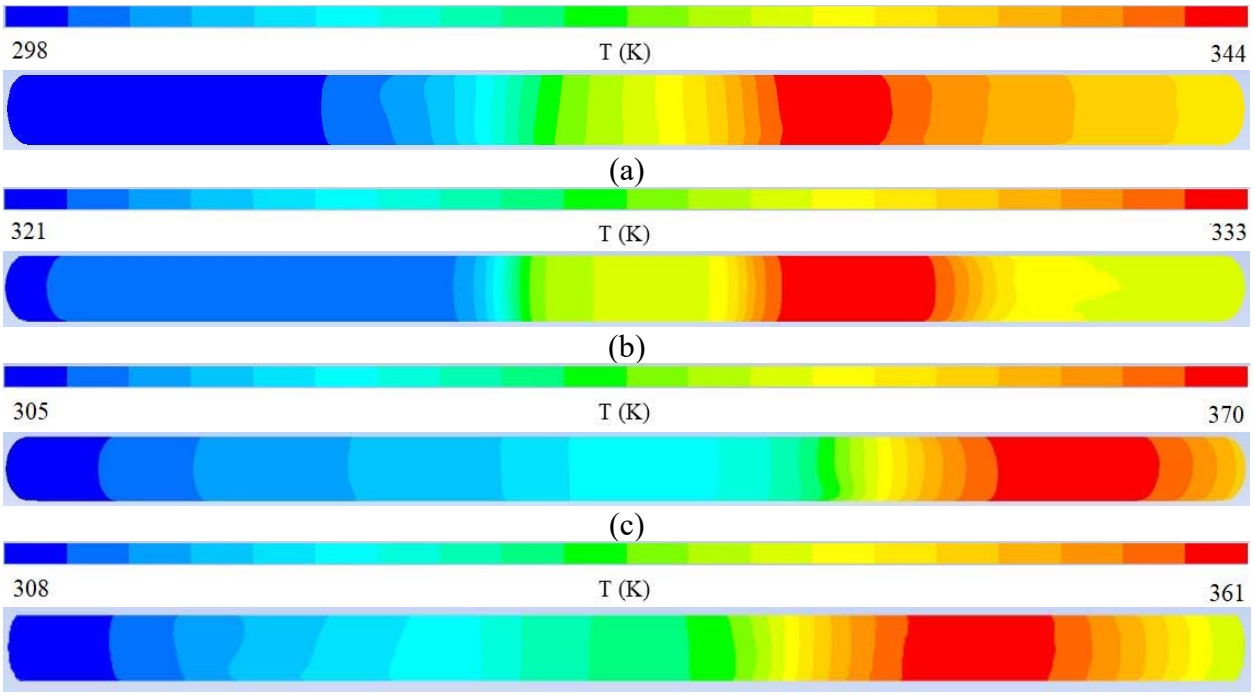

Figure 3.8. Comparison of the temperature contours on the inner wall surface at steady state: (a) case 3; (b) case 7; (c) case 5; (d) case 8.

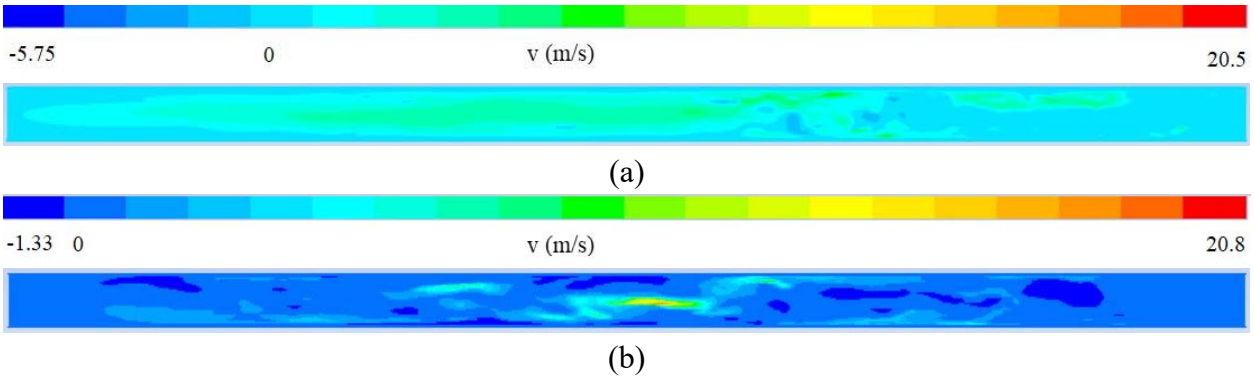

Figure 3.9. Velocity profile in the symmetry plane at steady state: (a) case 3; (b) case 8.

3.7 Conclusions

This paper investigates the effect of different solution methods on accuracy and computational expense of 3D CFD simulations of a two-phase closed thermosyphon (TPCT). The

overall objective of this study was to investigate different combinations of numerical scheme, boundary conditions, models, and model coefficients, in order to determine an accurate and efficient simulation methodology using the well-known volume-of-fluid (VOF) approach within general-purpose finite-volume flow solver. Simulations were performed for a TPCT test case that matches a previously published experimental study, and which has been used as a validation test case for previously documented CFD studies.

An initial set of simulations was run using a general methodology previously adopted by other studies in the open literature, including constant saturation temperature, constant heat flux boundary condition for the evaporator section, convection boundary condition for the condenser, the Geo-Reconstruct numerical scheme for discretization of the volume fraction equation, and a ratio of interphase mass transfer time relaxation parameters (i.e. mass transfer coefficients) based on the liquid-to-vapor density ratio for use in the Lee evaporation/condensation model [3.18]. Based on results from the initial tests, a second set of test cases were run with identical set up, except for the use of a constant heat flux boundary condition in the condenser section. For both sets of cases, several different values of the mass transfer coefficients were tested to determine their effect on the simulation results.

Based on results from the simulations with constant saturation temperature, a new model for variable global saturation temperature was developed and implemented into the CFD solver. In the second part of the study, simulations using the variable saturation temperature model were run for test cases with constant heat flux and convection boundary conditions in the condenser (for all cases a constant heat flux condition was used in the evaporator), the Geo-Reconstruct and Compressive scheme for the volume fraction equation, first- and second-order discretization of the momentum and energy equations, and several different values of the mass transfer coefficients.

Simulations were run until a stationary state was reached in which wall temperatures in the evaporator, condenser, and adiabatic sections were no longer changing with increasing simulation time. Results from the 21 total simulations were interrogated in detail. The primary system level figure of merit for validation was the thermal resistance of the TPCT. Other relevant global characteristics were the time-averaged total mass and net heat transfer rate, which quantified how well the simulation results satisfied mass and energy conservation, respectively, over the entire system. Results including distribution of volume fraction, temperature, and velocity were also presented.

The simulation results allow for several significant conclusions to be drawn regarding TPCT operation and modeling. First, the results support the assertion of previous researchers that the condensation and evaporation time relaxation parameters in the Lee model [3.18] should be selected such that their ratio is equal to the density ratio between the liquid and vapor phases. Using the density ratio to guide selection of the mass transfer time relaxation parameters provides a physical relationship for the balance in mass transfer between the vapor and liquid phases within the TPCT. A simulation using equal values of the parameters did not achieve a steady state condition, and at the time it was terminated, the relative error in terms of thermal resistance was over 400%. Simply adjusting the condensation parameter based on density ratio allowed the simulation to achieve a steady state, and a much smaller error of 200%.

For simulations in which the saturation temperature is fixed to a constant value, the use of a constant heat flux boundary condition for the evaporator and a convection boundary condition for the condenser is not appropriate. The reason is that the convection boundary condition effectively fixes the condenser wall temperature based on the heat transfer coefficient and reference temperature, since the heat transfer rate is nominally determined by the evaporator

boundary condition. As a result, the temperatures in the system are overconstrained. For the constant saturation temperature cases at steady state, the net heat transfer to the system showed an imbalance of up to 60% of the applied evaporator heat transfer rate. For cases with a prescribed saturation temperature, it is more appropriate to use constant heat flux boundary conditions for both the evaporator and the condenser to ensure that the net heat transfer rate is in balance. It should be noted that of the 15 previous studies summarized on Table 3.1, only two use this boundary condition combination. It should also be noted that most studies do not report the net heat transfer rate for their simulations.

For the general VOF solution approach used here and in most previous studies, saturation temperature and vapor density are assumed to be independent of the system pressure. As a consequence, mass is not conserved in the simulations. In the present study, for simulations using a constant saturation temperature, differences between final and initial system mass were found to vary between 40% and 60%. It should be noted that most studies in the open literature do not report the final versus initial system mass or verify that mass is conserved in their simulations.

The proposed model for variable saturation temperature was found to successfully mitigate both mass and energy imbalance. For all cases, the maximum difference between final and initial system mass when using the model was less than 15%. For the two cases in which the thermal resistance was predicted with the highest accuracy, the imbalance was less than 3%. The result verifies that the variable saturation temperature model performs as intended, providing a feedback mechanism to adjust the saturation temperature appropriately when evaporation rate becomes too high relative to condensation, or vice versa. The result also suggests that it might be possible to determine an optimum saturation temperature for a given simulation based on minimizing mass imbalance, although such an approach is reserved for future study. The variable saturation

temperature model also allowed physically realistic results to be obtained using a convection boundary condition for the condenser, since the strict constraint on saturation temperature was relaxed. The maximum energy imbalance over all simulations was found to be less than 6%. Finally, a variable saturation temperature resulted in a substantially shorter time required for the simulations to reach a stationary state, presumably since the simulation can quickly adjust the relative rates of condensation and evaporation such that they become equal much more quickly than when using a constant saturation temperature.

Simulations using the Geo-Reconstruct scheme were found to be more accurate than those using the Compressive scheme, based on mean squared error and on the most accurate result for each. This is likely due to the fact that the Geo-Reconstruct scheme is capable of resolving the sharp interface between the liquid and vapor phases. The Compressive scheme was found to be stable using a time step size larger than the Geo-Reconstruct scheme, however for most cases the physical simulation time required to reach convergence was shorter using the Geo-Reconstruct scheme. As a result, the two schemes were comparable in terms of total computational cost.

Based on the above, it is recommended that TPCT simulations use the proposed or a similar model for variable saturation temperature in combination with the Geo-Reconstruct scheme, a full 3D computational domain that includes both fluid and solid regions of the thermosyphon geometry, mass transfer time relaxation parameters based on liquid-to-vapor density ratio, and constant heat flux boundary conditions for both evaporator and condenser. Choice of the value of the evaporation (or condensation) mass transfer coefficient should be determined via numerical experimentation and optimization, with mass balance used as a metric to determine the optimum value if experimental results are not available for validation.

Future research will investigate application of this methodology to additional test cases including oscillating heat pipes. It may also be possible to develop a method for dynamic computation of the evaporation and condensation coefficients and saturation temperature such that the simulation automatically adopts values that result in global conservation of both mass and energy.

CHAPTER IV: CFD SIMULATION OF AN OSCILLATING HEAT PIPE

Oscillating heat pipes (OHPs) have been implemented for numerous applications including electronic cooling, energy storage systems, and thermoelectric power generators. Because of their utility and demand, several numerical and experimental studies have been carried out to analyze and predict the heat transfer performance of OHPs. This paper investigates the performance of a commercially available computational fluid dynamics (CFD) solver (Ansys FLUENT) to predict the complex flow behavior of OHPs using a compressive discretization scheme with the volume of fluid (VOF) model. Numerical simulations of an OHP vertical channel sections are performed. Validation of appropriate modeling and numerical parameters is achieved by performing simulations of heat and mass transfer performance for a two-phase closed thermosyphon (TPCT) from previous work, since the heat transfer mechanism and operating principles of the TPCT and OHP are similar and experimental data is more readily available for the TPCT. Initial results show that using an appropriate value for the evaporation and condensation mass transfer coefficients along with the compressive discretization scheme allows computationally efficient simulation and yields results that show good agreement with available experimental data. Results further show that the 3D CFD simulation methods implemented in this study successfully predict the phase change process and vital flow behavior inside the OHP.

4.1 Introduction

A heat pipe is a passive heat transfer device driven by the temperature gradient between the evaporator and condenser without external pumping. An oscillating heat pipe (OHP), or pulsating heat pipe (PHP), is a type of heat pipe that was developed by Akachi [4.1] and is generally made from a long capillary tube bent into several turns with no wick structure. It consists

of three parts: an evaporator, an adiabatic section, and a condenser. Heating in the evaporator leads to the evaporation of the liquid, leading to phase change and vapor generation. The size and quantity of the gas bubbles increases leading to higher vapor pressure. This increase in vapor pressure drives the motion of the fluid towards the condenser, where the fluid is cooled. The cyclic phase change between liquid and vapor state, accompanying density-driven fluid motion, and separation of the evaporator and condenser sections result in an oscillating or pulsating motion of the working fluid inside the OHP. There are three major types of OHPs: closed loop; closed loop with additional check valves; and open loop. Most researchers believe the optimum heat transfer performance in closed loop oscillating heat pipes (CLOHP) is higher than in the other two OHP types due to the circulation of the working fluid within the pipe being a constant volume, and for this reason the CLOHP is the most common OHP type [4.2].

One advantage of the OHP is the simple design, as they do not have any wicking structure. Also, OHPs are compact in size compared to conventional heat pipes, making them a more flexible option to accommodate different system configurations. Hence the OHP has been used in a broad range of applications, including electronic cooling, solar collectors, fuel cell cooling, and micro electronic devices [4.2-4.4]. The wide application of OHPs has led to increasing interest among researchers, and various experimental and numerical studies have investigated their performance. Among the numerical studies, computational fluid dynamics (CFD) models have been developed by several researchers to simulate the complex heat and mass transfer processes inside OHPs using the commercially available software package Ansys FLUENT. One challenge for CFD research is to determine an accurate and efficient method to simulate two-phase flow, as occurs during evaporation and condensation inside OHP.

The most common approach for early researchers was to use the volume of fluid (VOF) model to simulate the interface of the two phases inside the OHPs [4.5-4.21]. Among all these studies, the Geo-Reconstruct scheme is the most popular discretization scheme for the volume fraction equation, since this scheme can capture the sharp interface between the liquid and vapor phases of the working fluid [4.5-4.7]. For example, Liu et al. [4.5] performed a 3D simulation to predict liquid-vapor two-phase flow during the heat and mass transfer process inside the CLOHPs using Ansys FLUENT. In their CFD study, the second order upwind scheme was employed to discretize the momentum and energy equations. Wang et al. [4.6] performed a 2D CFD study using the second order upwind scheme on a single CLOHP loop with different length ratios of the evaporator to the condenser to investigate start-up characteristics and thermal performance. Mohammad et al. [4.7] successfully reproduced the heat and mass transfer process inside an OHP with a 2D CFD model using Ansys FLUENT.

To increase the time step size for transient simulations in order to more quickly reach steady state conditions, thereby reducing computational cost, a dispersed interface has been employed by some researchers. For example, a 2D CFD simulation was carried out by Gupta et al. [4.8] on a CLOHP in bottom heated mode to study its thermal performance using Ansys FLUENT using the first-order upwind scheme to discretize the energy, momentum, and volume fraction equations. Zhao et al. [4.9] performed a 2D CFD simulation using Ansys FLUENT of a single turn OHP at different vacuum degrees during the startup process to investigate vapor flow patterns and the distribution and fluctuation of the pressure. In this study second-order upwind schemes were employed for the discretization for the kinetic energy, momentum, specific dissipation rate, and energy equations with an implicit solver formulation.

Some other methods have been used to simulate the flow inside OHPs using Ansys FLUENT. For example, some researchers use the mixture model to simulate the flow behavior and heat transfer mechanism of OHPs [4.22-4.23]. Zhang et al. [4.23] performed a 2D CFD simulation on a miniature OHP in bottom heating mode to study the flow behavior and heat transfer performance. Two sets of simulations were performed, employing either the VOF model or mixture model. In the VOF model, the dispersed interface was selected. In both simulations the QUICK scheme was chosen to discretize the momentum equations and volume fraction equations, and the first-order upwind scheme was applied as the discretization scheme for the energy equation. Reddy et al. [4.24] used transient RANS simulations to investigate the thermal performance of a CLOHP with different filling ratios. In their CFD study, the second-order upwind scheme was selected to discretize the momentum equations, and the first-order upwind discretization scheme was used for turbulent kinetic energy and specific dissipation rate. Some other researchers [4.25-4.26] have performed CFD simulations on CLOHP systems but without specifying the details of the methods used in their studies. It should be noted that the majority of prior CFD simulations of OHP systems are two dimensional. Full 3D simulations are less common. Of those studies discussed above, only Refs. [4.5], [4.12], [4.15], [4.19], [4.21], and [4.24] are 3D simulations.

This paper is an extension of a previous CFD study on a two-phase closed thermosyphon (TPCT) system [4.27], since the operating principles of the TPCT and OHP are very similar. In this paper, the 3D CFD simulations of OHPs were performed using a new method, compressive discretization scheme implemented as a user-defined function (UDF) within the VOF model, that has been proved to be effective in the CFD simulations of the TPCT. The method proposed is designed to allow for an increase in the time step size commonly used in the Geo-Reconstruct

method. Similar to the previous TPCT study [4.27], a methodology is implemented to allow variation of the global saturation temperature during the simulation, in response to the net inter-phase mass transfer. Two cases were examined in this work, each having the same heat load but using different values for the coefficient that limits the volume change of the vapor phase and the saturation temperature. The boundary conditions for both the evaporator and the condenser of the OHP were applied constant heat flux. The evaporation and condensation mass transfer time relaxation parameters were selected based on results from the previous TPCT study [4.27]. All simulations are run using full three-dimensional computational domains. Simulation results were validated against the experimental data available in Ref [4.23].

4.2 Methods

Simulations were carried out using the commercial software Ansys FLUENT (v16.2) and grids were constructed using available Ansys meshing tools. In this study, the volume-of-fluid (VOF) model was used to simulate the two-phase flow and capture the interface between liquid and vapor phases. The Lee [4.28] model was employed to calculate the rate of interphase mass transfer in the vicinity of the phase interface during the evaporation and condensation processes. The continuum surface force (CSF) [4.29] model was employed to simulate the surface tension of the liquid-vapor interface. The new variable saturation temperature model was implemented as a user-defined function (UDF) in Ansys FLUENT. In order to more thoroughly investigate the effect of this coefficient on the simulation results, two cases were run to completion, i.e. to a stationary state in terms of thermal resistance. Cases 1 and 2 used values of $C = 5.5 \times 10^6$ and 2.75×10^6, respectively. It was found that a value of $C = 5.5 \times 10^6$ was effective in maintaining stability, while limiting the change in vapor fraction to 10% of the initial vapor volume with the variation of saturation temperature of less than +/- 25 K during the course of the simulations. A value of

$C = 2.75 \times 10^6$ limited the change in vapor fraction to 20% of the initial vapor volume, and limited the variation of saturation temperature to less than +/- 25 K. Further details of the simulation methods are summarized in Section 3.2.

4.3 Model Geometry and Computational Mesh

In order to validate the CFD model, the three-dimensional geometry of the OHP was built to match the experimental configuration in [4.23]. The material and dimensions of the OHP are listed in Table 4.1.

Table 4.1. Design summary of the OHP.

Wall material	**Copper**
Outer diameter (mm)	1.6
Inner diameter (mm)	0.5
Total length L (mm)	100
Evaporator length (mm)	20
Condenser length (mm)	20
Number of turns	4

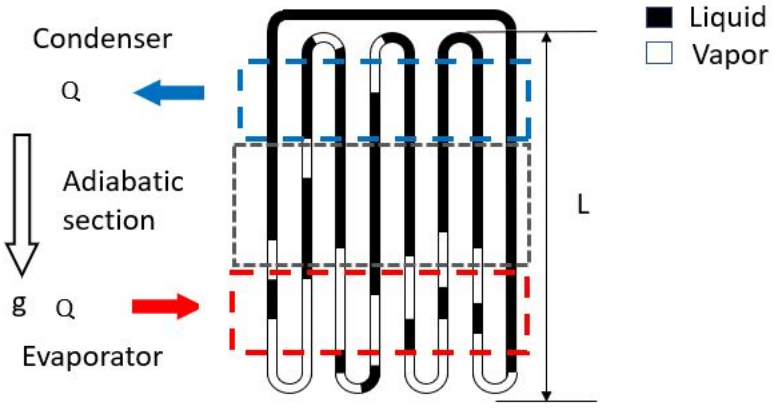

Figure 4.1. Schematic overview of the OHP design.

A multi-block structured grid was generated using Ansys for the oscillating heat pipe geometry used in this study. An O-type grid with a rectangular core was used to control the growth rate of

cells inside the pipe and to reduce skewness. The circumference of the pipe was discretized with 40 cells. In the radial direction, a total of 42 cells were used to discretize the pipe in the radial direction. The axial direction was discretized uniformly using a total of 500 cells in the evaporator, adiabatic, and condenser section together of the straight pipe while the curved adiabatic section contained 100 cells in the axial direction. A total of 3.8 million cells were distributed throughout the OHP domain. A mesh resolution study was beyond the scope of this effort. It should be noted that only Ref [4.5] of the three-dimensional studies documented above [4.5,4.12,4.15,4.19,4.21,4.25] performed mesh resolution studies, and that the total number of cells in those cases ranged from 4,407-566,244. The mesh resolution used in the current study is therefore comparable to or greater than that used in previous, similar efforts.

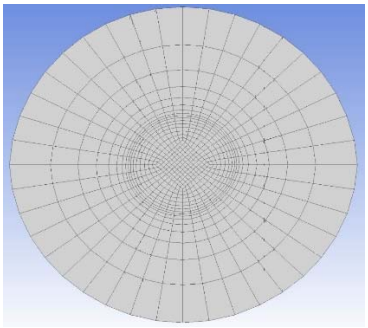

Figure 4.2(a). Illustration of computational grid of the straight pipeline, including fluid and solid domains, axial view.

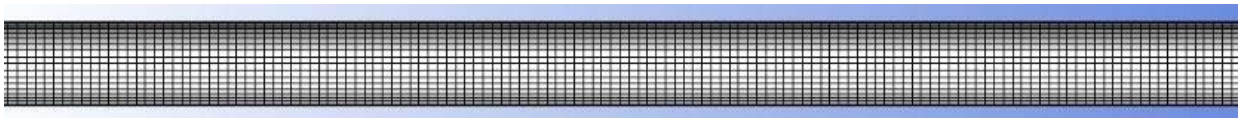

Figure 4.2(b). Illustration of the outer surface grid of the straight pipeline, including fluid and solid domains, radial view.

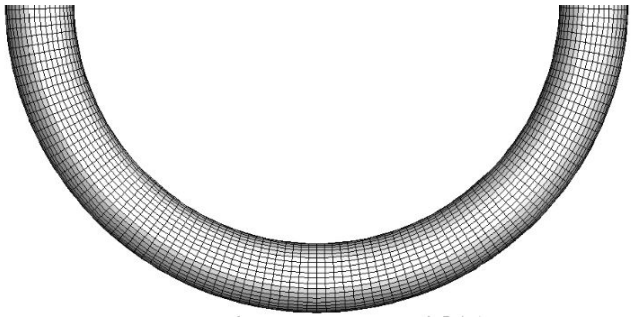

Figure 4.2(c). Illustration of the outer surface grid of the curved pipeline, including fluid and solid domains, radial view.

4.4 Simulation Conditions

In the present study, the working fluid is water and the properties of the liquid and vapor phases are listed in Table 4.2. All properties are assumed to be temperature independent except for the density of the vapor, the value of which shown in the table corresponds to the density at the initial saturation temperature and pressure. The instantaneous local vapor density was obtained from the incompressible ideal gas law in FLUENT, for which the pressure was assumed equal to the initial saturation pressure.

According to the experimental data for the validation test case, the average surface temperature of the evaporator was 370.2 K and the average surface temperature of the condenser was 301.5 K. The initial saturation temperature was selected to be the average of these two values, 335.85 K. Note that since the pressure of the vapor phase in the experiment was not supplied, the initial saturation temperature cannot be specified exactly. Based on results from the prior study on TPCT simulation [4.27], the average of the evaporator and condenser temperatures is assumed to be a reasonable estimate.

The initial filling ratio for the OHP was 50%, therefore the vapor phase volume fraction was initialized to be zero below the vertical midplane, and one above the vertical midplane. Note that the filling ratio is defined here as the ratio of the liquid volume to the total volume of the OHP.

For the initial temperature condition, all portions of the domain above the condenser and in the condenser section were set to be 301.5 K, and all portions of the domain below the evaporator and in the evaporator section were set to be 370.2 K. For the adiabatic section, the temperature was specified as a linear function of the position, $T = (260.337 - 1510Y)$ K. Contours of initial vapor phase volume fraction are shown on the inner wall of the OHP in Fig. 4.3. The initial temperature contour at the inner wall of the OHP is illustrated in Fig. 4.4.

Table 4.2. Properties of the working fluid, water.

Property (unit)	**Value**
ρ_l (kg/m^3)	981.826
μ_l (kg/ms)	4.4739×10^{-4}
k_l (W/mK)	0.657
$c_{p,l}$ (J/kgK)	4186
ρ_v (kg/m^3)	0.1457
μ_v (kg/ms)	1.0524×10^{-5}
k_v (W/mK)	0.022
$c_{p,v}$ (J/kgK)	1921.7
L (J/kg)	2351960

The boundary conditions and initial conditions used in the CFD simulation are listed in Table 4.3, and were selected to correspond as closely as possible to the experimental study [4.23]. A no-slip boundary condition is applied on the inner wall of the OHP. A constant heat flux boundary condition is applied to the evaporator. An equal and opposite constant heat flux condition is applied to the outer wall of the condenser. It was found in [4.27] that this choice is the most physically appropriate of the three commonly used idealized thermal boundary conditions (isothermal, constant heat flux, and convection), since it ensures that the net rate of heat transfer to the OHP is zero, while not artificially enforcing a wall temperature in the condenser section. Adiabatic conditions are applied to the top sections above the condenser, bottom sections below the evaporator, and adiabatic sections.

Table 4.3. Operating conditions (heat input of 24 [W]).

Condition	**Section**	**Value**
Boundary Condition	Evaporator	Constant heat flux: $Q = 24$ [W] $A = 0.000808$ [m^2] $q" = 29703$ [W/m^2]
	Adiabatic	Zero heat flux: $q" = 0$ [W/m^2]
	Condenser	Constant heat flux: $Q = -24$ [W] $A = 0.000808$ [m^2] $q" = -29703$ [W/m^2]
	Curved Sections	Zero heat flux: $q" = 0$ [W/m^2]
	Wall Adhesion	Contact angle: $\theta = 15.6°$
Initial Condition	Liquid	Volume Fraction: $\alpha_l = 1$
	Vapor	Volume Fraction: $\alpha_l = 0$
Filling ratio	50%	
Gauge pressure	-78700 [Pa]	
Initial saturation temperature	335.85 [K]	

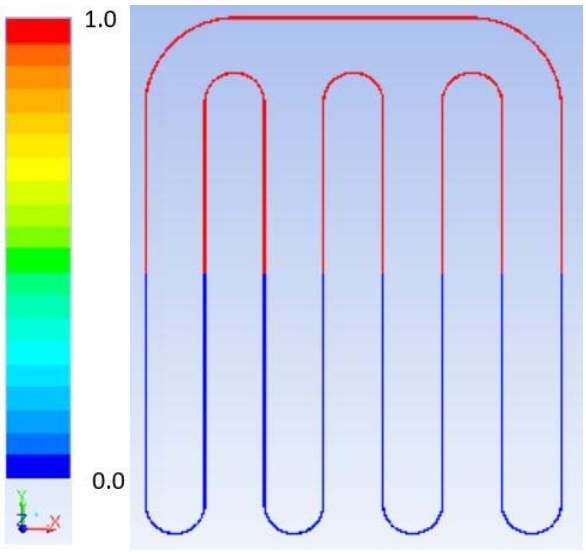

Figure 4.3. Initial vapor phase contour at the inner wall of the OHP.

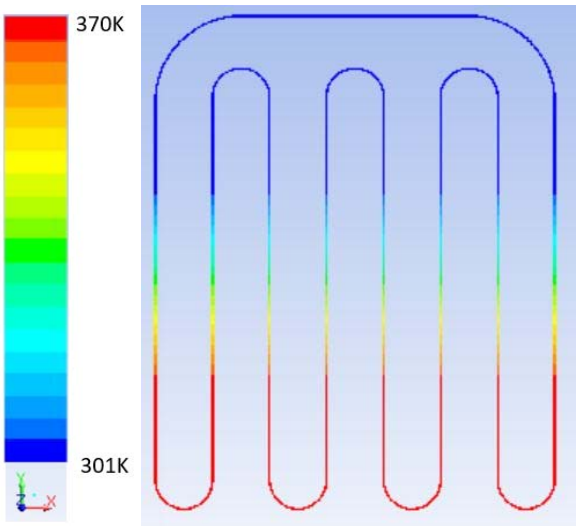

Figure 4.4. Initial temperature contour at the inner wall of the OHP.

4.5 Solution Procedure

The CFD simulations were performed using FLUENT (v16.2) on computing hardware at the University of Oklahoma Supercomputing Center for Education & Research (OSCER). A transient simulation was carried out to model the dynamic behavior of the two-phase flow inside the OHP. The algorithm employed for pressure-velocity coupling was SIMPLE with momentum-weighted interpolation to mitigate pressure-velocity decoupling. The implicit Compressive scheme was used to discretize the volume fraction equation. A first-order upwind scheme was adopted to discretize the momentum and energy equations. The PRESTO discretization for the pressure interpolation was selected.

The initial time step size for both cases was specified to be 0.0001s. Because there is no imposed characteristic velocity for the system, it is difficult to estimate *a priori* the appropriate time step size based on the expected Courant-Friedrich-Lewy (CFL) number for the system. Once the simulation achieved a limiting steady state condition, it was found that the maximum CFL number was 2227. One key advantage of the implicit formulation is that it permits the use of a higher CFL number than an explicit scheme, with the trade-off that the simulation may not resolve

some of the small-time-scale features of the flowfield. The extent to which the implicit formulation and selected time step size are appropriate will be partly determined based on validation comparison to the experimental data. In fact, one primary objective of this study is to determine if the implicit Compressive scheme with relatively large time step size can simulate the performance characteristics of an OHP with reasonable engineering accuracy and computational expense.

4.6 Results

The most useful quantitative metric to evaluate heat transfer performance for the OHP is the effective overall thermal resistance, which can be calculated as

$$R = \frac{T_{e,a} - T_{c,a}}{Q}. \tag{4-20}$$

where $T_{e,a}$ and $T_{c,a}$ are the average temperatures in the evaporator and condenser section, respectively, and Q is the heat transfer rate into the evaporator section [4.23]. In the present study, the value of the thermal resistance showed an oscillatory time-dependent behavior as illustrated in Figure 4.5. The period of each cycle was approximately 5 s of physical time. In order to compare simulation results to reference data, the thermal resistance was averaged over several cycles to determine a stationary (time-averaged) value. The resulting time-averaged thermal resistance is compared to experimental data in Table 4.5. Recall that in the present study Case 1 and Case 2 refer to two different values that were chosen for the global model for saturation temperature defined in Eq. (3-22b). All other simulation details, including the boundary conditions for the evaporator and the condenser, the mass transfer time relaxation parameters, the initial saturation temperature of the system, are the exactly the same between the two cases.

Lin et al. [4.23] performed CFD simulations to determine OHP heat transfer performance using both the VOF model and mixture model separately, and their calculated thermal resistance values are included for comparison in the results summary (Table 4.4). In the Lin et al. [4.23]

study, applying the mixture model resulted in a much smaller relative error (116.08%) than using only the VOF model (819.23%). It is worth pointing out that the dispersed interface was employed when they were performing the CFD simulation on the OHP using the VOF model. In the current study, the predicted thermal resistance for both cases is significantly lower than either of the cases in Ref [4.23]. It is apparent that both cases underpredict the thermal resistance that was measured experimentally [4.23]. The higher coefficient ($C = 5.5 \times 10^6$) in Case 1 results in a smaller relative error (26.40%) for the thermal resistance predicted in comparison to the lower coefficient ($C = 2.75 \times 10^6$) in Case 2 (43.71%). As discussed above, the value of the coefficient represents a trade-off between accuracy and numerical stability. The higher value of the coefficient in Case 1 enforces a stricter bound on the overall mass transfer between phases, and therefore serves to keep the filling ratio on the simulation closer to the value of 50% in the experiment. The results suggest that in practice, use of the variable saturation temperature model can potentially be optimized by determining the maximum value of C that can be used while still maintaining numerical stability in the simulation.

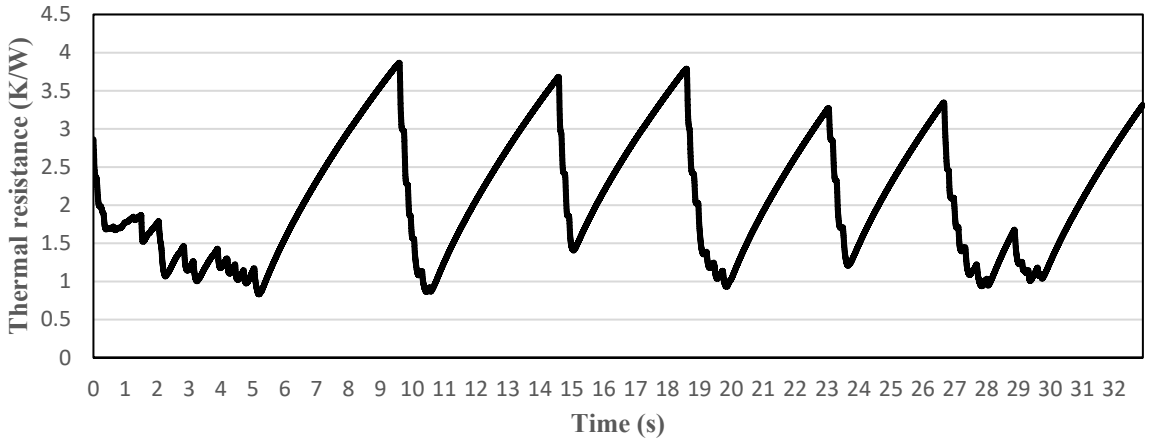

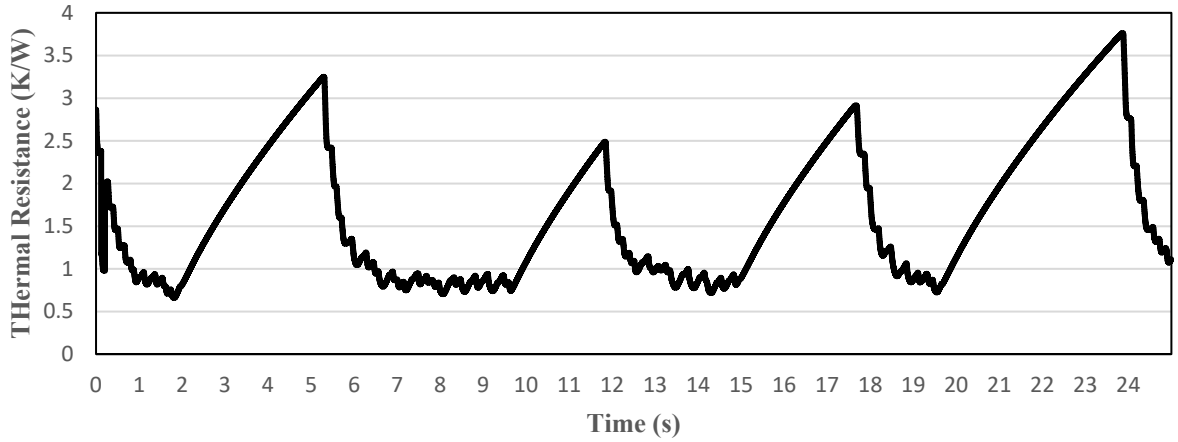

Figure 4.5. Thermal resistance as a function of time: (a) $\boldsymbol{C = 5.5 \times 10^6}$; (b) $\boldsymbol{C = 2.75 \times 10^6}$.

Table 4.4. Summary of thermal resistances (heat input of 24 [W]).

	Thermal Resistance(K/W)	**Relative Error (%)**
Experiment [23]	2.86	
Case 1	2.105	-26.40
Case 2	1.610	-43.71
CFD result using VOF model alone in [23]	26.29	+819.23
CFD result using mixture model alone in [23]	6.18	+116.08

Results are shown by Case 1, which had the lower error for thermal resistance based on the comparison to experimental data. Figure 4.6 is a comparison of the volume fraction of the vapor phase at the inner wall at a at different physical simulation times, beginning at 26 s and using a time interval of 1.5 s. The interface between the liquid phase and the vapor phase is somewhat dispersed though still clearly identifiable with the Compressive volume discretization scheme. In Figure 4.6 (a) to (d), the oscillatory motion of the vapor phase can be clearly observed. It can be seen from Figure 4.3 that the liquid was distributed at the bottom half of the OHP initially. After the heat was supplied to the evaporator, the evaporation process started and generated bubbles in the evaporator. As the vapor pressure kept increasing, the liquid was pushed upward. Hence the oscillatory behavior of working fluid inside the OHP started.

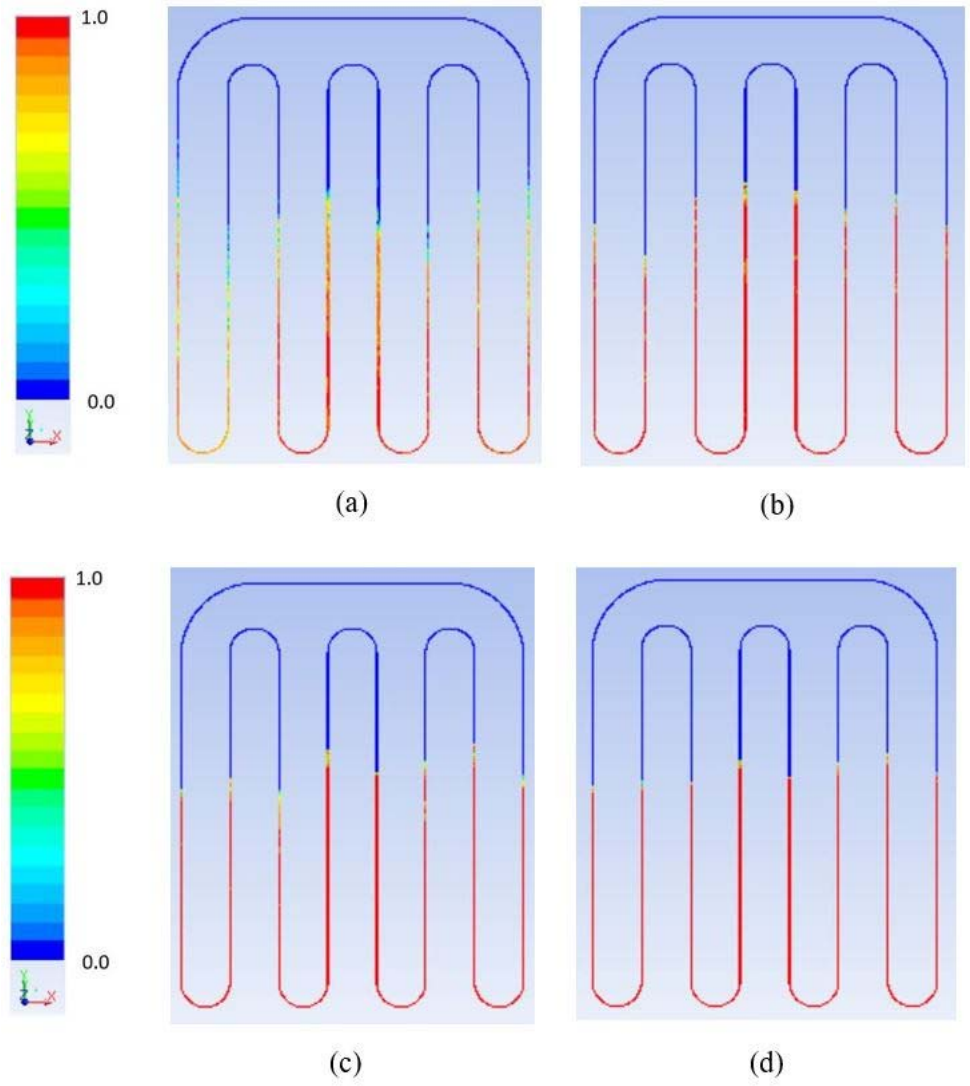

Figure 4.6. Comparison of the vapor phase volume fraction contours (starting at around 26 s) at the inner wall using a time interval of 1.5s for an oscillating cycle of the OHP.

4.7 Conclusions

This paper extends upon a prior study of CFD simulation methods for two-phase flow in heat pipe applications [4.27] and applies them to the simulation of an oscillating heat pipe (OHP). Specifically, the methodology consists of applying the volume-of-fluid (VOF) model with a Compressive discretization scheme for the volume-fraction equation, in combination with a proposed model for variable saturation temperature based on the total liquid-to-vapor mass transfer

in the system. Simulations were run using a fully three-dimensional, unsteady approach. Use of the implicit Compressive scheme allowed for significantly larger time-step size than possible for stable solution with explicit schemes that have been used in previous simulations documented in the literature. The use of a variable saturation temperature model facilitated convergence to a stationary state for which the filling ratio and saturation temperature remained close to the experimental test case. Comparison of results to experimental data show that the method used yields results that are significantly more accurate than previously documented CFD results for the same test case. The new method adopted here allows for successful prediction of the oscillating flow behavior of water as the working fluid inside the OHP and for a significant increase in the simulation time step size in comparison to the more commonly used Geo-Reconstruct method. Future work will focus on additional simulations with an alternative convective heat transfer boundary condition for the condenser, higher evaporation and condensation mass transfer time relaxation parameters, different geometries and varying heat loads.

CHAPTER V: CONCLUSIONS

In this study, both the analytical model and computation model were employed to investigate the concept of ferrofluid charged OHP as an energy harvester. The analytical model developed characterizes the key design parameter of the ferrofluid energy harvesting process and relates the induced EMF from the solenoids to the external magnetic field strength, the ferrofluid pumping frequency, and operating temperatures. The CFD simulations successfully predict the two-phase complex flow behavior and the heat transfer performance of the TPCT and the OHP. The research effort presented in this dissertation demonstrates viable modeling methods to describe and predict operation and energy generation from passive, cyclic thermofluidic induction processes. This work contributes to the understanding of combined heat transfer, fluid mechanics, and energy harvesting inherent to thermofluidic induction, and impacts the predictive modeling and understanding of oscillating fluid in capillary structures with expended magnetic field, thermal/magnetic coupling effects in ferrofluid, effect of generated magnetic fields on heat transfer mechanisms, relative fluid motion and magnetic field on nanoparticle suspension and alignment. The study also provides guidelines for efficient ferro-nanofluids for combined heat transfer enhancement and energy harvesting/conversion service. This method can be utilized for analysis and design of combined thermal management and on-site power generation systems and will potentially have broad application in electronics cooling, waste heat recovery, renewable energy generation, autonomous energy system design and other next-generation technologies.

5.1 Analytical Model

The analytical model developed in the present work predicts induced EMF due to a pulsating ferrofluid passing through solenoid-equipped tubing. The basis of the model is the assumption that the pulsating fluid is analogous to a series of cylindrical slugs moving through the

induction coil. Starting from the expression for induced EMF from a single point dipole, an expression for EMF versus relative position between the slug centroid and solenoid centroid is obtained. The expression can then be integrated to determine the RMS value of EMF for a given set of conditions.

The model inputs include properties of the ferrofluid, magnetic field, solenoid, and fluid flow. As a consequence, it potentially can be tailored to a wide range of EMF generation systems. Experimental data from an energy harvesting process that employed pulsating ferrofluid motion driven by a peristaltic pump was used to validate the model. Uncertainty in the model inputs was included by obtaining minimum and maximum prediction of induced EMF for each test case. The two extrema were found in the present case to differ by approximately two orders of magnitude.

The analytical model generated was able successfully predict induced EMF from a solenoid for pulsating ferrofluids. The trends with respect to both magnetic flux density and pumping frequency were correctly reproduced, and the experimental EMF values were between the minimum and maximum for all cases, with the exception of the two operating conditions for which the experimental values were nominally zero. Overall, the results suggest that the modeling approach adopted here is valid for these magnetic fluid-induced energy harvesting configurations, although further work is needed to fully validate and optimize the modeling methodology for general ferrofluid energy scavenging applications.

5.2 CFD Simulation on TPCT

This work investigates the effect of different solution methods on accuracy and computational expense of 3D CFD simulations of a two-phase closed thermosyphon (TPCT). The overall objective of this study was to investigate different combinations of numerical scheme, boundary conditions, models, and model coefficients, in order to determine an accurate and

efficient simulation methodology using the well-known volume-of-fluid (VOF) approach within general-purpose finite-volume flow solver. Simulations were performed for a TPCT test case that matches a previously published experimental study, and which has been used as a validation test case for previously documented CFD studies.

An initial set of simulations was run using a general methodology previously adopted by other studies in the open literature, including constant saturation temperature, constant heat flux boundary condition for the evaporator section, convection boundary condition for the condenser, the Geo-Reconstruct numerical scheme for discretization of the volume fraction equation, and a ratio of interphase mass transfer time relaxation parameters (i.e. mass transfer coefficients) based on the liquid-to-vapor density ratio for use in the Lee evaporation/condensation model [3.18]. Based on results from the initial tests, a second set of test cases were run with identical set up, except for the use of a constant heat flux boundary condition in the condenser section. For both sets of cases, several different values of the mass transfer coefficients were tested to determine their effect on the simulation results.

Based on results from the simulations with constant saturation temperature, a new model for variable global saturation temperature was developed and implemented into the CFD solver. In the second part of the study, simulations using the variable saturation temperature model were run for test cases with constant heat flux and convection boundary conditions in the condenser (for all cases a constant heat flux condition was used in the evaporator), the Geo-Reconstruct and Compressive scheme for the volume fraction equation, first- and second-order discretization of the momentum and energy equations, and several different values of the mass transfer coefficients.

Simulations were run until a stationary state was reached in which wall temperatures in the evaporator, condenser, and adiabatic sections were no longer changing with increasing simulation

time. Results from the 21 total simulations were interrogated in detail. The primary system level figure of merit for validation was the thermal resistance of the TPCT. Other relevant global characteristics were the time-averaged total mass and net heat transfer rate, which quantified how well the simulation results satisfied mass and energy conservation, respectively, over the entire system. Results including distribution of volume fraction, temperature, and velocity were also presented.

The simulation results allow for several significant conclusions to be drawn regarding TPCT operation and modeling. First, the results support the assertion of previous researchers that the condensation and evaporation time relaxation parameters in the Lee model [3.18] should be selected such that their ratio is equal to the density ratio between the liquid and vapor phases. Using the density ratio to guide selection of the mass transfer time relaxation parameters provides a physical relationship for the balance in mass transfer between the vapor and liquid phases within the TPCT. A simulation using equal values of the parameters did not achieve a steady state condition, and at the time it was terminated, the relative error in terms of thermal resistance was over 400%. Simply adjusting the condensation parameter based on density ratio allowed the simulation to achieve a steady state, and a much smaller error of 200%.

For simulations in which the saturation temperature is fixed to a constant value, the use of a constant heat flux boundary condition for the evaporator and a convection boundary condition for the condenser is not appropriate. The reason is that the convection boundary condition effectively fixes the condenser wall temperature based on the heat transfer coefficient and reference temperature, since the heat transfer rate is nominally determined by the evaporator boundary condition. As a result, the temperatures in the system are overconstrained. For the constant saturation temperature cases at steady state, the net heat transfer to the system showed an

imbalance of up to 60% of the applied evaporator heat transfer rate. For cases with a prescribed saturation temperature, it is more appropriate to use constant heat flux boundary conditions for both the evaporator and the condenser to ensure that the net heat transfer rate is in balance. It should be noted that of the 15 previous studies summarized on Table 1, only two use this boundary condition combination. It should also be noted that most studies do not report the net heat transfer rate for their simulations.

For the general VOF solution approach used here and in most previous studies, saturation temperature and vapor density are assumed to be independent of the system pressure. As a consequence, mass is not conserved in the simulations. In the present study, for simulations using a constant saturation temperature, differences between final and initial system mass were found to vary between 40% and 60%. It should be noted that most studies in the open literature do not report the final versus initial system mass or verify that mass is conserved in their simulations.

The proposed model for variable saturation temperature was found to successfully mitigate both mass and energy imbalance. For all cases, the maximum difference between final and initial system mass when using the model was less than 15%. For the two cases in which the thermal resistance was predicted with the highest accuracy, the imbalance was less than 3%. The result verifies that the variable saturation temperature model performs as intended, providing a feedback mechanism to adjust the saturation temperature appropriately when evaporation rate becomes too high relative to condensation, or vice versa. The result also suggests that it might be possible to determine an optimum saturation temperature for a given simulation based on minimizing mass imbalance, although such an approach is reserved for future study. The variable saturation temperature model also allowed physically realistic results to be obtained using a convection boundary condition for the condenser, since the strict constraint on saturation temperature was

relaxed. The maximum energy imbalance over all simulations was found to be less than 6%. Finally, a variable saturation temperature resulted in a substantially shorter time required for the simulations to reach a stationary state, presumably since the simulation can quickly adjust the relative rates of condensation and evaporation such that they become equal much more quickly than when using a constant saturation temperature.

Simulations using the Geo-Reconstruct scheme were found to be more accurate than those using the Compressive scheme, based on mean squared error and on the most accurate result for each. This is likely due to the fact that the Geo-Reconstruct scheme is capable of resolving the sharp interface between the liquid and vapor phases. The Compressive scheme was found to be stable using a time step size larger than the Geo-Reconstruct scheme, however for most cases the physical simulation time required to reach convergence was shorter using the Geo-Reconstruct scheme. As a result, the two schemes were comparable in terms of total computational cost.

Based on the above, it is recommended that TPCT simulations use the proposed or a similar model for variable saturation temperature in combination with the Geo-Reconstruct scheme, a full 3D computational domain that includes both fluid and solid regions of the thermosyphon geometry, mass transfer time relaxation parameters based on liquid-to-vapor density ratio, and constant heat flux boundary conditions for both evaporator and condenser. Choice of the value of the evaporation (or condensation) mass transfer coefficient should be determined via numerical experimentation and optimization, with mass balance used as a metric to determine the optimum value if experimental results are not available for validation.

5.3 CFD Simulation on OHP

This paper extends upon a prior study of CFD simulation methods for two-phase flow in heat pipe applications [4.27] and applies them to the simulation of an oscillating heat pipe (OHP).

Specifically, the methodology consists of applying the volume-of-fluid (VOF) model with a Compressive discretization scheme for the volume-fraction equation, in combination with a proposed model for variable saturation temperature based on the total liquid-to-vapor mass transfer in the system. Simulations were run using a fully three-dimensional, unsteady approach. Use of the implicit Compressive scheme allowed for significantly larger time-step size than possible for stable solution with explicit schemes that have been used in previous simulations documented in the literature. The use of a variable saturation temperature model facilitated convergence to a stationary state for which the filling ratio and saturation temperature remained close to the experimental test case. Comparison of results to experimental data show that the method used yields results that are significantly more accurate than previously documented CFD results for the same test case. The new method adopted here allows for successful prediction of the oscillating flow behavior of water as the working fluid inside the OHP and for a significant increase in the simulation time step size in comparison to the more commonly used Geo-Reconstruct method. Future work will focus on additional simulations with an alternative convective heat transfer boundary condition for the condenser, higher evaporation and condensation mass transfer time relaxation parameters, different geometries and varying heat loads.

5.4 Future Work

Future work of the CFD simulation on the OHP will focus on additional simulations with an alternative convective heat transfer boundary condition for the condenser, higher evaporation and condensation mass transfer time relaxation parameters, different geometries, and varying heat loads. Ferrofluid will be employed as the working fluid besides water in the CFD simulation on the OHP. Results from the OHP CFD simulations are going to be combined with the analytical model for ferrofluidic induction to yield a method for predicting the potential energy harvesting

power output in an OHP for different ferrofluid concentrations, external magnetic fields, and operating temperatures. The resulting predictive tool can be used to determine optimum design and operating conditions for energy harvesting using these devices.

CHAPTER VI: REFERENCES

[1.1] Cepnik, C., Lausecker,R., Wallrabe, U., 2013, "Review on Electrodynamic Energy Harvester-A Classification Approach," Micromachines, Vol. 4, pp. 168-196.

[1.2] Pozo, B., Garate, J.I., Araujo, J.A., Ferreiro, S., 2019, "Energy Harvesting Technologies and Equivalent Electronic Structural Models – Review," Electronics, Vol.8.

[1.3] Bibo, A., Masana, R., King, A., Li, G., Daqaq, M.F., 2012, "Electromagnetic ferrofluid-based energy harvester," Physics Letters A, Vol. 376, pp. 2163-2166.

[1.4] Alazemi, S.F., Bibo, A., Daqaq, M.F., 2015, "A ferrofluid based energy harvester: An experimental investigation involving internally-resonant sloshing modes," European Physical Journal of Special Topics, Vol. 224, pp. 2993-3004.

[1.5] Alazmi, S., Xu, Y., Daqaq, M. F., 2016 "Harvesting energy from the sloshing motion of ferrofluids in an externally excited container: Analytical modeling and experimental validation," Physics of Fluids, Vol. 28.

[1.6] Liu, Q., Alazemi, S.F., Daqaq, M.F., Li, G., 2018, "A ferrofluid based energy harvester: Computational modeling, analysis, and experimental validation," Journal of Magnetism and Magnetic Materials, Vol. 449, pp. 105-118.

[1.7] Monroe, J.G., Vasquez, E.S., Aspin, Z.S., Walters, K.B., Berg, M.J., Thompson, S.M., 2015, "Electromagnetic induction by ferrofluid in an oscillating heat pipe," Applied Physics Letters Vol. 106.

[1.8] Monroe, J.G., Vasquez, E.S., Aspin, Z.S., Fairly, J.D., Walters, K.B., 2015, "Energy Harvesting via Ferrofluidic Induction," Proceeding of SPIE 9493, Energy Harvesting and Storage: Materials, Devices, and Applications VI.

[1.9] Monroe, J.G., Kumari, S., Fairley, J.D., Walters, K.B., Berg, M.J., Thompson, S.M., 2018, "On the Energy Harvesting and Heat Transfer Ability of a Ferro-Nanofluid Oscillating Heat Pipe," International Journal of Heat and Mass Transfer, Vol.132, pp. 162-171.

[1.10] Oh, D.W., Sohn, D.Y., Byun, D.G., Kim, Y.S., 2014, "Analysis of Electromagnetic Force Characteristics and Device Implementation for Ferrofluid Based Energy Harvesting System," 17th International Conference on Electrical Machines and Systems (ICEMS).

[1.11] Kim, Y.S., 2015, "Analysis of Electromotive Force Characteristics for Electromagnetic Energy Harvester using Ferrofluid," Journal of Magnetics, Vol. 20, pp. 252-257.

[1.12] Chen, C.Y., Wang, Y.S., Wu, C.M., Lin, C.H., Huang, K.A., 2012, "Characteristics of electromagnetic induction by moving ferrofluids," Magnetohydrodynamics, Vol.48, pp. 567-580.

[1.13] Seol, M.L., Jeon, S.B., Han, J.W., Choi, Y.K., 2017, "Ferrofluid-based triboelectric-electromagnetic hybrid generator for sensitive and sustainable vibration energy harvesting," Nano Energy, Vol. 31, pp. 233–238.

[1.14] Bakhtiar, S., Khan, F.U., 2019, "Analytical Modeling and Simulation of an Electromagnetic Energy Harvester for Pulsating Fluid Flow in Pipeline," The Scientific World Journal.

[1.15] Wagner, A.M., 2014, "Review of Thermosyphons Applications," Technical Report ERDC/CRREL TR-14-1, Cold Regions Research and Engineering Laboratory (CRREL), Hanover, New Hampshire.

[1.16] Jafari, D., Franco, A., Filippeschi, S., Marco, P.D., 2016, "Two-phase closed thermosyphon: A review of studies and solar applications," Renewable and Sustainable Reviews, Vol. 53, pp. 575-593.

[1.17] Jadhav, S.A., Patil, S.A., 2016, "Two-Phase Thermosyphon – A Review of Studies," International Journal of Engineering Sciences & Research Technology., Vol. 53, pp. 575-593.

[1.18] Ramezanizedeh, M., Nazari, M.A., Ahmadi, M.H., Lorenzini, G., Kumar, R., Jilte, R., 2018, "A review on the solar applications of thermosyphons," Mathematical Modelling of Engineering Problems, Vol. 5, No. 4, pp. 275-280.

[1.19] A. Alizadehdakhel, M. Rahimi, A.A. Alsairafi, 2010, "CFD modeling of flow and heat transfer in a thermosyphon," International Communications in Heat and Mass Transfer, Vol. 37, pp. 312-318.

[1.20] B. Fadhl, L.C. Wrobel, H. Jouhara, 2013, "Numerical modelling of the temperature distribution in a two-phase thermosyphon," Applied Thermal Engineering, Vol. 60, pp. 122-131.

[1.21] B. Fadhl, L.C. Wrobel, H. Jouhara, 2015, "CFD simulation of a two-closed thermosyphon charged with R134a and R404a," Applied Thermal Engineering, Vol. 78, pp. 482-490.

[1.22] H. Jouhara, B. Fadhl, L.C. Wrobel, 2016, "Three-dimensional CFD simulation of geyser boiling in a two-phase closed thermosyphon," International Journal of Hydrogen Energy, Vol. 41, pp. 16463-16476.

[1.23] Alammar, A.A., Al-Dadah, R.K., Mahmoud, S.M., 2016, "Numerical investigation of effect of fill ratio and inclination angle on a thermosyphon heat pipe thermal performance," Applied Thermal Engineering, Vol.108, pp. 1055-1065.

[1.24] Song, H., Zhang, W., Li, Y., Yang, Z., Ming, A., 2016, "Simulation of the Vapor-Liquid Two-Phase Flow of Evaporation and Condensation," International Journal of Heat and Technology, Vol. 34, pp. 663-670.

[1.25] Asmaie, L., Haghshenasfard, M., Zeinabad, A.M., Esfahany, M.N., 2013, "Thermal performance analysis of nanofluids in a thermosyphon heat pipe using CFD modeling," Heat Mass Transfer, Vol. 49, pp. 667-668.

[1.26] Wang, X., Wang, Y., Chen, H., Zhu, Y., 2018, "A combined CFD/visualization investigation of heat transfer behaviors during geyser boiling in two-phase closed thermosyphon," International Journal of Heat and Mass Transfer, Vol. 121, pp. 703-714.

[1.27] Wang, Y., Wang, X., Chen, H., Taylor, R.A., Zhu, T., 2017, "A combined CFD/visualized investigation of two-phase heat and mass transfer inside a horizontal loop thermosiphon," International Journal of Heat and Mass Transfer, Vol. 112, pp. 607-619.

[1.28] Kim, Y., Choi, J., Kim, S., Zhang, Y., 2015, "Effects of mass transfer time relaxation parameters on condensation in a thermosyphon," Journal of Mechanical Science and Technology, Vol. 29, pp. 5497~5505.

[1.29] Xu, Z., Zhang, Y., Li, B., Huang, J., 2016, "Modeling the phase change process for a two-phase closed thermosyphon by considering transient mass transfer time relaxation parameter," International Journal of Heat and Mass Transfer, Vol. 101, pp. 614-619.

[1.30] Xu, Z., Zhang, Y., Li, B., Wang, C.C., Ma, Q., 2018, "Heat performances of a thermosyphon as affected by evaporator wettability and filling ratio," Applied Thermal Engineering, Vol. 129, pp. 665-673.

[1.31] Kafeel, K., Turan, A., 2013, "Axi-symmetric simulation of a two-phase vertical thermosyphon using Eulerian two-fluid methodology," Heat Mass Transfer, Vol. 49, pp. 1089-1099.

[1.32] Kafeel, K., Turan, A., 2014, "Simulation of the response of a thermosyphon under pulsed heat input conditions," International Journal of Thermal Sciences, Vol. 80, pp. 33-40.

[1.33] Zhao, Z., Zhang, Y., Zhang, Y., Zhou, Y., Hu, H., 2018, "Numerical study on the transient thermal performance of a two-phase closed thermosyphon," Energies, Vol. 11, pp. 1433.

[1.34] Sonawane, C.R., Gole, P., Pandey, A.K., 2019, “Numerical modelling of two phase closed thermosyphon flexible heat pipe,” Twelve International Conference on Thermal Engineering: Theories and Applications.

[1.35] Temimy, A.A.B., Abdulrasool, A. A., 2019, “CFD modelling for flow and heat transfer in a closed thermosyphon charged with water – A new observation for the two-phase interaction,” 2nd International Conference on Sustainable Engineering Techniques.

[1.36] Wang, X., Zhu, Y., Wang, Y., 2019, “Development of pressure-based phase change model for CFD modelling of heat pipes,” International Journal of Heat and Mass Transfer, Vol.145, pp. 118763.

[1.37] H. Akachi, Structure of Heat Pipe, US Patent, 4921041, 1990.

[1.38] Bastakoti, D., Zhang, H., Li, D., Cai, W., Li, F., 2018, “An overview on the developing trend of pulsating heat pipe and its performance,” Applied Thermal Engineering, Vol. 141, pp.305-322.

[1.39] Han, X., Wang, X., Zheng, H., Xu., X., Chen, G., 2016, “Review of the development of pulsating heat pipe for heat dissipation,” Renewable and Sustainable Energy Reviews, Vol. 59, pp. 692-709.

[1.40] Nazari, M.A., Ahmadi, M.H., Ghasempour, R., Shafii, M.B., Mahian, O., Kalogirou, S., Wongwises, S., 2018, “A review on pulsating heat pipes: from solar to cryogenic applications,” Applied Energy, Vol. 222, pp.475-484.

[1.41] Liu, X., Hao, Y., 2009, “Numerical Simulation of Liquid – Vapor Two – Phase Flow in a Closed Loop Oscillating Heat Pipe,” Proceedings of the ASME 2009 International Mechanical Engineering Congress & Exposition, No. 2009-12038, pp. 609-617.

[1.42] Wang, J., Ma. H., Zhu, Q., 2015, “Effects of the evaporator and condenser length on the performance of pulsating heat pipes,” Applied Thermal Engineering, Vol. 91, pp. 1018-1025.

[1.43] Mohammad, W.S., Ahmed, I.S., 2016, “Numerical simulation of oscillating heat pipe using VOF model,” Australian Journal of Basic and Applied Science, Vol. 10 (14), pp. 196-206.

[1.44] Gupta, A., Parwani, A.K., 2017, “CFD modeling for thermal performance of Closed Loop Pulsating heat pipe in bottom heated mode,” Proceedings of Sixth International Conference on Advances in Civil, Structural and Mechanical Engineering, pp. 46-50.

[1.45] E, J., Zhao, X., Deng, Y., Zhu, H., 2016, “Pressure distribution and flow characteristics of closed oscillating heat pipe during the starting process at different vacuum degrees,” Applied Thermal Engineering, Vol. 93, pp. 166-173.

[1.46] Nagwase, S.Y., Pachghare, P.R., 2013, “Experimental and CFD Analysis of Closed Loop Pulsating Heat Pipe with DI-Water,” Proceedings of the IEEE international conference on energy efficient technologies for sustainability (ICEETS), pp. 185-190.

[1.47] Suresh, J.V., Bhramara, P., 2016, “CFD Analysis of Single Turn Pulsating Heat Pipe,” International Journal of Scientific & Engineering Research, Vol. 7, Issue 6.

[1.48] Suresh, J.V., Bhramara, P., 2017, “CFD Analysis of Copper Closed Loop Pulsating Heat Pipe,” Materials Today: Proceedings 5, pp. 5487-5495.

[1.49] Patel, M.S., Mane, S.D., Mopare, S.S., Patil, D.Y., 2017, “Comparison of Heat Transfer Rate of Closed Loop Micro Pulsating Heat Pipes having different number of turns,” the International Journal of Engineering and Science, Vol. 6, Issue 7, pp. 1-12.

[1.50] Johnson, E.J., Joshi, S.M. Sarangi, R.K.,2017, “Performance of Closed Loop Pulsating Heat Pipe: A Numerical Analysis,” International Journal of Latest Technology in Engineering, Management & Applied Sciences, Vol. VI, Issue VII.

[1.51] Pal, M.K., Satra, N., Dixit, S., 2018, “Comparative Analysis of a Closed Loop Pulsating Heat Pipes (CLPHPs) on the Basis of their Material and Working Fluid,” International Journal of Latest Technology in Engineering, Management & Applied Sciences, Vol.8, Issue IV.

[1.52] Park, S.H., Park, Y.G., Ha, M.Y., “Numerical Simulation on the Two-Phase Flow Pattern in the Loop Pipe with R-134A,” 13th International Conference on Heat Transfer, Fluid Mechanics and Thermodynamics.

[1.53] Kathait, P.S., Sharma, R.N, 2018, “The operational characteristics of a pulsating heat pipe (PHP) under different startup modes,” 21st Australasian Fluid Mechanics Conference.

[1.54] Han, S.H., Choi, J.W., Kim, S.C., 2016, “Computational Analysis of Thermal Flow with Varying the Diameter and the Number of Tubes in Pulsating Heat Pipes,” Journal of Computational Fluids, Vol. 21, No.1, pp. 86-93.

[1.55] Sree, N.S., Sudheer, N.V.S.S., Bhramara, P., 2018, “Thermal Analysis of Closed Loop Pulsating Heat Pipe,” International Journal of Mechanics and Production, Vol. 8, Issue 2.

[1.56] Rajendra, S.D., Deshmukh, D.A., Pawar, R.S., 2019, “Experimental Investigation of Closed Loop Pulsating Heat Pipe Thermal Performance and CFD Validation,” Journal of Thermal Engineering and Technology, Vol. 4, Issue 1, pp. 33-51.

[1.57] Haque, M.A. U., Azizuddin, M.,2016, “CFD and Volume Fraction Analysis of Closed Loop Pulsating Heat Pipe (CLPHP),” IOSR Journal of Mechanical and Civil Engineering, Vol. 13, Issue 5, Ver. IV, pp. 88-94.

[1.58] Wang, S.F., Lin, Z.R., Lee, Z.Y., Zhang, L.W., 2010, “Numerical Simulation on Flow and Heat Transfer in Oscillating Heat Pipes,” 10th International Heat Pipes Symposium.

[1.59] Lin, Z., Wang, S., Shirakashi, R., Zhang, L.W., 2013, “Simulation of a miniature oscillating heat pipe in bottom heating mode using CFD with unsteady modeling,” International Journal of Heat and Mass Transfer, Vol. 57, pp. 642-656.

[1.60] R, B.E., Reddy, G.V.G., 2017, “Effect of Filling Ratio on Thermal Performance of Closed Loop Pulsating Heat Pipe,” International Journal of Advances in Scientific Research and Engineering, Vol.3, Special Issue 1, pp.223-229.

[1.61] Kumar, V., S, R., 2014, “CFD Analysis and Experimental Investigation on Thermal Performance of Closed Loop Pulsating Heat Pipe Using Different Nanofluids,” International Journal of Advanced Research, Vol. 2, Issue 8, pp. 753-760.

[1.62] Muchrikar, A., Soni, N., 2017, “Numerical Analysis of Closed Loop Pulsating Heat Pipe Using CFD,” International Journal of Scientific Research in Science, Engineering and Technology, Vol.3, Issue 8, pp. 860-863.

[2.1] Sansom, C.L., Jones, P., Dorey, R.A., Beck, C., Stanhope-Bosumpim, A., Peterson, J., 2013, “Synthesis and characterization of $Mn_{0.5}Zn_{0.5}Fe_2O_4$ and Fe_3O_4 nanoparticle ferrofluids for thermo-electric conversion,” Journal of Magnetism and Magnetic Materials, Vol. 335, pp. 159-162.

[2.2] Yarahmadi, M., Goudarzi, H.M., Shafii, M.B., 2015, “Experimental investigation into laminar forced convective heat transfer of ferrofluids under constant and oscillating magnetic field with different magnetic field arrangements and oscillation modes,” Experimental Thermal and Fluid Science, Vol. 68, pp. 601-611.

[2.3] Chen, C.Y., Wang, S.Y., Wu, C.M., Lin, C.H., Huang, K.A., 2012, “Characteristics of electromagnetic induction by moving ferrofluids,” Magnetohydrodynamics, Vol. 48, pp. 567-580.

[2.4] Bibo, A., Masana, R., King, A., Li, G., Daqaq, M.F., 2012, “Electromagnetic ferrofluid-based energy harvester,” Physics Letters A, Vol. 376, pp. 2163-2166.

[2.5] Alazemi, S.F., Bibo, A., Daqaq, M.F., 2015, “A ferrofluid based energy harvester: An experimental investigation involving internally-resonant sloshing modes,” The European Physical Journal of Special Topics, Vol. 224, pp. 2993-3004.

[2.6] Oh, D.W., Sohn, D.Y., Byun, D.G., Kim, Y.S., 2014, “Analysis of Electromagnetic Force Characteristics and Device Implementation for Ferrofluid Based Energy Harvesting System,” 17th International Conference on Electrical Machines and Systems (ICEMS), pp.2033-2038.

[2.7] Kim, Y.S., 2015, “Analysis of Electromotive Force Characteristics for Electromagnetic Energy Harvester using Ferrofluid,” Journal of Magnetics, Vol. 20, pp. 252-257.

[2.8] Monroe, J.G., Vasquez, E.S., Aspin, Z.S., Walters, K.B., Berg, M.J., Thompson, S.M., 2015, “Electromagnetic induction by ferrofluid in an oscillating heat pipe,” Applied Physics Letters, Vol.106, pp. 26931.

[2.9] Monroe, J.G., Kumari, S., Fairley, J.D., Walters, K.B., Berg, M.J., Thompson, S.M., 2019, "On the Energy Harvesting and Heat Transfer Ability of a Ferro-Nanofluid Oscillating Heat Pipe," International Journal of Heat and Mass Transfer, Vol.132, pp. 162-171.

[2.10] Seol, M.L., Jeon, S.B., Han, J.W., Choi, Y.K., 2017, “Ferrofluid-based triboelectric-electromagnetic hybrid generator for sensitive and sustainable vibration energy harvesting,” Nano Energy, Vol.31, pp.233–238.

[2.11] Ozbey, A., Karimzadehkhouei, M., Yalcin, S.E., Gozuacik, D., Kosar, A., 2015, “Modeling of ferrofluid magnetic actuation with dynamic magnetic field in small channels,” Microfluid Nanofluid, Vol.18, pp. 447–460.

[2.12] Berthier, J., Ricoul, F., 2002, “Numerical modeling of ferrofluid flow instabilities in a capillary tube at the vicinity of a magnet,” Proceedings of 2002 Modeling and Simulation of Microsystem Conference, pp. 22–25.

[2.13] Papadopoulos, P.K., Vafeas, P., Hatzikonstantinou, P.M., 2012, “Ferrofluid pipe flow under the influence of the magnetic field of a cylindrical coil,” Physics of Fluids, Vol. 24, pp. 122002.

[2.14] Furlani, E. P. Xue, X., 2012, “Field, force and transport analysis for magnetic particle-based gene delivery,” Microfluid Nanofluid, Vol. 13, pp. 589–602.

[2.15] Khashan, S. A., Alazzam, A., Furlani, E.P., 2015, “Computational Analysis of Enhanced Magnetic Bioseparation in Microfluidic Systems with Flow-Invasive Magnetic Elements,” Scientific Reports, No.4.

[2.16] Monroe, G., Vasquez, E., Aspin, Z., Fairly, J., Walters, K.B., 2015, “Energy Harvesting via Ferrofluidic Induction,” Proceeding of SPIE 9493, Energy Harvesting and Storage: Materials, Devices, and Applications VI.

[2.17] Griffiths, D.J., Introduction to Electrodynamics, pp. 314-315.

[2.18] Taylor, S., Leus, V., 2012, “The magneto-kinematic effect for the case of rectilinear motion,” European Journal of Physics, Vol. 33, pp. 837–852.

[2.19] Butter, K., Bomans, P.H.H., Frederik, P.M., Vroege, G.J., Philipse, P., 2003, “Direct observations of dipolar chains in iron ferrofluids by cryogenic electron microscopy,” Nature Materials, Vol. 2, pp. 88-91.

[2.20] Yoon, M., Tomanck, D., 2010, “Equilibrium structure of ferrofluid aggregates,” Journal of Physics.: Condensed Matter, Vol. 22, No.45.

[2.21] Wang, J., Sun, J., Sun, Q., Chen, Q., 2003, “One-step hydrothermal process to prepare highly crystalline Fe_3O_4 nanoparticles with improved magnetic properties,” Materials Research Bulletin, Vol. 38, pp. 1113-1118.

[2.22] R. E. Rosensweig, Ferrohydrodynamics, 1985, Cambridge University Press.

[3.1] Jafari, D., Franco, A., Filippeschi, S., Marco, P.D., 2016, “Two-phase closed thermosyphon: A review of studies and solar applications,” Renewable and Sustainable Reviews, Vol. 53, pp. 575-593.

[3.2] Alizadehdakhel, A., Rahimi, M., Alsairafi, A.A., 2010, “CFD modeling of flow and heat transfer in a thermosyphon,” International Communications in Heat and Mass Transfer, Vol. 37, pp. 312-318.

[3.3] Fadhl, B., Wrobel, L.C., Jouhara, H., 2013, “Numerical modelling of the temperature distribution in a two-phase thermosyphon,” Applied Thermal Engineering, Vol. 60 pp. 122-131.

[3.4] Fadhl, B., Wrobel, L.C., Jouhara, H., 2015, “CFD simulation of a two-closed thermosyphon charged with R134a and R404a,” Applied Thermal Engineering, Vol. 78, pp. 482-490.

[3.5] Jouhara, H., Fadhl, B., Wrobel, L.C., 2016, “Three-dimensional CFD simulation of geyser boiling in a two-phase closed thermosyphon,” International Journal of Hydrogen Energy, Vol.41, pp.16463-16476.

[3.6] Alammar, A.A., Al-Dadah, R.K., Mahmoud, S.M., 2016, “Numerical investigation of effect of fill ratio and inclination angle on a thermosyphon heat pipe thermal performance,” Applied Thermal Engineering, Vol. 108 pp. 1055-1065.

[3.7] Song, H., Zhang, W., Li, Y., Yang, Z., Ming, A., 2016, “Simulation of the Vapor-Liquid Two-Phase Flow of Evaporation and Condensation,” International Journal of Heat and Technology, Vol. 34, pp. 663-670.

[3.8] Asmaie, L., Haghshenasfard, M., Zeinabad, A. M., Esfahany, M.N., 2013, "Thermal performance analysis of nanofluids in a thermosyphon heat pipe using CFD modeling," Heat Mass Transfer, Vol.49, pp. 667-668.

[3.9] Wang, X., Wang, Y., Chen, H., Zhu, Y., 2018, "A combined CFD/visualization investigation of heat transfer behaviors during geyser boiling in two-phase closed thermosyphon," International Journal of Heat and Mass Transfer, Vol. 121, pp. 703-714.

[3.10] Wang, Y., Wang, X., Chen, H., Taylor, R.A., Zhu, T., 2017, "A combined CFD/visualized investigation of two-phase heat and mass transfer inside a horizontal loop thermosiphon," International Journal of Heat and Mass Transfer, Vol. 112, pp. 607-619.

[3.11] Kim, Y., Choi, J., Kim, S., Zhang, Y., 2015, "Effects of mass transfer time relaxation parameters on condensation in a thermosyphon," Journal of Mechanical Science and Technology, Vol. 29, pp. 5497~5505.

[3.12] Xu, Z., Zhang, Y., Li, B., Huang, J., 2016, "Modeling the phase change process for a two-phase closed thermosyphon by considering transient mass transfer time relaxation parameter," International Journal of Heat and Mass Transfer, Vol. 101, pp. 614-619.

[3.13] Xu, Z., Zhang, Y., Li, B., Wang, C.C., Ma, Q., 2018, "Heat performances of a thermosyphon as affected by evaporator wettability and filling ratio," Applied Thermal Engineering, Vol. 129, pp.665-673.

[3.14] Kafeel, K., Turan, A., 2013, "Axi-symmetric simulation of a two-phase vertical thermosyphon using Eulerian two-fluid methodology," Heat Mass Transfer, Vol. 49, pp. 1089-1099.

[3.15] Kafeel, K., Tura, A., 2014, "Simulation of the response of a thermosyphon under pulsed heat input conditions," International Journal of Thermal Sciences, Vol. 80, pp. 33-40.

[3.16] Wang, H., Walters, K.B., Walters, D.K., “The effect of model parameters on CFD simulation of a thermosyphon,” ASME JSME KSME Joint Fluids Conference 2019, No. 2019-4896.

[3.17] Wang, X., Zhu, Y., Wang, Y., 2019, “Development of pressure-based phase change model for CFD modelling of heat pipes,” International Journal of Heat and Mass Transfer, Vol.145, pp. 118763.

[3.18] Lee, W.H., 1979, "A Pressure Iteration Scheme for Two-Phase Modeling," Technical Report LA-UR 79-975. Los Alamos Scientific Laboratory, Los Alamos, New Mexico.

[3.19] Brackbill, J. U., Kothe, D. B., Zemach., C., 1992, “A Continuum Method for Modeling Surface Tension,” Journal of Computational Physics, Vol.100, pp. 335-354.

[3.20] Incropera, F.P., Dewitt, D.P., Bergman, T.L., Lavine, A.S., “Principles of Heat and Mass Transfer”, 7th edition, Appendix A.6.

[3.21] Bernardin, J.D., Mudawar, I., Walsh, C.B., Franses, E.T., 1997, “Contact angle temperature dependence for water droplets on practical aluminum surfaces,” International Journal of Heat and Mass Transfer, Vol.40, pp. 1017-1033.

[3.22] ANSYS, *ANSYS Fluent Theory Guide 16.7.3*, ANSYS, Inc., Canonsburg, PA.

[4.1] H. Akachi, Structure of Heat Pipe, US Patent, 4921041, 1990.

[4.2] Bastakoti, D., Zhang, H., Li, D., Cai, W., Li,F.,2018, “An overview on the developing trend of pulsating heat pipe and its performance,” Applied Thermal Engineering, Vol. 141, pp.305-322.

[4.3] Han, X., Wang, X., Zheng, H., Xu., X., Chen, G., 2016, “Review of the development of pulsating heat pipe for heat dissipation,” Renewable and Sustainable Energy Reviews, Vol. 59, pp. 692-709.

[4.4] Nazari, M.A., Ahmadi, M.H., Ghasempour, R., Shafii, M.B., Mahian, O., Kalogirou, S., Wongwises, S., 2018, “A review on pulsating heat pipes: from solar to cryogenic applications,” Applied Energy, Vol. 222, pp.475-484.

[4.5] Liu, X., Hao, Y., 2009, “Numerical Simulation of Liquid – Vapor Two – Phase Flow in a Closed Loop Oscillating Heat Pipe,” Proceedings of the ASME 2009 International Mechanical Engineering Congress & Exposition, No. 2009-12038, pp. 609-617.

[4.6] Wang, J., Ma. H., Zhu, Q., 2015, “Effects of the evaporator and condenser length on the performance of pulsating heat pipes,” Applied Thermal Engineering, Vol. 91, pp. 1018-1025.

[4.7] Mohammad, W.S., Ahmed, I.S., 2016, “Numerical simulation of oscillating heat pipe using VOF model,” Australian Journal of Basic and Applied Science, Vol. 10 (14), pp. 196-206.

[4.8] Gupta, A., Parwani, A.K., 2017, “CFD modeling for thermal performance of Closed Loop Pulsating heat pipe in bottom heated mode,” Proceedings of Sixth International Conference on Advances in Civil, Structural and Mechanical Engineering, pp. 46-50.

[4.9] E, J., Zhao, X., Deng, Y., Zhu, H., 2016, “Pressure distribution and flow characteristics of closed oscillating heat pipe during the starting process at different vacuum degrees,” Applied Thermal Engineering, Vol. 93, pp. 166-173.

[4.10] Nagwase, S.Y., Pachghare, P.R., 2013, “Experimental and CFD Analysis of Closed Loop Pulsating Heat Pipe with DI-Water,” Proceedings of the IEEE international conference on energy efficient technologies for sustainability (ICEETS), pp. 185-190.

[4.11] Suresh, J.V., Bhramara, P., 2016, “CFD Analysis of Single Turn Pulsating Heat Pipe,” International Journal of Scientific & Engineering Research, Vol. 7, Issue 6.

[4.12] Suresh, J.V., Bhramara, P.,2017, “CFD Analysis of Copper Closed Loop Pulsating Heat Pipe,” Materials Today: Proceedings 5 pp. 5487-5495.

[4.13] Patel, M.S., Mane, S.D., Mopare, S.S., Patil, D.Y., 2017, “Comparison of Heat Transfer Rate of Closed Loop Micro Pulsating Heat Pipes having different number of turns,” the International Journal of Engineering and Science, Vol. 6, Issue 7, pp. 1-12.

[4.14] Johnson, E.J., Joshi, S.M. Sarangi, R.K., 2017, “Performance of Closed Loop Pulsating Heat Pipe: A Numerical Analysis,” International Journal of Latest Technology in Engineering, Management & Applied Sciences, Vol. VI, Issue VII.

[4.15] Pal, M.K., Satra, N., Dixit, S., 2018, “Comparative Analysis of a Closed Loop Pulsating Heat Pipes (CLPHPs) on the Basis of their Material and Working Fluid,” International Journal of Latest Technology in Engineering, Management & Applied Sciences, Vol.8, Issue IV.

[4.16] Park, S.H., Park, Y.G., Ha, M.Y., “Numerical Simulation on the Two-Phase Flow Pattern in the Loop Pipe with R-134A,” 13th International Conference on Heat Transfer, Fluid Mechanics and Thermodynamics.

[4.17] Kathait, P.S., Sharma, R.N, 2018, “The operational characteristics of a pulsating heat pipe (PHP) under different startup modes,” 21st Australasian Fluid Mechanics Conference.

[4.18] Han, S.H., Choi, J.W., Kim, S.C., 2016, “Computational Analysis of Thermal Flow with Varying the Diameter and the Number of Tubes in Pulsating Heat Pipes,” Journal of Computational Fluids, Vol. 21, No.1, pp. 86-93.

[4.19] Sree, N.S., Sudheer, N.V.S.S., Bhramara, P., 2018, “Thermal Analysis of Closed Loop Pulsating Heat Pipe,” International Journal of Mechanics and Production, Vol. 8, Issue 2.

[4.20] Rajendra, S.D., Deshmukh, D.A., Pawar, R.S., 2019, “Experimental Investigation of Closed Loop Pulsating Heat Pipe Thermal Performance and CFD Validation,” Journal of Thermal Engineering and Technology, Vol. 4, Issue 1, pp. 33-51.

[4.21] Haque, M.A. U., Azizuddin, M.,2016, “CFD and Volume Fraction Analysis of Closed Loop Pulsating Heat Pipe (CLPHP),” IOSR Journal of Mechanical and Civil Engineering, Vol. 13, Issue 5, Ver. IV, pp. 88-94.

[4.22] Wang, S.F., Lin, Z.R., Lee, Z.Y., Zhang, L.W., 2010, “Numerical Simulation on Flow and Heat Transfer in Oscillating Heat Pipes,” 10th International Heat Pipes Symposium.

[4.23] Lin, Z., Wang, S., Shirakashi, R., Zhang, L.W., 2013, “Simulation of a miniature oscillating heat pipe in bottom heating mode using CFD with unsteady modeling,” International Journal of Heat and Mass Transfer, Vol. 57, pp. 642-656.

[4.24] R, B.E., Reddy, G.V.G., 2017, “Effect of Filling Ratio on Thermal Performance of Closed Loop Pulsating Heat Pipe,” International Journal of Advances in Scientific Research and Engineering, Vol.3, Special Issue 1, pp.223-229.

[4.25] Kumar, V., S, R., 2014, “CFD Analysis and Experimental Investigation on Thermal Performance of Closed Loop Pulsating Heat Pipe Using Different Nanofluids,” International Journal of Advanced Research, Vol. 2, Issue 8, pp. 753-760.

[4.26] Muchrikar, A., Soni, N., 2017, “Numerical Analysis of Closed Loop Pulsating Heat Pipe Using CFD,” International Journal of Scientific Research in Science, Engineering and Technology, Vol.3, Issue 8, pp. 860-863.

[4.27] Wang, H., Walters, K.B., Walters, D.K., “The effect of model parameters on CFD simulation of a thermosyphon,” ASME JSME KSME Joint Fluids Conference 2019, No. 2019-4896.

[4.28] Lee, W.H., 1979, "A Pressure Iteration Scheme for Two-Phase Modeling," Technical Report LA-UR 79-975. Los Alamos Scientific Laboratory, Los Alamos, New Mexico.

[4.29] Brackbill, J. U., Kothe, D. B., Zemach., C., 1992, "A Continuum Method for Modeling Surface Tension," Journal of Computational Physics, Vol.100, pp. 335-354.

[4.30] Incropera, F.P., Dewitt, D.P., Bergman, T.L., Lavine, A.S., "Principles of Heat and Mass Transfer," 7th edition, Appendix A.6.

[4.31] Bernardin, J.D., Mudawar, I., Walsh, C.B., Franses, E.T., 1997, "Contact angle temperature dependence for water droplets on practical aluminum surfaces," International Journal of Heat and Mass Transfer, Vol.40, pp. 1017-1033.